NTNU
Norwegian University of
Science and Technology

Three dimensional Finite Element Modeling of a Brushless Doubly-fed Induction Machine

Wani Faisal Mushtaq

Wind Energy
Submission date: August 2016
Supervisor: Robert Nilssen, ELKRAFT
Co-supervisor: Henk Polinder, Delft University of Technology, Netherlands

Norwegian University of Science and Technology
Department of Electric Power Engineering

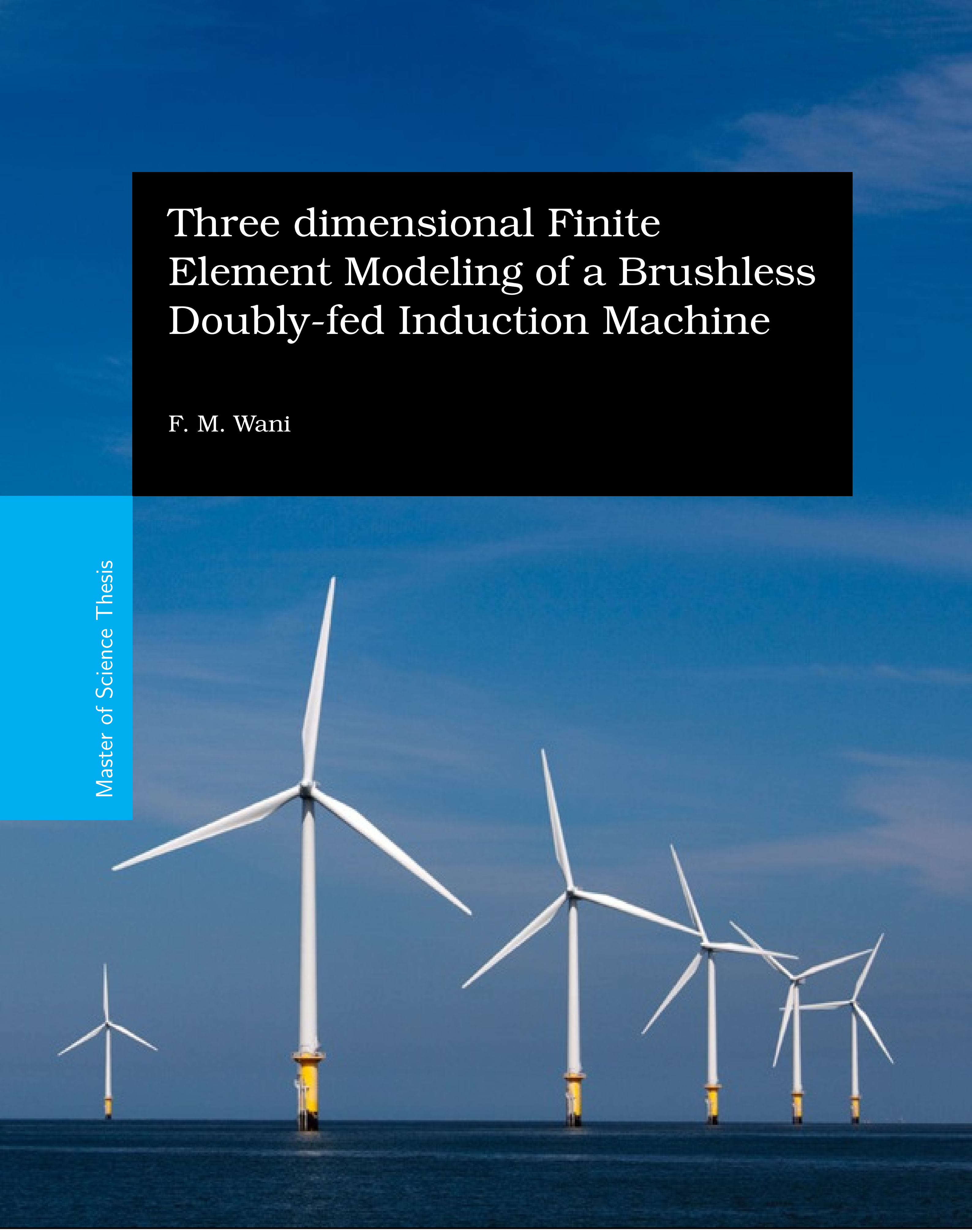

Three dimensional Finite Element Modeling of a Brushless Doubly-fed Induction Machine

F. M. Wani

Master of Science Thesis

TU Delft
Delft
University of
Technology

NTNU
Norwegian University of
Science and Technology

European Wind Energy Masters

THESIS REPORT, EUROPEAN WIND ENERGY MASTERS, ELECTRIC POWER SYSTEMS TRACK

Three dimensional Finite Element Modeling of a Brushless Doubly-fed Induction Machine

by

Faisal Mushtaq Wani

in partial fulfillment of the requirements for the degrees of

MSc in Electrical Engineering at Delft University of Technology
&
MSc-Technology in Wind Energy at Norwegian University of Science and Technology,

under the European Wind Energy Masters programme.

To be defended publicly
on Monday August 22, 2016 at TU Delft.

Supervisors:	Dr. ir. H. Polinder,	TU Delft
	Prof. R. Nilssen,	NTNU
Thesis committee:	Prof. R. Nilssen,	NTNU
	Dr. ir. H. Polinder,	TU Delft
	Dr. D. J. P. Lahaye,	TU Delft
	X. Wang,	TU Delft

Abstract

As we move deeper into offshore waters to harness more of wind energy there is a need to keep the total operational and maintenance costs to a minimum, of which expenditures related to the generators form a major share. Brushless Doubly-fed Induction machine used as a generator, due to the requirement of a lower rating converter, and the absence of brush-gear and slip-ring arrangement can help in mitigating those costs.

2D models of the BDFIM have been developed to arrive at a better design so that the machine is able to compete with and possibly, outperform other solutions in the market. However, much like 2D models of the other machines, these models usually neglect or at best approximate certain practical aspects. These aspects mostly include effects arising due to physical features such as end windings, laminated structure of the iron, skew in the conductors, etc.

3D modeling can allow us to more accurately model these effects and perhaps, result in an even more efficient design. However, there are some caveats in this approach. 3D models, as expected, are mathematically more complex to formulate and solve. Besides, there is a multi-fold increase in the number of unknowns to be solved for which poses a significant challenge in terms of the memory requirement and the time cost of the model. The methods adopted to solve 2D problems hitherto, magnetostatic as well as transient, are not suitable to solve large scale 3D models.

The objective of this thesis is primarily to present a strategy to efficiently solve such 3D problems. In this regard, different magnetic potential formulations were considered, and the mathematical properties of the matrix system resulting from each formulation were outlined. Special emphasis is placed on the implementation of iterative solvers and multigrid preconditioning. Also, it will be demonstrated that a formulation resulting in fewer degrees of freedom does not necessarily translate into a memory and/or time efficient model.

This approach is then extended to estimate the axial flux in the BDFIM arising from the skewed rotor. In the 3D model, we consider the axial flux component and anisotropy of the iron which are neglected by the 2D multi-slice model. Upon analysis, it was observed that incorporating these effects leads to minimal improvement over the 2D multi-slice model which, however, more than outweighs this improvement by being computationally less expensive.

Acknowledgements

I would like to extend my profound gratitude to my supervisor Dr. ir. Henk Polinder for providing me with the opportunity to work on this thesis and for his constant guidance throughout this period. I deeply admire him for allowing me a lot of freedom during my research, whilst at the same time ensuring my work remained focused as well as result-oriented. My deepest thanks to my co-supervisor Prof. Robert Nilssen for being a part of several thought-provoking and fruitful discussions on several topics including this thesis, during my time at NTNU.

Furthermore, this thesis would not have been possible without the contribution of Dr. Domenico Lahaye. I am extremely grateful to him for his support both academically and otherwise, and reinforcing in me the desire to always strive for further improvement..

In addition to the above, I would also like to thank Xuezhou Wang for his tireless support, valuable insights, and bearing with me patiently during several of our discussions.

I would also like to take this opportunity to express my deeply felt gratitude towards my parents and siblings for their selfless support and patience with me.

Last but most certainly not the least, I sincerely appreciate all of my friends for sticking with me through thick and thin. Special mention must be made of my friends at Delft of which there are many—my apologies for not mentioning each one of them by their names—who were of great support especially during the days when I was recuperating after the accident. Any amount of thanks will be less than what they deserve.

Faisal Mushtaq Wani
Delft University of Technology

To my parents,
Rehana Wani and Mushtaq Ahmad Wani.

Table of Contents

List of Figures

List of Tables

Chapter 1

Introduction

Our dependence on fossil fuels amounts to global pyromania, and the only fire extinguisher we have at our disposal is renewable energy. —Hermann Scheer.

Chapter summary:

This chapter gives an account of the motivation behind this thesis and the previous research carried out in the same field. The problem definition, the research objectives and the outline of the thesis are also presented.

1.1 Background

One of many applications of induction machines is as a generator in wind turbines. The energy output from a wind turbine can be maximized by maintaining the optimal *tip-speed ratio*[1] in the turbine. Traditionally, Doubly-Fed Induction Machines (DFIMs) have been preferred over the conventional squirrel-cage induction machines for this purpose. Conventional induction machines used as Adjustable Speed Drives (ASDs) require a power electronic converter of the full kVA rating. This has implications for the size and the total cost of the system. On the other hand, doubly-fed induction machines can operate with a converter of substantially lower rating than the full kVA, thus offering a relatively inexpensive and a compact solution. However, this flexibility comes at a price. The presence of slip-rings and brush-gear arrangement in a DFIM makes it susceptible to frequent maintenance due to wear and tear, and also are a potential cause for sparking. These factors have been an impediment towards the wide-scale use of the DFIMs in the offshore wind turbines and various other drive applications [2]. Brushless Doubly-fed Induction Machine (BDFIM) offers a reliable solution under such circumstances without compromising the advantages of the DFIM. In other words, the machine still requires a power converter of the similar rating as a DFIM, albeit without the need for a slip-ring and brush configuration. This no longer makes the regular maintenance

---

[1] Tip-speed ratio of a wind turbine is defined as the ratio of the linear speed of the tip of the blade to the wind speed [1].

of the machine a necessity and thus, the BDFIM can be an effective solution at sites where frequent maintenance maybe a costly proposition e.g. offshore wind farms.

BDFIMs can also be operated at reduced speeds compared to the conventional DFIMs; this has advantages for the gear design [2]. For instance, it might be possible to eliminate a stage of the gear and consequently, a potential fault point.

Brushless Doubly-fed Induction Machines can also be employed to inject reactive power into the grid [3]. This feature especially distinguishes it from the conventional induction machines and makes it similar to synchronous machines in operation.

Moreover, as elucidated in [4], the BDFIM is also expected to exhibit better fault-ride through capability compared to the conventional DFIM; thereby, making it more likely to comply with the stricter grid regulations in the future.

1.2 Motivation

Before Brushless Doubly-fed Induction Machines can be proffered as a reliable market solution in the wind energy sector, it is imperative to gain deeper understanding of the operation of the machine under different conditions and to improve its performance characteristics as much as possible.

The machine, as will be shown in the next chapter, is unconventional in more than one way. Also, compared to other electrical machinery such as induction and synchronous machines, BDFIMs have been comparatively less studied in the past. Perhaps due to the recent advances made in power electronics and the desire to move deeper into offshore waters for harnessing wind energy, the interest in BDFIM has been rejuvenated. All these factors point towards the need for accurate modeling of the machine.

In order to capture various complex effects in electrical machines such as non-linear characteristics of the material, eddy currents and effects arising due to complex geometrical features amongst many others, finite element modeling presents a more viable and accurate way of modeling than analytical methods.

For Brushless Doubly-fed Induction Machines, both analytical and finite element models have been developed to gain deeper insight into the operational characteristics of the machine [5–12]. Finite element methods, as mentioned earlier, make it relatively easier to incorporate complexities due to slotting and saturation etc. compared to the analytical methods, although the latter is more insightful. The analysis carried out so far on BDFIM, including the ones referred to here, have focused on the magnetic flux density distribution in the airgap, estimation of the torque ripple and core loss inside the machine. In addition, equivalent circuit and parameter estimation models have also been developed. Some works also comment on the optimum number of pole-pair combination in BDFIMs. Finite element models which take non-linear characteristics of the iron into account have also been formulated. However, as far as the author is aware, all these models have been limited to two-dimensions and none has been extended to three-dimensions. In addition to those models, Wang and *et al.* [8], have developed a multi-slice 2D model to estimate the effect of skew in the machine, which could otherwise be accurately modeled only using 3D modeling. A small scale 3D study of BDFIM in frequency domain was actually carried out by Thompson in 1995 [13]. However, the system was limited to few thousand degrees of freedom which is quite limited for accurate modeling. Also, no methods were proposed for modeling of large scale models or those of practical dimensions. In other words, the applicability of the model was considerably restricted.

In addition to skew, end-winding effect is another facet which can be accurately modeled only in 3D. Besides these, the laminated structure of the iron inside electrical machines clearly points out the need for modeling of anisotropic materials. Obviously, this anisotropy in material properties can only be accounted for in 3D models. These areas of research are, to the knowledge of the author, unexplored for the BDFIM.

In a nutshell, we consider 3D modeling a necessity for accurate prediction of machine performance. Not only this, we strongly believe that it can serve as a benchmark to which various 2D models can be compared. This way even if we continue using 2D models, we can have a better idea about their accuracy and limitations.

1.3 Problem statement

The problem definition for this thesis can be put forth as follows:

To lay the foundation towards developing a 3D transient model for the Brushless Doubly-fed Induction Machine, including motion and circuit equations for the rotor, and to ascertain the feasibility of carrying out a 3D transient study.

1.4 Scope of the thesis

The problem definition stated in the previous section is a rather general statement and given the limitations of time, the scope of the thesis needs to be well defined as well as limited to certain aspects. Keeping this in mind, it is wise to establish the deliverables from this thesis as clearly as possible.

1.4.1 Research objectives

The research objectives have been enlisted in terms of milestones or goals below:

1. To build a 3D magnetostatic model of the BDFIM—with skewed and non-skewed rotor—to gain an understanding of the magnetic field distribution in the machine. The rotor currents in this case are taken from the 2D multi-slice model for the same machine.

2. To estimate the magnitude of the axial component of magnetic flux density, and its impact on the electromagnetic torque developed in the machine. This component of the magnetic field has been hitherto neglected in 2D models.

3. To comment on the validity of the 2D multi-slice model used for estimating the effect of skew on machine performance.

4. To describe the methods for building up a full-scale 3D transient models for BDFIM, discuss the feasibility of such a formulation and outline its limitations.

1.5 Outline for the thesis

This thesis has been divided into seven chapters. The main content in each chapter is enlisted below:

- **Chapter 2** gives an abridged version of the history of BDFIMs. An introduction about the operating principle and the skew in the machine is also presented.
- **Chapter 3** gives an account of the governing differential equations, corresponding boundary conditions and various magnetic potential formulations involved. Estimation of torque from potentials is also described.
- **Chapter 4** is intended to briefly describe the fundamentals of finite elements *viz.,* weak formulations, meshing in 3D and solving sparse system of linear equations arising from finite element discretization. Iterative methods, including multigrid preconditioners, are introduced.
- **Chapter 5** describes the steps involved in setting up of a 3D magnetostatic model of BDFIM for finite element approximation in COMSOL Multiphysics. Application of iterative solvers for solving large scale system of equations and the results obtained obtained from the magnetostatic model are also discussed.
- **Chapter 6** is an attempt to solve the transient model for the BDFIM, both in 2D and 3D, using iterative solvers. The chapter discusses the limitations encountered while implementing iterative solvers for the 3D transient analysis.
- **Chapter 7** summarizes the results obtained in this thesis and recommends some areas of scientific interest, left unexplored in this work, for further research.

Chapter 2

Brushless Doubly-fed Induction Machine

We are trying to prove ourselves wrong as quickly as possible, because only in that way can we find progress.—Richard Phillips Feynman

---

Chapter summary:

The chapter begins with a short historical account of the cascade induction machines culminating in present day Brushless Doubly-fed Induction Machines. The basic constructional features of the machine and its synchronous mode of operation are then presented. Subsequently, need for introducing the skew in the rotor and ways to incorporate it in the mathematical models developed so far are discussed.

2.1 A brief history

In the early 20th century, for applications requiring variable speed operations, DC machines were preferred. Speed control of induction machines using variable frequency power converters is a recent phenomenon. Initially for induction machines, speed control was mostly achieved by varying the rotor resistance in a wound rotor induction machine or by using a machine with multiple windings with variable number of poles. However, this affected the overall reliability and efficiency of the system. Steinmetz in his patent [14], in 1897, proposed a different alternative to achieve the speed control by operating two or more induction machines in cascade. This improved the efficiency of the system by cutting down on additional copper losses in the rotor resistance. Cascade operation of induction machines also made it suitable for low-speed applications. It should also be mentioned here that the cascade mode of control was also proposed independently by Görges in Germany, in the same year as Steinmetz. The cornerstone for the present day BDFIM was laid in these inventions.
There were, however, a few limitations with cascading two induction machines. Increased size due to two rotors and stators led to high costs, more copper losses in the stator, low power

factor, reduced efficiency and even decreased overload capacity [15]. After Steinmetz and Görges, others followed with further topological modifications to make the idea of cascading commercially more viable.

An important contribution came from Hunt in 1907. The idea was to accommodate two stator and rotor windings in the same machine. The problem in this case, however, was to ensure that no direct transformer like coupling occured between the two stator windings. According to Hunt, this could be achieved in two manners. First, proposed by Professor Thompson in 1901, who suggested dividing the stator windings into several sections with alternate sections comprising of coils from two different windings. Second, attributed to Lydall in 1902, who put forth the idea of having two separate stator windings wound for different number of pole-pairs [15]. Obviously, latter is a more practical way of alleviating the problem of direct coupling between the two stator windings. Further improvements in this direction were suggested by Creedy [16]. These type of machines were referred to as self-cascaded machines.

To optimize the performance characteristics of the self-cascaded machines, modifications with the rotor were necessary too. Earlier versions with two sets of rotor windings of appropriate pole numbers in a double layer configuration were replaced by more advanced designs resembling the cage rotor, due to their robustness. One such design was the *Nested-cage rotor* proposed by Broadway and Burbridge in 1970 [17]. We shall return to this point again in the next section.

In the late 20th century, after significant advances in power electronic technology, self-cascaded machines were a topic of interest again. More so, due to their potential applications as adjustable speed drives with fractionally rated converter. In 1994, Li and *et al.* [18] demonstrated the final version of the self-cascaded machine, now called the "Brushless Doubly-fed Machines" and outlined its operation in a similar manner to that of the synchronous machine. More recently in 2009, Blázquez and *et al.* [2], used the term "Brushless Doubly-fed Induction Machines" for these type of machines.

2.2 Construction and Synchronous Mode of Operation

The stator of the Brushless Doubly-fed Induction Machine has two windings, commonly referred to as the Power Winding (PW) and the Control Winding (CW). The power winding is connected directly to the grid and has a fixed voltage and frequency. On the other hand, the control winding is fed from the grid via a power electronic converter, with variable frequency and variable voltage output. Figure 2.1 depicts this configuration. PW and CW are wound with different number of pole pairs so that there is no direct coupling between the two. However, cross coupling between the two windings occurs via the rotor.

There are two primary sources of the magnetic field in the air-gap; one of them is due to the power winding and the other due to the control winding. The mathematical expressions for the magnetic flux densities due to these windings in the stator reference frame can be written as:

$$\boldsymbol{B_{ps}} = \boldsymbol{\hat{B}_{ps}}\ sin(\omega_p t - p_p\theta + \phi_p) \tag{2.1}$$

$$\boldsymbol{B_{cs}} = \boldsymbol{\hat{B}_{cs}}\ sin(\omega_c t - p_c\theta + \phi_c) \tag{2.2}$$

where, $\boldsymbol{B_{ps}}$ and $\boldsymbol{B_{cs}}$ represent the magnetic flux densities due to the power winding and the control winding respectively; $\boldsymbol{\hat{B}_{ps}}$ and $\boldsymbol{\hat{B}_{cs}}$ denote their corresponding amplitudes.

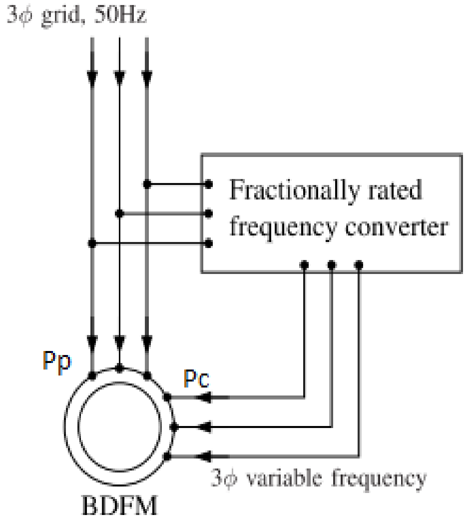

Figure 2.1: Configuration of BDFIM, as reproduced from [5].

ω_p and ω_c are the frequencies of the power winding and the control winding supplies respectively; p_p and p_c are their corresponding number of pole-pairs.

Expressing (2.1) and (2.2) in the rotor reference frame with the transformation:

$$\theta_s = \theta_r + \omega_m t \tag{2.3}$$

where, ω_m is the mechanical speed of the rotor (rad/s); we have:

$$\boldsymbol{B_{ps}} = \boldsymbol{\hat{B}_{ps}}\ sin((\omega_p - p_p\omega_m)t - p_p\theta_r + \phi_p) \tag{2.4}$$

$$\boldsymbol{B_{cs}} = \boldsymbol{\hat{B}_{cs}}\ sin((\omega_c - p_c\omega_m)t - p_c\theta_r + \phi_c) \tag{2.5}$$

For synchronous mode of operation, the frequency of both the magnetic flux densities in the rotor must be the same [6], which results in:

$$\omega_p - p_p\omega_m = \pm(\omega_c - p_c\omega_m) \tag{2.6}$$

Since, we are looking for the potential application of the BDFIM in wind turbines; we opt for the condition resulting in a lower ω_m:

$$\omega_p - p_p\omega_m = -(\omega_c - p_c\omega_m) = \omega_r \tag{2.7}$$

$$\omega_m = \frac{\omega_p + \omega_c}{p_p + p_c} \tag{2.8}$$

This speed ω_m given by (2.8) is termed as the *synchronous speed* of the BDFIM.
Another important mode of operation is when the control winding is fed with a DC supply or is short-circuited. The speed of synchronous operation in this case, as given by (2.8) is:

$$\omega_n = \frac{\omega_p}{p_p + p_c} \tag{2.9}$$

where, ω_n is now termed as the *natural speed* [7].

The resultant of the magnetic field densities due to the power winding and the control winding as given by (2.4) and (2.5), and using (2.7), can be written as:

$$\boldsymbol{B_s} = \hat{\boldsymbol{B}}_{\boldsymbol{ps}}\ sin(\omega_r t - p_p\theta_r + \phi_p) + \hat{\boldsymbol{B}}_{\boldsymbol{cs}}\ sin(\omega_r t - p_c\theta_r + \phi_c) \tag{2.10}$$

For the ease of analytical analysis, we assume $\hat{\boldsymbol{B}}_{\boldsymbol{ps}} = \hat{\boldsymbol{B}}_{\boldsymbol{cs}} = \hat{\boldsymbol{B}}_{\boldsymbol{s}}$. Equation (2.10) can then be reformulated as:

$$\boldsymbol{B_s} = \hat{\boldsymbol{B}}_{\boldsymbol{s}}\ sin(-\frac{p_p + p_c}{2}\theta_r + \frac{\phi_p + \phi_c}{2})\ cos(\omega_r t - \frac{(p_p - p_c)}{2}\theta_r + \frac{\phi_p - \phi_c}{2}) \tag{2.11}$$

As can be inferred from (2.11), the resultant magnetic field density in the air-gap has a standing wave like characteristics, though mathematically not completely identical to it. We can thus conclude that the resultant flux density in the air-gap has an equivalent of $(p_p + p_c)$ poles with a frequency of ω_r in the rotor reference frame [6]. The flux density wave travels in the airgap at a speed corresponding to ω_r rad/s with respect to the rotor. The machine itself rotates at a mechanical speed given by (2.8).

As mentioned earlier, earlier developments in rotor design began with the two sets of windings of appropriate pole numbers in a double layer configuration. However, on subsequent analysis of star slot diagrams in rotor led to the development of the *Nested-cage rotor*. This is well explained by Broadway and Burbridge [17]. Nested-cage rotors are an advanced version of the conventional squirrel-cage rotor and allows for better cross-coupling between the power winding and the control winding. Number of nests, N_r is equal to the number of equivalent poles developed in the rotor, which then taking (2.11) into account becomes:

$$N_r = p_p + p_c \tag{2.12}$$

An example of the Nested-loop rotor in BDFIM is shown in Figure 2.2. The number of loops within a nest depends on the number of rotor slots available. More slots lead to a lower referred rotor-slot leakage reactance [17]. A higher number of loops, in principle, also reduce the harmonic content of the rotor and the torque ripple. However, one should be careful of the cost implications and also be mindful of the fact that a higher number of loops can result in coupling of higher order harmonics and therefore, increase in torque ripple [6]. Nested-cage rotors are preferred because of their robustness and simplicity of design. An important point worth mentioning here is that it is not the only design for BDFIM rotors, alternative designs also exist.

It should be noted that in the above analysis, we have neglected the magnetic field due to the rotor currents. This assumption can be justified by the fact that additional current in stator windings is drawn to overcome the effect of rotor currents, whereas the primary magnetizing current and thus, the magnetizing flux is maintained constant in the air-gap [6].

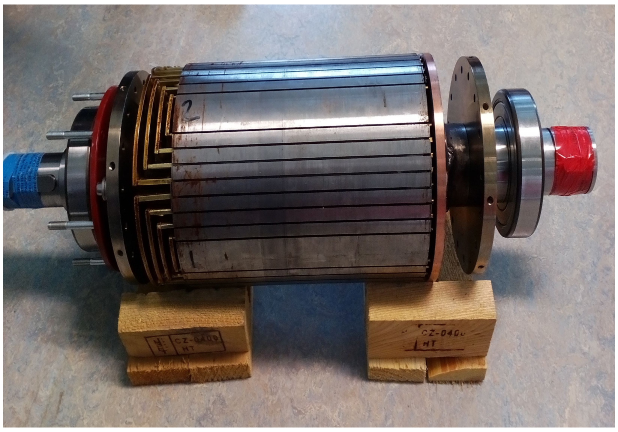

Figure 2.2: An example of Nested cage rotor used in BDFIM.

2.3 Skew in the Nested Cage rotor

Quite often in rotating electrical machines, conductor slots—or for that matter even magnets—are skewed. There are various advantages of employing skew in these machines. Minimizing the cogging torque and smoothening of the back emf are paramount amongst them [19]. Attenuation of the cogging torque invariably implies mitigation of the torque ripple. Figure 2.3 shows a skewed nested cage rotor used in the BDFIM. The rotor slots are skewed by one stator slot, which in this case is 5 degrees.

Figure 2.3: Skewed Nested cage rotor.

The concept of skewing is based on the idea of minimizing the variation of the reluctance along the tangential direction. Implementing the skew nevertheless comes at a cost. Skewing the slots means increase in the slot length and hence, associated increase in the copper losses. It might also result in reducing the maximum flux linkage corresponding to a current loop in the rotor, thereby reducing the induced current in the rotor and the average torque. For machines, with sinusoidal or square wave flux densities, the decrease in the induced emf in the rotor can be taken care of by using the skew factor [20]. However, it is not so straightforward to implement a similar skewing factor in case of the BDFIM, given the complex shape of magnetic flux density in the airgap, given by (2.11). The high space harmonic content in the

airgap magnetic flux density in a BDFIM has been highlighted in [6, 8, 9].
Moreover, due to skew, the force generated has two components—one in the tangential direction and the other along the axial direction. The axial component of the force results in a screw like effect, leading to additional thrust on the rotor bearings [20]. In principle, either of the stator slots or the rotor slots can be skewed. The choice is usually determined by the ease of fabrication, minimizing the copper losses, etc.
Skewing can have an impact on the stray load loss and the no-load loss in the machine. The presence of the axial component of the flux can also result in additional eddy losses in the iron. Besides, due to non-homogeneity along the axial direction, the skew is responsible for asymmetric distribution of flux. This asymmetrical distribution in flux is partly due to the tangential component of the rotor current, partly owing to the relative phase shift between the stator and the rotor conductors and partly, due to the change in the reluctance of the flux paths from one end to the other end of the machine. Skewing is employed almost always in case of the small machines, however, for the large machines, skewing need not always be the best option [21].

2.4 Modeling of skew in electrical machinery

Field modeling of electrical machines, to be precise, is a three-dimensional problem. However, to keep things simple and yet be able to deduce pragmatic results within the acceptable limits of accuracy, we often prefer two-dimensional modeling. This approach is justified by the fact that for most machines, a certain cross-sectional area remains the same along one of the principal axis of the machine. In other words, most electrical machines are more or less homogeneous along the axial direction. 2D modeling while giving acceptable results has certain limitations and inherently involves some approximations. For instance, the anisotropy of the stator and the rotor iron due to their laminated structure is disregarded. End winding effects are also usually neglected in 2D modeling. Skew in the rotor, in particular, is a case where a simple 2D modeling can have limited accuracy. Usually to account for skew in the rotor, a multi-slice 2D model has been used [8, 22, 23].

Nonetheless, a more accurate understanding of the skew and other aforementioned effects can only be achieved by means of a full scale 3D transient model. Several papers have discussed the 3D model for an induction machine in order to understand the effect of skew on core losses and torque characteristics [24–26]. However, a similar study for the BDFIM, as far as the author's knowledge is concerned, has not been carried out so far. Given the complex shape of the airgap magnetic flux density in the BDFIM compared to the conventional induction machines, it should be worthwhile to pursue a similar study on the BDFIM, to gain a deeper insight into the effects of skew on loss and torque characteristics.
The methodology adopted to do the same has been explained in the following chapters.

2.5 Machine geometry

The parameters for the BDFIM model used in this thesis are listed in Table 2-1. The data values correspond to the BDFIM prototype present at the EEMCS faculty at TU Delft.
A 2D representative diagram of the machine is shown in Figure 2.4. The region shaded in

blue represents the air-gap. The bottom conductors in each stator slot belong to the power winding whereas the top conductors belong to the control winding.

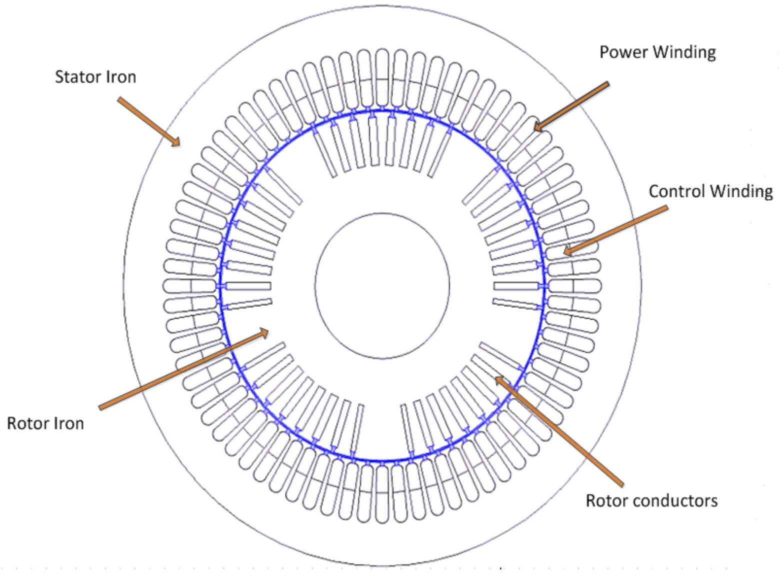

Figure 2.4: A 2D representation of the BDFIM geometry.

Machine Parameter	Value
PW phases	3
CW phases	3
PW pole pairs	2
CW pole pairs	3
PW slots/pole/phase	6
CW slots/pole/phase	4
Stator slots	72
Stack length	0.240 m
Airgap length	0.001 m
Stator Outer radius	0.135 m
Stator Inner radius	0.085 m
Rotor Bore radius	0.035 m
Rotor slots	40
Rotor nests	5
Rotor loops per nest	4

Table 2-1: Parameters for the BDFIM

Chapter 3

Maxwell equations and Mathematical preliminaries

The physicist, in his study of natural phenomena, has two methods of making progress: (1) the method of experiment and observation, and (2) the method of mathematical reasoning. The former is just the collection of selected data; the latter enables one to infer results about experiments that have not been performed. There is no logical reason why the second method should be possible at all, but one has found in practice that it does work and meets with reasonable success.—Paul Adrien Maurice Dirac

---

Chapter summary:

This chapter describes the governing differential equations for the analysis that follows in the subsequent chapters. Various magnetic potential formulations along with the relevant boundary conditions are discussed. Retrieving the physical quantities of interest such as torque from the solution of these differential equations is also explained.

3.1 Maxwell equations

Maxwell equations are the fundamental building blocks of the classical electrodynamics. The set of equations put forth by James Clerk Maxwell, later expressed in a more compact differential form are expressed below:

$$\nabla \cdot \boldsymbol{D} = \rho \tag{3.1}$$

$$\nabla \times \boldsymbol{E} = -\frac{\partial \boldsymbol{B}}{\partial t} \tag{3.2}$$

$$\nabla \cdot \boldsymbol{B} = 0 \tag{3.3}$$

$$\nabla \times \boldsymbol{H} = \boldsymbol{J} + \frac{\partial \boldsymbol{D}}{\partial t} \tag{3.4}$$

where, $\boldsymbol{D}$ is the electric flux density $[C/m^2]$
ρ is the free charge density $[C/m^3]$
$\boldsymbol{E}$ is the electric field intensity $[V/m]$
$\boldsymbol{B}$ is the magnetic flux density $[T]$
$\boldsymbol{H}$ is the magnetic field intensity $[A/m]$
$\boldsymbol{J}$ is the current density $[A/m^2]$

These equations together with the Lorentz force law and the Newton's laws of motion can be used to describe almost all classical electromechanical energy conversions [27]. And as such, all rotating electrical machines can be analyzed by the application of the Maxwell equations. In this thesis, we apply this set of equations to the brushless doubly-fed induction machine, with slight modifications wherever necessary[1]. The idea is to calculate and understand the field distributions inside the physical dimensions of the machine, and subsequently based on that information estimate practical quantities of interest such as electromagnetic torque developed and core loss in the machine.

3.2 Constitutive relations

The electric and magnetic field vectors in the Maxwell equations are related to each other by the so-called *constitutive relations.* These relationships are expressed in the form of equations below:

$$\boldsymbol{D} = \epsilon_0 \epsilon_r \boldsymbol{E} = \epsilon \boldsymbol{E} \tag{3.5}$$

where, ϵ_0 and ϵ_r represent the permitivitty of free space and the relative permitivitty of the material.

Similarly[2],

$$\boldsymbol{B} = \mu_0 \mu_r \boldsymbol{H} = \mu \boldsymbol{H} \tag{3.6}$$

where, μ_0 and μ_r represent the permeability of the free space and the relative permeability of the material respectively.
For anisotropic materials, the permeability is treated as a tensor quantity as shown in (3.7) below:

$$\overset{\leftrightarrow}{\mu} = \begin{bmatrix} \mu_{xx} & \mu_{xy} & \mu_{xz} \\ \mu_{yx} & \mu_{yy} & \mu_{yz} \\ \mu_{zx} & \mu_{zy} & \mu_{zz} \end{bmatrix} \tag{3.7}$$

Clearly, the same applies for other material properties such as permitivitty, electrical conductivity and so on[3].

---

[1] For instance, in this work we neglect any displacement current effects. Equation (3.4) then reduces to the Ampere's Law.

[2] The relation is different if magnets are involved.

[3] Equation (3.5) becomes $\boldsymbol{D} = \epsilon \cdot \boldsymbol{E}$. Same applies for (3.6) .

3.2.1 Non-linear relations

The constitutive relations presented above are also in general, non-linear. A commonly encountered effect in the iron part of the electrical machines is that of the saturation. Saturation refers to the phenomenon when the magnetic flux density inside the material starts approaching a fixed value despite increase in the magnetic field intensity. A typical $\boldsymbol{HB}$-curve is shown in Figure 3.1.

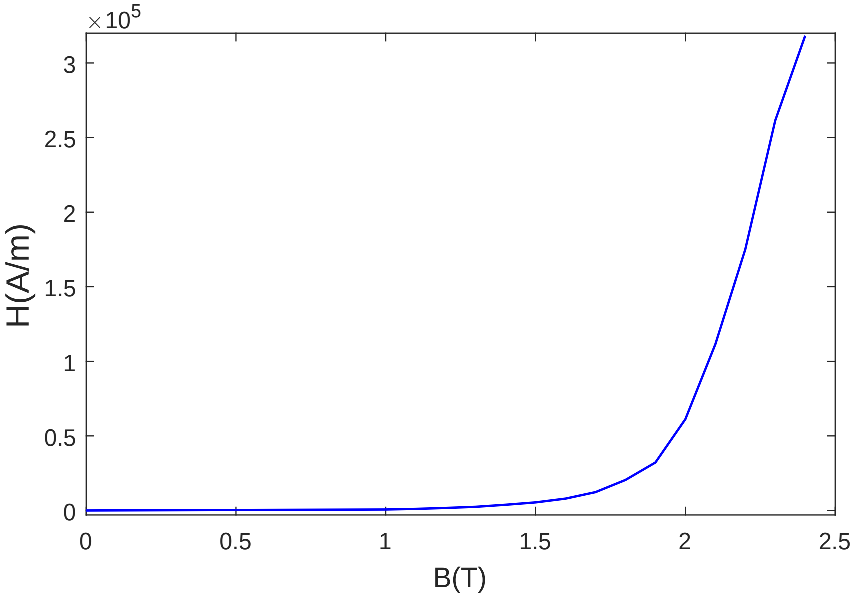

Figure 3.1: Typical HB curve for iron in machines

Here, we have neglected the multi-valued nature of the $\boldsymbol{HB}$-curve.
In context of this thesis, we shall mostly assume linear properties for all the materials involved, unless mentioned otherwise.
Usually in textbooks, we find a $\boldsymbol{BH}$-curve rather than a $\boldsymbol{HB}$-curve. The reason we have opted for the latter is that the magnetic flux density is directly related to the magnetic vector potential, which is the primary dependent variable in the model. Thus, the magnetic field intensity in such models is derived from the magnetic flux density and not vice-versa.

3.3 Magnetic Vector Potential

From (3.3) it follows that the magnetic flux density $\boldsymbol{B}$ can be expressed as the curl of a vector field $\boldsymbol{A}$. This argument stems from the fact that the divergence of the curl of any vector field is always zero. Mathematically put:

$$\boldsymbol{B} = \nabla \times \boldsymbol{A} \tag{3.8}$$

where, $\boldsymbol{A}$ is the magnetic vector potential $[Tm]$

Using (3.6) and (3.7), and assuming no displacement current effects, we can rewrite (3.4) as:

$$\nabla \times (\frac{1}{\mu}\nabla \times \boldsymbol{A}) = \boldsymbol{J} \tag{3.9}$$

For a simple case where μ is assumed to be constant over the region of interest, the above equation takes the form[4]:

$$\nabla(\nabla \cdot \boldsymbol{A}) - \nabla^2 \boldsymbol{A} = \mu \boldsymbol{J} \tag{3.10}$$

Where, $\nabla^2 \boldsymbol{A}$ represents the vector Laplacian of $\boldsymbol{A}$.
In this form, it is much easier to impose the gauge on $\boldsymbol{A}$, as explained next.

3.3.1 The Gauge of A

The only constraint on the magnetic Vector potential $\boldsymbol{A}$ is that its curl must be equal to $\boldsymbol{B}$. There is no such restriction on the divergence of $\boldsymbol{A}$. This fact can be exploited for mathematical convenience, and the choice for $\nabla \cdot \boldsymbol{A}$ is then usually made according to the problem. In other words, we might impose one value for the divergence of $\boldsymbol{A}$ in magnetostatic problems and another in case of other problems [27].

This arbitrary fixing of $\nabla \cdot \boldsymbol{A}$ is termed as the *gauge fixing.* In case of $\boldsymbol{A}$, any such changes to $\boldsymbol{A}$, which ensures that its curl remains unaltered is acceptable. Knowing that the curl of a gradient is always zero, we can with impunity add the gradient of any scalar function ψ to $\boldsymbol{A}$ for our convenience, without affecting $\boldsymbol{B}$. Specifying the gauge implies ensuring the uniqueness on $\boldsymbol{A}$.
Some of the commonly employed gauge transformations are the Coulomb Gauge, the Lorentz Gauge and the Diffusion Gauge. In magnetostatic problems, it is the Coulomb Gauge that is widely used [28]. Using Coulomb Gauge, implies opting for $\nabla \cdot \boldsymbol{A} = 0$. Equation (**??**) then becomes:

$$-\frac{1}{\mu}\nabla^2 \boldsymbol{A} = \boldsymbol{J} \tag{3.11}$$

Quite often it is the case that no specific choice is made for the divergence of $\boldsymbol{A}$, in so called *ungauged* vector formulations. This however, does not mean that no choice whatsoever is made for $\nabla \cdot \boldsymbol{A}$, but that any reasonable choice works equally well. It is not possible to numerically arrive at the solution of the potential unless some choice is made. This choice is sometimes hidden in the formulations with implicit enforcement of the Coulomb gauge and at others, is made by the computer, through the numerical round off error mechanism. Specifying the gauge whenever possible should be done to avoid numerical instabilities [29]. These numerical issues are mostly encountered in 3D. For 2D problems, the gauge is always satisfied.

3.3.2 Boundary conditions for A

To solve a boundary value problem in $\boldsymbol{A}$ inside the domain Ω, it is mandatory to specify the appropriate boundary conditions on its boundary Γ, i.e. on $\Gamma = \partial\Omega$. Boundary conditions

---

[4] Using the vector identity: $\nabla \times (\nabla \times \boldsymbol{V}) = \nabla(\nabla \cdot \boldsymbol{V}) - \nabla^2 \boldsymbol{V}$

can be specified either in terms of the tangential component or the normal component of the magnetic field. In general, we can suppose that the boundary is composed of two disjoint boundary parts, i.e. $\Gamma = \Gamma_H \cup \Gamma_B$.

Suppose, on Γ_H, the tangential component of the magnetic field is known a priori:

$$\boldsymbol{H} \times \boldsymbol{n} = \boldsymbol{K} \tag{3.12}$$

where, $\boldsymbol{K}$ is the surface current density and $\boldsymbol{n}$ is the outward normal on Γ_H. Reformulating the above equation in terms of $\boldsymbol{A}$, we get:

$$(\frac{1}{\mu}\nabla \times \boldsymbol{A}) \times \boldsymbol{n} = \boldsymbol{K} \tag{3.13}$$

This represents a Neumann type boundary condition.

Similarly suppose on Γ_B, the normal component of the field is known. Then, we can write:

$$\boldsymbol{B} \cdot \boldsymbol{n} = b \tag{3.14}$$

In terms of $\boldsymbol{A}$, it becomes:

$$(\nabla \times \boldsymbol{A}) \cdot \boldsymbol{n} = b \Rightarrow \nabla \cdot (\boldsymbol{n} \times \boldsymbol{A}) = -b \tag{3.15}$$

Or in a more succinct manner as:

$$\boldsymbol{n} \times \boldsymbol{A} = \alpha \tag{3.16}$$

where, $\nabla \cdot \alpha = -b$. This represents a Dirichlet type boundary condition [30].

3.4 Magnetic Scalar Potential

For regions with zero current density, the curl of the magnetic field intensity $\boldsymbol{H}$ is zero from (3.4). Therefore, in such cases, it is possible to express the magnetic field intensity $\boldsymbol{H}$ as a gradient of the scalar potential ϕ, rather than expressing it as a curl of any vector potential.

$$\boldsymbol{H} = -\nabla\phi \tag{3.17}$$

3.4.1 Boundary conditions for ϕ

In this case, again the boundary can be divided into two regions: (1) satisfying the Dirichlet condition on Γ_D, and (2) satisfying the Neumann condition on Γ_N, i.e. $\Gamma = \Gamma_D \cup \Gamma_N$.

For the sake of generality, we specify non-homogeneous boundary conditions here.

On Γ_D,

$$\phi = \phi_0 \tag{3.18}$$

On Γ_N,

$$\nabla\phi \cdot \boldsymbol{n} = \beta \tag{3.19}$$

3.4.2 Comparison with Vector formulation

There are some obvious advantages of the scalar formulation over the vector formulation, as and when it can be applied. Firstly, the information about the magnetic field is contained in a scalar number rather than a vector with three components [28]. Secondly, it is much simpler and requires fewer computations to calculate the scalar potential than the vector potential. From computational perspective, it is efficient both in terms of memory and time cost. On the other hand, if the problem domain involves materials with relative permeability values differing by a few orders of magnitude, scalar potential formulation may not work optimally in a problem involving both scalar and vector potential domains. These points shall be addressed as and when they appear in the subsequent chapters.

3.5 Mixed formulation

It is also possible to use both the scalar and the vector potential formulations in the same model. This type of formulation is termed as the mixed potential formulation, or sometimes just mixed formulation. Mixed formulations are mostly employed in 3D models, to exploit the advantages of the scalar potential, as mentioned above. In 2D, since only one component of the vector potential is needed, therefore, it is not a big concern in terms of number of degrees of freedom involved.

In this section we shall mostly limit ourselves to the necessary boundary conditions at the interface between the scalar and the vector potential regions. The governing equations in the interior of the domains are same as described above, depending whether the domain is defined by the scalar or the vector potential.

Let Ω_A and Ω_ϕ represent the vector and the scalar potential regions respectively, and $\Gamma_{A,\phi}$ denote the interface between these two regions. Also, let $\boldsymbol{n}_A$ and $\boldsymbol{n}_\phi$ represent the outward normals on the interface from the vector and the scalar potential regions respectively. See Figure 3.2.

In accordance with the Ampere's Law and the Gauss' Law for magnetism, the tangential component of the magnetic field intensity and the normal component of the magnetic flux density need to be continuous on the material boundaries[5]. Mathematically put, this implies:

$$
\begin{aligned}
(\frac{1}{\mu}\nabla \times \boldsymbol{A}) \times \boldsymbol{n}_A - \nabla\phi \times \boldsymbol{n}_\phi = 0 \\
(\nabla \times \boldsymbol{A}) \cdot \boldsymbol{n}_A - \mu\nabla\phi \cdot \boldsymbol{n}_\phi = 0
\end{aligned}
\tag{3.20}
$$

The usual PDEs are applicable inside the scalar and the vector potential regions. Similarly, the boundary conditions as outlined in the previous sections remain true on the external boundaries.

3.6 Maxwell Stress Tensor

There are several ways to calculate torque on the rotor in an electrical machine [23]. Though every method has its pros and cons, usually they result in the same final result. Therefore, one

---

[5] Assuming no surface currents on the boundary.

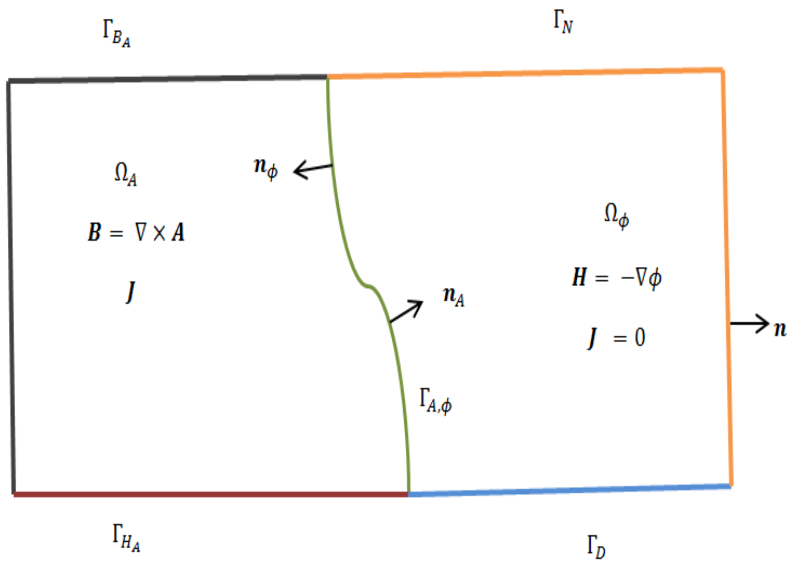

Figure 3.2: Mixed potential formulation

may adopt any one of those depending upon the ease of calculation it offers or the accuracy desired. In this thesis, we opt for the torque calculation using the Maxwell Stress Tensor (MST) method. For detailed reasoning and the explanation of the Stress Tensor method, see [23, 28].

The method of Maxwell stress tensor has been quite widely applied for calculation of torque in electrical machines. MST method relies on the knowledge of field quantities rather than usual electrical or mechanical state variables like current, voltage, speed etc. The information about field quantities is now readily available due to numerical methods like finite elements, and modern computers. This also explains why the stress tensor method was not usually preferred earlier as it can be cumbersome to calculate field quantities rather accurately using analytical methods [23].

To evaluate the magnetic force on a body using the MST method, the information about the field quantities is required on any surface enclosing the body. In case of electrical machines then, the tangential force on the rotor can be calculated by knowing the magnetic field intensity or the magnetic flux density in the air-gap. An optimal surface for this purpose is a cylindrical one in the air-gap enclosing the rotor.

If Γ is one such surface in the air-gap , then the electromagnetic torque is given by the following surface integral [31]:

$$\boldsymbol{T}_e = \oint_\Gamma \boldsymbol{r} \times \overset{\leftrightarrow}{T} \cdot \, d\Gamma \tag{3.21}$$

where, $\boldsymbol{r}$ is the radius of the cylindrical surface inside the air-gap and $\overset{\leftrightarrow}{T}$ is the Maxwell stress tensor.

In physical terms, $\overset{\leftrightarrow}{T}$ represents the force per unit area. Mathematically, $\overset{\leftrightarrow}{T}$ can be expressed as:

$$\overset{\leftrightarrow}{T} = \begin{bmatrix} T_{xx} & T_{xy} & T_{xz} \\ T_{yx} & T_{yy} & T_{yz} \\ T_{zx} & T_{zy} & T_{zz} \end{bmatrix} \tag{3.22}$$

Here, T_{ij} represents the force acting along the ith direction on the surface element pointing towards the jth direction. In other words, T_{ii}'s can be used to express the pressure forces, whereas the T_{ij}'s represent the shear forces [23]. Thus, to calculate the force in the y-direction on the surface pointing in the x-direction, the element T_{yx} is responsible. The stress tensor above has been expressed in the cartesian coordinate system. It can easily be extended to other coordinate systems. For instance, consider a cylindrical coordinate system, which is a natural coordinate system for geometries similar to that of rotating electrical machines. Then the tangential force can be evaluated by computing the integral of $T_{\theta r}$ element of the stress tensor matrix on the cylindrical surface in the air-gap. Obviously, this surface points in the radial direction.

In case of 2D, the integral in (3.20) becomes the line integral, and the total torque is evaluated by multiplying the integral with the axial length of the machine, l. For the sake of brevity, we only write the simplified form of (3.21) here:

$$\boldsymbol{T}_e = l \oint rF_\theta \, ds \tag{3.23}$$

where, F_θ is the tangential force density and is given by:

$$F_\theta = \frac{1}{\mu_0} \, B_r B_\theta \tag{3.24}$$

where, B_r and B_θ denote the radial and the tangential components of the magnetic flux density respectively. Several modifications to the above method and recommendations with respect to meshing have been proposed to alleviate the numerical issues that arise on account of moving mesh in finite element modeling [23, 31].

For torque calculation in 3D, the multiplication with the axial length is not required and the original surface integral can be evaluated on the curved surface of the cylinder. For 3D models, (3.23) becomes:

$$\boldsymbol{T}_e = \frac{1}{\mu_0} \iint_\Gamma r \; B_r B_\theta \; \, d\Gamma \tag{3.25}$$

The components of the magnetic flux density $\boldsymbol{B}$ used in the above equations are retrieved by evaluating the curl of the magnetic vector potential. This follows from the definition of $\boldsymbol{A}$, as per (3.8).

Chapter 4

Finite Element Modeling

All the mathematical sciences are founded on relations between the physical laws and the laws of numbers, so that the aim of exact science is to reduce the problems of nature to the determination of quantities by operations with numbers.—James Clerk Maxwell

---

Chapter summary:

The chapter is meant to be a brief introduction to the finite element method. A step-by-step approach to solve a partial differential equation using the finite element method is presented. We begin by expressing the PDE in the weak form. Subsequently, elements used in meshing and the expansion functions associated with the nodal and the edge elements are discussed. Finally, we present some of the methods implemented to solve the resulting system of algebraic equations.

4.1 Introduction to FEM

Almost all of our analysis of the physical phenomena are based on their differential equation models. Solutions of such *boundary value problems* are indispensable to our understanding of nature. Analytical solutions of such problems are in general, extremely difficult, and almost invariably we rely on the numerical methods to obtain approximate solutions. Finite element analysis is one such numerical technique employed to arrive at the solution of these problems. Finite element approximation is basically a four step process. The first step is to express the unknown of interest in the relevant PDE implicitly, in terms of predetermined interpolation or expansion functions associated with each node (or edge) within an element, also known as *weak formulation* in finite element literature. The second step would be to divide the problem domain into small (or finite) discretized elements, a process known as *meshing.* In the next step we transform the weak form into a system of algebraic equations. And finally, the weight associated with each node(or edge), by solving this system of algebraic equations, is calculated. Initially finite element methods were employed to solve problems pertaining to structural analysis. For problems in electrodynamics or wave phenomena, the method was applied a little later.

Boundary value problems arising from the governing differential equations are typically of the form:

$$\hat{L}\phi = f \tag{4.1}$$

where, $\hat{L}$ is the differential operator
ϕ is the field quantity to be determined; and
f is the forcing or source term.
The equation is valid over domain Ω and with boundary conditions imposed on $\Gamma = \partial\Omega$.

Most commonly employed methodologies in developing a solution from the finite element methods are the *variational method* (or the *Ritz method*) and the *method of weighted residuals* (also known as *Petrov-Galerkin method*). In this text, we limit ourselves to the latter; as it does not require formulating an additional functional, unlike the former, which can at times be cumbersome [35].

4.2 Method of weighted residuals

In FEM, the primary dependent variable inside an element is approximated by using a predefined interpolation function, usually a polynomial. If the domain is discretized into N elements, then the primary dependent variable approximation $\hat{\phi}$ is given by:

$$\hat{\phi} = \sum_{n=1}^{N} c_n w_n = W^T C \tag{4.2}$$

where, c_n is the value of the unknown degrees of freedom, and w_n is the polynomial interpolation function.

The method of weighted residuals essentially relies upon the idea that for $\hat{\phi}$ to be a good approximate solution for (4.1), the residual r given below should be minimized:

$$r = \hat{L}W^T C - f \tag{4.3}$$

If u be the weighting function, then the solution to (4.1) can be obtained by imposing:

$$\iiint_\Omega u_j r \;\; d\Omega = 0 \tag{4.4}$$

Or in another form as:

$$(\iiint_\Omega U L W^T d\Omega) C = \iiint_\Omega U f d\Omega \tag{4.5}$$

where, $U = \{u_j\}$ and $j = 1, 2, 3..., N$.

One special case of the Petrov-Galerkin method is when the weighting function and the interpolation function are taken to be the same. This special class of FEM approximation is known as the *Galerkin method.*

4.3 Weak formulations

4.3.1 Regions with Scalar potential formulation

For regions with zero current density, the magnetic field intensity $\boldsymbol{H}$ can be expressed as the gradient of the Magnetic scalar potential ϕ. For better readability, we repeat (3.16) here:

$$\boldsymbol{H} = -\nabla\phi \tag{4.6}$$

Then using equations (3.3) and (3.6), we can write:

$$-\nabla\cdot\mu\nabla\phi = 0 \tag{4.7}$$

If V be the weighting function in the domain Ω surrounded by the boundary $\Gamma = \partial\Omega$. Then integrating throughout the domain Ω we get:

$$-\iiint_\Omega V(\nabla\cdot\mu\nabla\phi)d\Omega = 0 \tag{4.8}$$

For sake of brevity, henceforth, we shall use $\int_\Omega \equiv \iiint_\Omega$. Rewriting the above equation in a more compact form:

$$-\int_\Omega V(\nabla\cdot\mu\nabla\phi)d\Omega = 0 \tag{4.9}$$

Using the identity $\nabla\cdot(u\mathbf{v}) = \mathbf{v}\cdot\nabla u + u\nabla\cdot\mathbf{v}$; we obtain:

$$-\int_\Omega V(\nabla\cdot\mu\nabla\phi)d\Omega = \int_\Omega \mu(\nabla\phi\cdot\nabla V)d\Omega - \int_\Omega \nabla\cdot V(\mu\nabla\phi)d\Omega \tag{4.10}$$

We can rewrite the above equation using the Divergence theorem as:

$$-\int_\Omega V(\nabla\cdot\mu\nabla\phi)d\Omega = \int_\Omega \mu(\nabla\phi\cdot\nabla V)d\Omega - \int_\Gamma V(\mu\nabla\phi\cdot\mathbf{n})d\Gamma \tag{4.11}$$

where, $\mathbf{n}$ is the outward normal on the surface Γ.

Interchanging V and ϕ in 4.11, since both are scalar functions, leads to:

$$-\int_\Omega \phi(\nabla\cdot\mu\nabla V)d\Omega = \int_\Omega \mu(\nabla\phi\cdot\nabla V)d\Omega - \int_\Gamma \phi(\mu\nabla V\cdot\mathbf{n})d\Gamma \tag{4.12}$$

From (4.11) and (4.12), we have:

$$-\int_\Omega V(\nabla\cdot\mu\nabla\phi)d\Omega = -\int_\Omega \phi(\nabla\cdot\mu\nabla V)d\Omega + \int_\Gamma \phi(\mu\nabla V\cdot\mathbf{n})d\Gamma - \int_\Gamma V(\mu\nabla\phi\cdot\mathbf{n})d\Gamma \tag{4.13}$$

Let the approximate solution for the scalar potential be $\tilde{\phi}$; then $\tilde{\phi}$ should also satisfy (4.13), i.e.:

$$-\int_{\Omega} V(\nabla\cdot\mu\nabla\tilde{\phi})d\Omega = -\int_{\Omega}\tilde{\phi}(\nabla\cdot\mu\nabla V)d\Omega + \int_{\Gamma}\tilde{\phi}(\mu\nabla V\cdot\mathbf{n})d\Gamma - \int_{\Gamma} V(\mu\nabla\tilde{\phi}\cdot\mathbf{n})d\Gamma \quad (4.14)$$

Subtracting (4.13) from (4.14), and using (4.9) :

$$-\int_{\Omega} V(\nabla\cdot\mu\nabla\tilde{\phi})d\Omega = -\int_{\Omega}(\tilde{\phi}-\phi)(\nabla\cdot\mu\nabla V)d\Omega + \int_{\Gamma}(\tilde{\phi}-\phi)(\mu\nabla V\cdot\mathbf{n})d\Gamma - \int_{\Gamma} V\{\mu\nabla(\tilde{\phi}-\phi)\cdot\mathbf{n})\}d\Gamma \quad (4.15)$$

As alluded to in the previous chapter, the boundary $\Gamma = \partial\Omega$ can be divided into two disjunct regions: (1) satisfying the Dirichlet condition on Γ_D; and (2) satisfying the Neumann condition on Γ_N .

Since, the values of the primary dependent variable are specified on Γ_D, we opt for the weighting function, V such that $V = 0$ on Γ_D.

On Γ_N, we use the equation (3.18), repeated here,

$$\nabla\phi\cdot\mathbf{n} = \beta \quad (4.16)$$

For $\tilde{\phi}$ to be a good approximation $\tilde{\phi} \simeq \phi$. Using (4.16), equation (4.15) then reduces to:

$$-\int_{\Omega} V(\nabla\cdot\mu\nabla\tilde{\phi})d\Omega + \int_{\Gamma_N} V\{\mu\nabla\tilde{\phi}\cdot\mathbf{n} - \beta\}d\Gamma = 0 \quad (4.17)$$

Integrating the first integral in (4.17) by parts and simultaneously applying the Divergence theorem, we obtain:

$$\int_{\Omega}\mu(\nabla\tilde{\phi}\cdot\nabla V)d\Omega - \int_{\Gamma_N} V\{\mu\nabla\tilde{\phi}\cdot\mathbf{n}\}d\Gamma + \int_{\Gamma_N} V\{\mu\nabla\tilde{\phi}\cdot\mathbf{n} - \beta\}d\Gamma = 0 \quad (4.18)$$

Or,

$$\int_{\Omega}\mu(\nabla\tilde{\phi}\cdot\nabla V)d\Omega - \int_{\Gamma_N} V\beta d\Gamma = 0 \quad (4.19)$$

Equation (4.19) represents the weak form in the domain with the scalar potential formulation.

4.3.2 Regions with Vector potential formulation

The relevant PDE to be solved is:

$$\nabla\times(\frac{1}{\mu}\nabla\times\boldsymbol{A}) = \boldsymbol{J} \quad (4.20)$$

We repeat the boundary conditions mentioned already in Section 3-3-2, for better readability here. On Γ_H,

$$\frac{1}{\mu}(\nabla \times \boldsymbol{A}) \times \boldsymbol{n} = \boldsymbol{K} \tag{4.21}$$

On Γ_B,

$$\boldsymbol{n} \times \boldsymbol{A} = \alpha \tag{4.22}$$

Gauged Vector potential

In addition to the boundary conditions in (4.22) and (3.12), imposing the Coulomb gauge results in the following additional boundary conditions:

$$\boldsymbol{A} \cdot \boldsymbol{n} = 0, \qquad \text{on } \Gamma_H \tag{4.23}$$

$$\frac{1}{\mu}\ \nabla \cdot \boldsymbol{A} = 0, \qquad \text{on } \Gamma_B \tag{4.24}$$

For details on these additional boundary conditions, see [30].

Applying the method of weighted residuals using the vector weighting function $\boldsymbol{W}$, we obtain:

$$\begin{aligned}\int_\Omega \boldsymbol{W} \cdot [\nabla \times (\frac{1}{\mu}\nabla \times \tilde{\boldsymbol{A}}) - \nabla(\frac{1}{\mu}\nabla \cdot \tilde{\boldsymbol{A}})]d\Omega + \int_{\Gamma_H} \boldsymbol{W} \cdot [\frac{1}{\mu}(\nabla \times \tilde{\boldsymbol{A}}) \times \boldsymbol{n} - \boldsymbol{K}]d\Gamma \\ + \int_{\Gamma_B} [\frac{1}{\mu}(\nabla \cdot \tilde{\boldsymbol{A}})](\boldsymbol{W} \cdot \boldsymbol{n})d\Gamma = \int_\Omega \boldsymbol{W} \cdot \boldsymbol{J} \quad d\Omega\end{aligned} \tag{4.25}$$

where, $\tilde{\boldsymbol{A}}$ denotes the approximate solution for the vector potential.
Dirichlet conditions for $\boldsymbol{A}$ also imply:

$$\begin{aligned}\boldsymbol{W} \cdot \boldsymbol{n} = 0 \qquad & \text{on} \quad \Gamma_H \\ \boldsymbol{W} \times \boldsymbol{n} = 0 \qquad & \text{on} \quad \Gamma_B\end{aligned} \tag{4.26}$$

In other words, the weighting function must vanish on the boundaries where the components of A have been explicitly defined.
Considering the first term of (4.25) on LHS, and applying the following identities:

$$\begin{aligned}\nabla \cdot \phi \boldsymbol{v} = \boldsymbol{v} \cdot \nabla\phi + \phi\nabla \cdot \boldsymbol{v} \\ \nabla \cdot (\boldsymbol{u} \times \boldsymbol{v}) = \boldsymbol{v} \cdot (\nabla \times \boldsymbol{u}) - \boldsymbol{u} \cdot (\nabla \times \boldsymbol{v})\end{aligned} \tag{4.27}$$

We obtain,

$$\begin{aligned}\int_\Omega \boldsymbol{W} \cdot [\nabla \times (\frac{1}{\mu}\nabla \times \tilde{\boldsymbol{A}}) - \nabla(\frac{1}{\mu}\nabla \cdot \tilde{\boldsymbol{A}})]d\Omega = \int_\Omega [\frac{1}{\mu}(\nabla \times \tilde{\boldsymbol{A}}) \cdot (\nabla \times \boldsymbol{W}) + \\ \nabla \cdot \{(\frac{1}{\mu}\nabla \times \tilde{\boldsymbol{A}}) \times \boldsymbol{W}\}]d\Omega + \int_\Omega [\nabla \cdot \{(\frac{1}{\mu}\nabla \cdot \tilde{\boldsymbol{A}})\boldsymbol{W})\} - (\frac{1}{\mu}\nabla \cdot \tilde{\boldsymbol{A}})\nabla \cdot \boldsymbol{W}]d\Omega\end{aligned} \tag{4.28}$$

Applying the Divergence theorem on the RHS of the above equation, modifies it into:

$$\begin{aligned}\int_\Omega \boldsymbol{W} \cdot [\nabla \times (\frac{1}{\mu}\nabla \times \tilde{\boldsymbol{A}}) - \nabla(\frac{1}{\mu}\nabla \cdot \tilde{\boldsymbol{A}})]d\Omega = \int_\Omega [\frac{1}{\mu}(\nabla \times \tilde{\boldsymbol{A}}) \cdot (\nabla \times \boldsymbol{W}) + \\ (\frac{1}{\mu}\nabla \cdot \tilde{\boldsymbol{A}})(\nabla \cdot \boldsymbol{W})]d\Omega + \int_\Gamma [\{(\frac{1}{\mu}\nabla \times \tilde{\boldsymbol{A}}) \times \boldsymbol{W}\} \cdot \boldsymbol{n} - (\frac{1}{\mu}\nabla \cdot \tilde{\boldsymbol{A}})(\boldsymbol{W} \cdot \boldsymbol{n})]d\Gamma\end{aligned} \tag{4.29}$$

Using eq(4.29) we rewrite eq(4.25) as:

$$\int_\Omega [\frac{1}{\mu}(\nabla\times\tilde{\boldsymbol{A}})\cdot(\nabla\times\boldsymbol{W})+(\frac{1}{\mu}\nabla\cdot\tilde{\boldsymbol{A}})(\nabla\cdot\boldsymbol{W})]d\Omega+\int_\Gamma[\{(\frac{1}{\mu}\nabla\times\tilde{\boldsymbol{A}})\times\boldsymbol{W}\}\cdot\boldsymbol{n}-$$
$$(\frac{1}{\mu}\nabla\cdot\tilde{\boldsymbol{A}})(\boldsymbol{W}\cdot\boldsymbol{n})]d\Gamma+\int_{\Gamma_H}\boldsymbol{W}\cdot[\frac{1}{\mu}(\nabla\times\tilde{\boldsymbol{A}})\times\boldsymbol{n}-\boldsymbol{K}]d\Gamma+\int_{\Gamma_B}[\frac{1}{\mu}(\nabla\cdot\tilde{\boldsymbol{A}})](\boldsymbol{W}\cdot\boldsymbol{n})d\Gamma \quad (4.30)$$
$$=\int_\Omega \boldsymbol{W}\cdot\boldsymbol{J}\quad d\Omega$$

Evaluating the boundary integrals on disjoint regions Γ_H and Γ_B, and using boundary conditions from equations (4.23), (4.24) and (4.26), and the vector identity $(\boldsymbol{a}\times\boldsymbol{b})\cdot\boldsymbol{c}=\boldsymbol{a}\cdot(\boldsymbol{b}\times\boldsymbol{c})$, we get:

$$\int_\Omega[\frac{1}{\mu}(\nabla\times\tilde{\boldsymbol{A}})\cdot(\nabla\times\boldsymbol{W})+(\frac{1}{\mu}\nabla\cdot\tilde{\boldsymbol{A}})(\nabla\cdot\boldsymbol{W})]d\Omega=\int_\Omega\boldsymbol{W}\cdot\boldsymbol{J}\ \ d\Omega+\int_{\Gamma_H}\boldsymbol{W}\cdot\boldsymbol{K}\ \ d\Gamma \quad (4.31)$$

Ungauged Vector potential

For ungauged vector potential, the weighted residual equation takes the form:

$$\int_\Omega\boldsymbol{W}\cdot[\nabla\times(\frac{1}{\mu}\nabla\times\tilde{\boldsymbol{A}})]d\Omega+\int_{\Gamma_H}\boldsymbol{W}\cdot[\frac{1}{\mu}(\nabla\times\tilde{\boldsymbol{A}})\times\boldsymbol{n}-\boldsymbol{K}]d\Gamma=\int_\Omega\boldsymbol{W}\cdot\boldsymbol{J}\quad d\Omega \quad (4.32)$$

Applying similar mathematical simplifications as for the gauged vector potential, in this case we obtain:

$$\int_\Omega[\frac{1}{\mu}(\nabla\times\tilde{\boldsymbol{A}})\cdot(\nabla\times\boldsymbol{W})\ \ d\Omega=\int_\Omega\boldsymbol{W}\cdot\boldsymbol{J}\ \ d\Omega+\int_{\Gamma_H}\boldsymbol{W}\cdot\boldsymbol{K}\ \ d\Gamma \quad (4.33)$$

4.3.3 Interface between regions with Scalar and Vector potential formulations

In 3D FEM, wherever possible, it is advantageous to use scalar potential rather than the vector potential. However, it is not always possible, even when the current density in the domain is zero. We shall elaborate further on this point in Chapter 6 on transient modeling in 3D. For the time being, we only discuss the weak form for models with mixed potential formulation. Figure 4.1 shows two domains, one of which is formulated using the scalar potential (Ω_ϕ) and the other uses the vector potential (Ω_A). Γ_B ,Γ_H , Γ_D and Γ_N boundaries have their usual meanings. $\Gamma_{\boldsymbol{A},\phi}$ represents the interface boundary between the scalar and the vector potential regions.

For the sake of completeness, we deal with two types of vector potential regions. Initially, we treat the vector potential region as current-free. Later, we describe the mixed formulation with vector potential regions having non-zero current densities by merely extending the weak form from current-free vector potential regions. This is done to limit the number of terms in the equations while deriving the weak form.

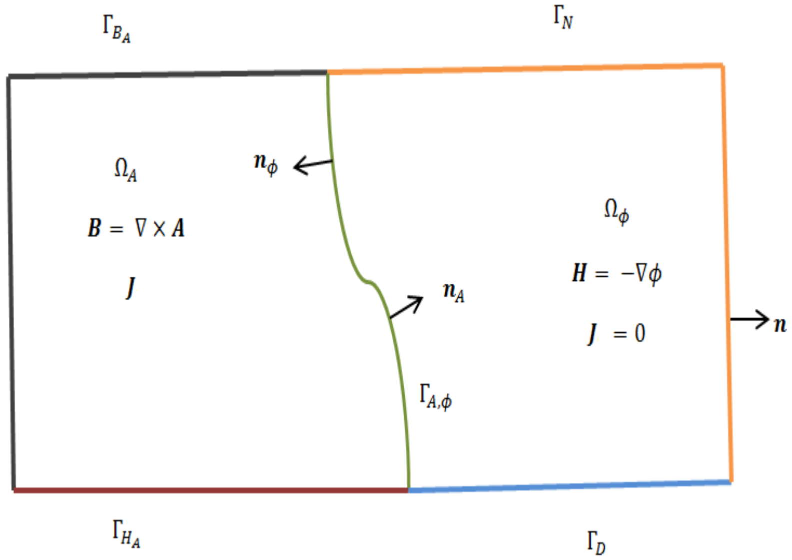

Figure 4.1: A representation for mixed potential formulation

Vector potential region with J = 0

For better readability purposes, we rewrite all the necessary PDEs and corresponding boundary conditions associated with the mixed formulation here.

$$\begin{aligned}
\nabla \times (\frac{1}{\mu}\nabla \times \boldsymbol{A}) = 0 &\qquad \text{in} \quad \Omega_A \\
\nabla.(\mu\nabla\phi) = 0 &\qquad \text{in} \quad \Omega_\phi \\
(\frac{1}{\mu}\nabla \times \boldsymbol{A}) \times \boldsymbol{n} = \boldsymbol{K} &\qquad \text{on} \quad \Gamma_{H_A} \\
\boldsymbol{A} \cdot \boldsymbol{n} = 0 &\qquad \text{on} \quad \Gamma_{H_A} \\
\boldsymbol{n} \times \boldsymbol{A} = \alpha &\qquad \text{on} \quad \Gamma_{B_A} \\
\frac{1}{\mu}\nabla \cdot \boldsymbol{A} = 0 &\qquad \text{on} \quad \Gamma_{B_A} \\
\phi = \phi_0 &\qquad \text{on} \quad \Gamma_D \\
(\mu\nabla\phi) \cdot \boldsymbol{n} = b &\qquad \text{on} \quad \Gamma_N \\
(\frac{1}{\mu}\nabla \times \boldsymbol{A}) \times \boldsymbol{n}_A - \nabla\phi \times \boldsymbol{n}_\phi = 0 &\qquad \text{on} \quad \Gamma_{A,\phi} \\
(\nabla \times \boldsymbol{A}) \cdot \boldsymbol{n}_A - \mu\nabla\phi \cdot \boldsymbol{n}_\phi = 0 &\qquad \text{on} \quad \Gamma_{A,\phi}
\end{aligned} \tag{4.34}$$

Also, in this section we shall assume the gauged vector formulation, which imposes the following additional boundary condition:

$$\boldsymbol{A} \cdot \boldsymbol{n}_A = 0 \qquad \text{on} \quad \Gamma_{A,\phi} \tag{4.35}$$

As different governing PDEs apply to the different domains, therefore, the weak formulation for the scalar and the vector potential regions will also be different.

We begin with the applying the method of weighted residual to the vector potential region first, as given by:

$$\begin{aligned}\int_{\Omega_A} \boldsymbol{W}\cdot[\nabla\times(\frac{1}{\mu}\nabla\times\tilde{\boldsymbol{A}})-\nabla(\frac{1}{\mu}\nabla\cdot\tilde{\boldsymbol{A}})]d\Omega+\int_{\Gamma_{H_A}}\boldsymbol{W}\cdot[\frac{1}{\mu}(\nabla\times\tilde{\boldsymbol{A}})\times\boldsymbol{n}-\boldsymbol{K}]d\Gamma\\ +\int_{\Gamma_{B_A}}[\frac{1}{\mu}(\nabla\cdot\tilde{\boldsymbol{A}})](\boldsymbol{W}\cdot\boldsymbol{n})d\Gamma++\int_{\Gamma_{A,\phi}}\boldsymbol{W}\cdot[\frac{1}{\mu}(\nabla\times\tilde{\boldsymbol{A}})\times\boldsymbol{n}_A-\nabla\tilde{\phi}\times\boldsymbol{n}_\phi]d\Gamma=0\end{aligned} \tag{4.36}$$

The first three terms on the LHS of the above equation are same as that of the (4.25). Therefore, we can rewrite (4.36), using the same mathematical simplification as applied in Section 4-3-2 as below:

$$\begin{aligned}\int_{\Omega_A}[\frac{1}{\mu}(\nabla\times\tilde{\boldsymbol{A}})\cdot(\nabla\times\boldsymbol{W})+(\frac{1}{\mu}\nabla\cdot\tilde{\boldsymbol{A}})(\nabla\cdot\boldsymbol{W})]d\Omega-\int_{\Gamma}\boldsymbol{W}\cdot[\frac{1}{\mu}(\nabla\times\tilde{\boldsymbol{A}})\times\boldsymbol{n}]d\Gamma\\ -\int_{\Gamma}(\frac{1}{\mu}\nabla\cdot\tilde{\boldsymbol{A}})(\boldsymbol{W}\cdot\boldsymbol{n})]d\Gamma+\int_{\Gamma_{H_A}}\boldsymbol{W}\cdot[\frac{1}{\mu}(\nabla\times\tilde{\boldsymbol{A}})\times\boldsymbol{n}-\boldsymbol{K}]d\Gamma+\\ \int_{\Gamma_{B_A}}\frac{1}{\mu}(\nabla\cdot\tilde{\boldsymbol{A}})(\boldsymbol{W}\cdot\boldsymbol{n})d\Gamma+\int_{\Gamma_{A,\phi}}\boldsymbol{W}\cdot[\frac{1}{\mu}(\nabla\times\tilde{\boldsymbol{A}})\times\boldsymbol{n}_A-\nabla\tilde{\phi}\times\boldsymbol{n}_\phi]d\Gamma=0\end{aligned} \tag{4.37}$$

In this equation, the second and the third surface integrals are to be evaluated over the enclosing boundary $\Gamma=\Gamma_{H_A}\cup\Gamma_{B_A}\cup\Gamma_{A,\phi}$. Thus, it further simplifies into:

$$\begin{aligned}\int_{\Omega_A}[\frac{1}{\mu}(\nabla\times\tilde{\boldsymbol{A}})\cdot(\nabla\times\boldsymbol{W})+(\frac{1}{\mu}\nabla\cdot\tilde{\boldsymbol{A}})(\nabla.\boldsymbol{W})]d\Omega-\int_{\Gamma_{B_A}}\boldsymbol{W}\cdot[\frac{1}{\mu}(\nabla\times\tilde{\boldsymbol{A}})\times\boldsymbol{n}]d\Gamma\\ -\int_{\Gamma_{H_A}\cup\Gamma_{A,\phi}}(\frac{1}{\mu}\nabla\cdot\tilde{\boldsymbol{A}})(\boldsymbol{W}\cdot\boldsymbol{n})]d\Gamma-\int_{\Gamma_{H_A}}\boldsymbol{W}\cdot\boldsymbol{K}d\Gamma+-\int_{\Gamma_{A,\phi}}\boldsymbol{W}\cdot(\nabla\tilde{\phi}\times\boldsymbol{n}_\phi)d\Gamma=0\end{aligned} \tag{4.38}$$

Boundary conditions as applied to the weighting function $\boldsymbol{W}$, similar to (4.26) are applicable in this instance also. This eliminates the second and the third integrals from the above equation, and results into:

$$\int_{\Omega_A}[\frac{1}{\mu}(\nabla\times\tilde{\boldsymbol{A}})\cdot(\nabla\times\boldsymbol{W})+(\frac{1}{\mu}\nabla\cdot\tilde{\boldsymbol{A}})(\nabla\cdot\boldsymbol{W})]d\Omega-\int_{\Gamma_{A,\phi}}\boldsymbol{W}\cdot(\nabla\tilde{\phi}\times\boldsymbol{n}_\phi)d\Gamma=\int_{\Gamma_{H_A}}\boldsymbol{W}\cdot\boldsymbol{K}d\Gamma \tag{4.39}$$

The surface integral on the LHS of the above equation is evaluated on the interface (surface) between the scalar and the vector potential regions. Let C be the curve enclosing the interface boundary $\Gamma_{A,\phi}$. On the curve C, in general, either the normal or the tangential component of the magnetic field is defined. In the light of this information, we attempt to simplify the above equation further, as follows:

$$-\int_{\Gamma_{A,\phi}}\boldsymbol{W}\cdot(\nabla\tilde{\phi}\times\boldsymbol{n}_\phi)d\Gamma=-\int_{\Gamma_{A,\phi}}\boldsymbol{n}_\phi\cdot(\boldsymbol{W}\times\nabla\tilde{\phi})d\Gamma \tag{4.40}$$

Now, substituting $\boldsymbol{n}_\phi=-\boldsymbol{n}_A$, and using the identity: $\nabla\times(\lambda\boldsymbol{F})=\lambda\nabla\times\boldsymbol{F}-\boldsymbol{F}\times\nabla\lambda$. We obtain:

$$-\int_{\Gamma_{A,\phi}}\boldsymbol{n}_\phi\cdot(\boldsymbol{W}\times\nabla\tilde{\phi})d\Gamma=\int_{\Gamma_{A,\phi}}\boldsymbol{n}_A\cdot[\tilde{\phi}(\nabla\times\boldsymbol{W})-\nabla\times(\tilde{\phi}\boldsymbol{W})]d\Gamma \tag{4.41}$$

The second integral can be replaced with a line integral using the Stokes' theorem.

$$-\int_{\Gamma_{A,\phi}} \boldsymbol{n}_\phi \cdot (\boldsymbol{W} \times \nabla\tilde{\phi}) d\Gamma = \int_{\Gamma_{A,\phi}} \boldsymbol{n}_A \cdot [\tilde{\phi}(\nabla \times \boldsymbol{W})] d\Gamma - \int_C \tilde{\phi}\boldsymbol{W} \cdot dl \tag{4.42}$$

For the sake of generality, we assume the curve C to be composed of two disjoint curves, C_B and C_H. Let the tangential component of the field be defined on C_H, which implies the curve C_H is an equipotential curve. Also, assume the normal component of the field is defined on C_B, which implies then, $\boldsymbol{W} \cdot dl = 0$, on C_B. Equation (4.42), can be rewritten as:

$$-\int_{\Gamma_{A,\phi}} \boldsymbol{n}_\phi \cdot (\boldsymbol{W} \times \nabla\tilde{\phi}) d\Gamma = \int_{\Gamma_{A,\phi}} \boldsymbol{n}_A \cdot [\tilde{\phi}(\nabla \times \boldsymbol{W})] d\Gamma - \int_{C_H} \phi_0 \boldsymbol{W} \cdot dl \tag{4.43}$$

Using this information, we can modify (4.39) into:

$$\begin{aligned} \int_{\Omega_A} [\frac{1}{\mu}(\nabla \times \tilde{\boldsymbol{A}}) \cdot (\nabla \times \boldsymbol{W}) + (\frac{1}{\mu}\nabla \cdot \tilde{\boldsymbol{A}})(\nabla . \boldsymbol{W})] d\Omega - \int_{\Gamma_{A,\phi}} [\tilde{\phi}(\nabla \times \boldsymbol{W})] \cdot \boldsymbol{n}_A d\Gamma \\ = \int_{\Gamma_{H_A}} \boldsymbol{W} \cdot \boldsymbol{K} d\Gamma + \int_{C_H} \phi_0 \boldsymbol{W} \cdot dl \end{aligned} \tag{4.44}$$

This represents the weak form the vector potential region in the mixed formulation. Similarly, we must arrive at the weak form for the scalar potential domain as well. This is done below. As usual, we begin by writing the weighted residual form which follows from (4.34). That is:

$$\int_{\Omega_\phi} V(\nabla \cdot \mu\nabla\tilde{\phi}) d\Omega + \int_{\Gamma_N} V(b - \mu\nabla\tilde{\phi} \cdot \boldsymbol{n}) d\Gamma + \int_{\Gamma_{A,\phi}} V[(\nabla \times \tilde{\boldsymbol{A}}) \cdot \boldsymbol{n}_A - \mu\nabla\tilde{\phi} \cdot \boldsymbol{n}_\phi] d\Gamma = 0 \tag{4.45}$$

where, V is the scalar weighting function.

Using (4.11), we write the above equation as:

$$\begin{aligned} -\int_{\Omega_\phi} \mu(\nabla\phi \cdot \nabla V) d\Omega + \int_\Gamma V(\mu\nabla\tilde{\phi} \cdot \mathbf{n}) d\Gamma + \int_{\Gamma_N} V(b - \mu\nabla\tilde{\phi} \cdot \boldsymbol{n}) d\Gamma \\ + \int_{\Gamma_{A,\phi}} V[(\nabla \times \tilde{\boldsymbol{A}}) . \boldsymbol{n}_A - \mu\nabla\tilde{\phi} \cdot \boldsymbol{n}_\phi] d\Gamma = 0 \end{aligned} \tag{4.46}$$

Here, the second integral is evaluated over the boundary $\Gamma = \Gamma_{A,\phi} \cup \Gamma_N \cup \Gamma_D$. This simplifies the above equation into:

$$\begin{aligned} -\int_{\Omega_\phi} \mu(\nabla\phi . \nabla V) d\Omega + \int_{\Gamma_D} V(\mu\nabla\tilde{\phi} \cdot \mathbf{n}) d\Gamma + \int_{\Gamma_N} Vb \ \ d\Gamma \\ + \int_{\Gamma_{A,\phi}} V(\nabla \times \tilde{\boldsymbol{A}}) \cdot \boldsymbol{n}_A \ \ d\Gamma = 0 \end{aligned} \tag{4.47}$$

Since, Γ_D represents the Dirichlet boundary, thus $V = 0$ on Γ_D. Therefore,

$$-\int_{\Omega_\phi} \mu(\nabla\phi \cdot \nabla V) d\Omega + \int_{\Gamma_{A,\phi}} V(\nabla \times \tilde{\boldsymbol{A}}) \cdot \boldsymbol{n}_A \ \ d\Gamma = -\int_{\Gamma_N} Vb \ \ d\Gamma \tag{4.48}$$

This represents the weak form for the scalar domains in the mixed formulation problem.

Vector potential region with $\boldsymbol{J_0} \neq \mathbf{0}$

In the last derivation for the weak form, we assumed the vector potential region to be current-free. However, in general, it may not be the case. Therefore, the weak form for the vector domains need to be modified. We shall not go through the entire derivation again. Rather, based on the knowledge from the previous sections, we shall include an additional term in equation (4.44) to incorporate the non-zero current densities. This is shown below:

$$\begin{aligned}\int_{\Omega_A}[\frac{1}{\mu}(\nabla\times\tilde{\boldsymbol{A}})\cdot(\nabla\times\boldsymbol{W})+(\frac{1}{\mu}\nabla\cdot\tilde{\boldsymbol{A}})(\nabla.\boldsymbol{W})]d\Omega-\int_{\Gamma_{A,\phi}}[\tilde{\phi}(\nabla\times\boldsymbol{W})]\cdot\boldsymbol{n}_A d\Gamma \\ =\int_{\Gamma_{H_A}}\boldsymbol{W}\cdot\boldsymbol{K}d\Gamma+\int_{C_H}\phi_0\boldsymbol{W}\cdot dl+\int_{\Omega_A}\boldsymbol{W}\cdot\boldsymbol{J}\ d\Omega\end{aligned} \tag{4.49}$$

The weak form for the scalar region remains as it is.

4.4 Meshing

The next step after arriving at the weak form of the original PDE, is the discretization of the problem space or *meshing*. First and foremost, an analyst must be concerned with an accurate discretization of the domain Ω of interest. Meshing involves dividing the domain into a finite number of non-overlapping elements. It must be ensured that the element edges and/or faces coincide with the external boundaries and/or boundaries between domains with different properties, to minimize the *domain discretization error*. A good quality mesh is a prerequisite to a convergent and a fairly accurate solution. The quality of the mesh is dependent on several factors. Some general considerations are: the aspect ratios need to be closer to unity, vertex angles in case of triangular elements should be roughly 60 degrees, elements should not be overly distorted, etc. These considerations are not hard rules and can be overlooked, if need be. All these aspects in conjunction with limitation of the computational resource and time cost, often present conflicting requirements on the mesh generation. As such, generation of mesh has been and remains an active area of research[34].

4.4.1 Finite elements in 3D

In 3D, the default element shape used is the tetrahedral element. The tetrahedron is the 3D *simplex* element, implying that any 3D geometry regardless of the shape can be meshed with the tetrahedron. A mesh comprising entirely of tetrahedral elements is usually taken care of by default meshing algorithms without much input from the user. As we shall see though, it is not always the preferred element shape. Other existing element shapes which are commonly employed are the *hexahedron*, the *prism* and the *pyramids*. These elements, however, cannot be used to mesh every 3D geometry.

The primary reason in opting for a hexahedron or a prism element over a tetrahedron is that they can significantly reduce the number of elements in the mesh. These elements can have high aspect ratios, unlike tetrahedron which usually have an aspect ratio close to unity for better results. Therefore, these elements are often a better choice if the solution is not expected to vary abruptly along a particular axis (or axes), compared to other axis (or axes).

Less number of elements also, in general, implies fewer unknown degrees of freedom. Figure 4.2 below shows a 10-node tetrahedral element, a 20-node hexahedron element and a 27-node hexahedron element. However, as one can see from the figure there are different number of nodes per element depending upon the shape of the element and its order. Thus, it is not quite straightforward to establish a direct relationship between number of elements and the number of degrees of freedom. More number of nodes per element also implies larger element matrices and a denser corresponding system matrix [36].

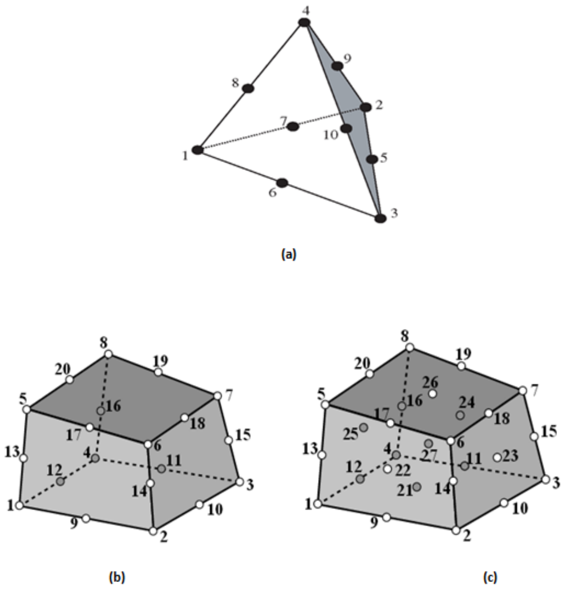

Figure 4.2: 3D element shapes: (a) 10 node tetrahedron (b) 20 node hexahedron (c) 27 node hexahedron

It is debatable which among the tetrahedral or hexahedral (or prism) elements, is the "best" one. However, a position taken often is that the hexahedral elements perform better than the tetrahedral ones for similar number of degrees of freedom. Nonetheless, this cannot be generalized to every problem, and a decision to opt for a particular element type is often best left to the analyst [34].

4.4.2 Types of Mesh

Meshes are typically classified into two classes: the structured mesh and the unstructured mesh. In most cases though, a combination of both is used for better efficiency. [34]

Structured Mesh

A structured mesh usually consists of quadrilateral or hexahedral elements. The mesh structure then resembles that of a rectangular grid where the edges intersect almost orthogonally. The edges of the elements can be curved as well, and usually are, to account for external curved boundaries of the material. A consequence of the structured mesh is that the number of adjacent elements in the interior elements (or nodes) of the mesh is the same. In other words, only a given number of elements meet at any interior node of the mesh. This type of meshing exclusively, however, is not always possible. Many geometries encountered are too complex to be meshed using the structured mesh. Electrical machines being a case in point. Nonetheless, structured mesh should be preferred wherever possible, for their accuracy and limited number of degrees of freedom [34]. An example of structured mesh is shown in Figure 4.3.

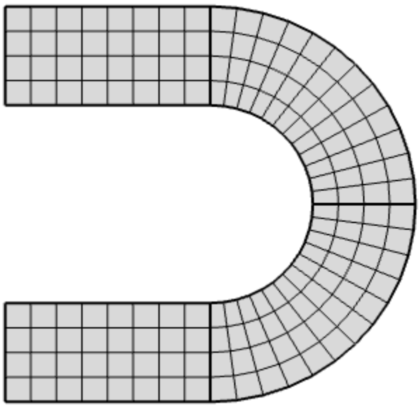

Figure 4.3: An example of structured mesh.

Unstructured Mesh

Unlike, the structured mesh, in an unstructured mesh any number of elements may meet at a given interior node of the mesh. Common shapes of elements in 2D and 3D are the triangular and the tetrahedral respectively. Although, it is still possible to have quadrilateral elements in an unstructured mesh. Unstructured mesh is suitable for any general shape of the domains making it very likely to be implemented exclusively, without the need for resorting to the structured mesh in any part of the model. An example of the unstructured mesh is depicted in Figure 4.4.

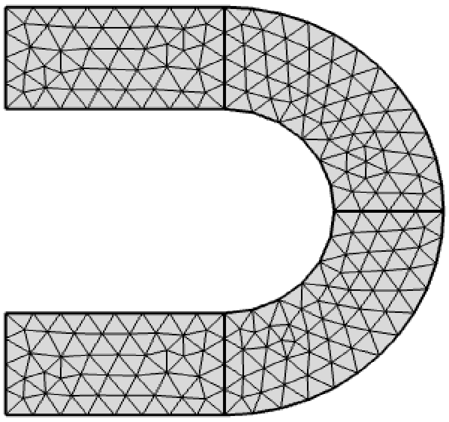

Figure 4.4: An example of unstructured mesh.

Different algorithms exist for generating the structured as well as the unstructured meshes. As mentioned earlier, an optimal mesh can often be a mixed one. In the context of this work, we discuss only one such possibility here, known as Sweeping.

Mapped mesh —Sweeping

It is often the case that opposite edges or faces of the surface or volume to be meshed are similar topologically. Under such circumstances, opposite ends tend to be meshed in a manner such that they consists of equal number of divisions. And hence, the extension of the mesh in the interior of the domain can be a relatively easy proposition. Such meshes are also known as *mapped mesh.*

Sweeping is one such class of the mapped mesh. Sweeping scheme usually implies a structured (hexahedral) or even an unstructured (triangular) mesh is swept through space along a predefined curve or an edge of the domain to be meshed, as the case might be. Figure 4.5 illustrates the sweeping mesh scheme.

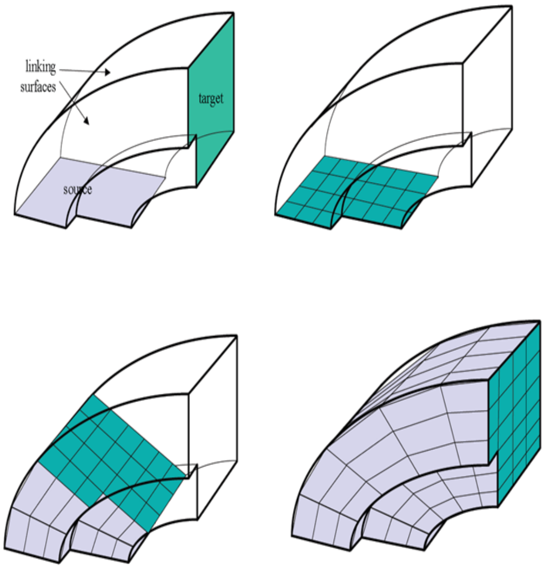

Figure 4.5: Sweep mesh scheme. Pictures taken from [37]

4.5 Nodal and Edge elements

In the finite element analysis, the scalar potentials are approximated using the *nodal elements* or *node-based expansion functions.* Each node has its corresponding expansion function. These nodal expansion functions, denoted by N_i, satisfy the following relations:

$$\begin{aligned} N_i &= 1, \qquad \text{at the node} \quad i \\ N_i &= 0, \qquad \text{at other nodes} \end{aligned} \tag{4.50}$$

Using this definition, the scalar potential, for instance, ϕ can be approximated as:

$$\phi \simeq \sum_{i=1}^{n} N_i \phi_i \tag{4.51}$$

where, n is the number of nodes.
Clearly, at the node i i.e. at (x_i, y_i), $N_i(x, y) = 1$. At the other nodes of the element, to which the node i belongs, $N_i(x, y) = 0$, and at any other coordinates (x, y), the magnitude of $N_i(x, y)$ is determined by its distance from the node i. It is quite straightforward to extend the same definition to three dimensions.
Usually, polynomials are preferred as the expansion functions. For instance, a 2D first-order nodal function can be defined as follows:

$$N_i(x, y) = a_i x + b_i y + c_i \tag{4.52}$$

where, a_i, b_i and c_i are the coefficients derived based on the equation (4.50).
Approximation of potentials or any dependent variable for that matter using higher order elements is also quite popular. For further details pertaining to higher order elements, readers may refer to [29, 30, 34].
The interpolation functions described here can also be used as the weighting function. This forms the basis for the Galerkin method, mentioned earlier in Section 4.2.
Approximating vector potentials is a little more complicated exercise. Intuitively, one might be inclined to think that using three individual expansion functions, one for each component, should work reasonably well. In fact, in the beginning, gauged vector potentials were interpolated using the nodal elements. However, some of the obstacles encountered with that approach were:

1. It is difficult to ensure the tangential continuity of electrical and magnetic fields across material interfaces in the absence of surface currents. Node-by-node enforcement of continuity, in such cases, does not guarantee the continuity over the edges or the faces confined by the nodes.

2. The numerical issues arising out of such discontinuities are especially more problematic in presence of corners or wedges.

3. In case of the ungauged vector potential, the lack of enforcement of the divergence condition usually leads to a system of algebraic equations for which iterative methods of solution usually fail.

These issues were overcome by the use of edge elements [30].
Edge elements or edge-shaped functions are also known as *vector-shape functions.* As the name suggests, the expansion function corresponds to an edge rather than a node. Also unlike nodal elements, edge elements have a direction associated with them. Therefore, they present a more natural way of representing vector functions. The direction and the magnitude of the vector potential at any point inside an element depends on its distance from the edges of the element, Closer the edge is to the point more its weight in the magnitude and direction of the vector potential at that particular point [38]. The edge-shaped functions, denoted by

$\boldsymbol{N}_i$, satisfy the following criteria:

$$\begin{aligned} \int_l \boldsymbol{N}_i.d\boldsymbol{l} &= 1, \qquad \text{along the edge} \quad i \\ \int_l \boldsymbol{N}_i.d\boldsymbol{l} &= 0, \qquad \text{along all other edges} \end{aligned} \tag{4.53}$$

where, l is the length of the edge.
Consequently, a vector potential, for instance, $\boldsymbol{A}$ is approximated as:

$$\boldsymbol{A} \simeq \sum_{i=1}^{m} \boldsymbol{N}_i A_i \tag{4.54}$$

where, m is the number of edges.
In other words, the expansion function $\boldsymbol{N}_i$ has a tangential component only along the edge i, whereas normal components exist along other edges. This also means that edge-shaped functions can be easily used to satisfy the continuity requirements for the tangential components of vector fields. Finally, edge elements also ensure that the divergence condition is automatically satisfied. Similar, to nodal elements, higher order edge elements also exist. Reference [30] gives further details.
Using the definitions for the aforementioned nodal and/or edge elements, the weak form can be evaluated on each element. This results in a local algebraic system of equations for each element. Subsequently, these system of equations are assembled into a global system of equations, with unknowns corresponding to each node or edge. The final step in the finite element approximation is to solve this resulting system of equations. This is discussed next.

4.6 Solving system of Linear equations

Solving partial differential equations using the finite element analysis finally boils down to solving a system of linear equations. The unknowns in such equations are the degrees of freedom in the finite element approximation [35]. The steady state linear equations obtained from the finite element analysis are generally of the following form:

$$K\hat{\boldsymbol{x}} = \boldsymbol{f} \tag{4.55}$$

where, K is a square matrix with known coefficients, $\hat{\boldsymbol{x}}$ is the unknown vector representing the nodal or edge unknowns, and $\boldsymbol{f}$ is a known vector, called as the forcing or the source vector.

Solution of the unknown $\hat{\boldsymbol{x}}$ vector in (4.55) can be arrived at either by the direct methods or the iterative methods.

Direct methods are the variants of the commonly employed Gauss elimination methods. For most 2D and some 3D problems with relatively fewer degrees of freedom, they are usually well suited. Direct methods are robust and give predictable results for non-singular K matrices, as they rely on factorization of the matrix into lower and upper triangular matrices. Also, they are relatively easy to understand compared to the iterative methods. Direct methods, however, exhibit a poor performance as the matrix size increases. For large scale problems, these methods are inefficient and rather avoidable as they require large amounts of memory

and are also expensive in terms of computational time cost [34]. In this thesis as we are concerned with the 3D problems with the number of degrees of freedom running into several millions, henceforth, we shall mostly limit our discussion to the iterative methods.
To have a rather general idea of the correlation between the physical memory (RAM) required to solve a system of linear equations by a typical direct solver or the iterative solvers, and the number of degrees of freedom—arising in typical finite element problems, see [39].

4.7 Iterative methods

Iterative methods employ a smarter way of arriving at the final solution. Typically, they add a stepwise correction to a known initial guess, which finally converges to the correct solution [29]. The memory requirement and time cost in case of large scale problems are significantly lower compared to the direct methods. Therefore, iterative methods are best suited for 3D problems such as the one undertaken in this thesis. Over the past few years, many robust and efficient iterative algorithms have been developed, making them even more attractive for end users.
The iterative procedure is terminated as soon as one of the following conditions is met [34]:

- A predetermined number of iterations have been completed; or
- The relative error is less than the predefined tolerance limit.

Two of the iterative methods employed in this thesis are: the *Conjugate Gradients* method and the *Generalized Minimum Residual* method. A brief account of both is given below:

Conjugate Gradients method

Conjugate gradient method (CG) is essentially an advanced version of the Steepest gradient method. The Steepest gradient method basically attempts at minimizing the quadratic form $F(z)$ defined by:

$$F(\boldsymbol{z}) = \boldsymbol{z}^T K \boldsymbol{z} - 2\boldsymbol{z}^T \boldsymbol{f} \tag{4.56}$$

If the matrix K is symmetric positive definite then at the minimum of $F(\boldsymbol{z})$, $\boldsymbol{z}$ coincides with the true solution $\hat{\boldsymbol{x}}$ in (4.55). The underlying idea is to update a correction in $\hat{\boldsymbol{z}}^k$ at every iterative step such that $\delta \boldsymbol{z}^k$ is orthogonal to the locus of constant $F(z)$. Therefore, the solution proceeds in the direction of the steepest descent, given by the negative gradient $-\nabla F(\boldsymbol{z})$ [41].

$$-\nabla F(\boldsymbol{z}) = \boldsymbol{f} - K\hat{\boldsymbol{z}} = \boldsymbol{r} \tag{4.57}$$

where, $\boldsymbol{r}$ is called the residual.
Conjugate gradients method improves upon the steepest descent method by ensuring that the successive residuals are orthogonal to each other. In this way, it ensures that the error eliminated at a step of iteration is prevented from reoccurring at any subsequent iteration [29].

CG methods are particularly impressive whenever the matrix K is symmetric and positive definite. The performance in case of non-symmetric or indefinite matrices can range from being poor to no convergence at all. Thus, it is a good idea to ensure that K is symmetric and positive definite before applying the method to a large system of equations.

Generalized Minimum Residual method

The Generalized Minimum Residual method (GMRES) is applicable in general, to all matrices. It is based on the minimization of the residual:

$$\boldsymbol{r}^k = \boldsymbol{f} - K\hat{\boldsymbol{x}}^k \tag{4.58}$$

The next iterate of the solution is derived from the information of two subspaces, namely the expansion space, M^s and the projection space, N^s. The idea is to approximate the next solution step from the previous value, such that $\hat{\boldsymbol{x}}^k \in \hat{\boldsymbol{x}}^0 + M^s$ and $(\boldsymbol{f} - K\hat{\boldsymbol{x}}^k) \perp N^s$. Different algorithms exist for generation of these subspaces, see [35, 40, 41].
A major limitation of the *unlimited* GMRES method is that the k^{th} iteration requires all previously computed vectors to be saved in memory, and an equivalent number of increased algebraic operations. A pragmatic way to implement the GMRES is by using its *restarted* version. In the restarted GMRES, the k^{th} iterate is used as an initial guess and a new GMRES sequence is started from there [41]. Even after implementing the restarted version, the CPU time and the memory requirement is not always low. For symmetric positive definite systems, it is almost always outperformed by the CG method. However, effective pre-conditioning can significantly curtail the number of required iterations and save on the computational time cost and resource. One such preconditioning is by the use of *Multigrid* methods [35].

Illustrative example

We illustrate the advantages of the iterative methods over the direct methods by virtue of the following example.
Consider a small scale 3D model of the BDFIM presented in Chapter 2, as shown in Figure 2-4. The axial length of the machine in this case is only 20mm, which is only $1/12^{th}$ of the actual length of the machine. The model presents a simple magnetostatic case and has 2.8 million degrees of freedom, if formulated entirely using vector potential. The system of equations were solved using the direct solver, the CG method and the GMRES method. Plots for the field lines are shown in Figure 4.6. Simulations were performed on Intel 3.5 GHz processor with 32 GB RAM. Performance of the solvers is listed in Table 4-1.

Solver Used	Memory Usage	Time Cost
Direct	30.18 GB	12 mins 49 s
GMG/GMRES (50)	7.69 GB	13 mins 58 s
GMG/CG	6.89 GB	11 mins 44s

Table 4-1: Solver performance comparison

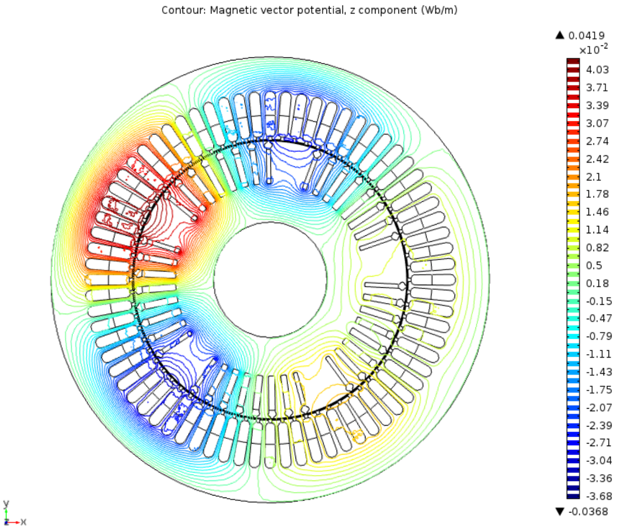

Figure 4.6: Magnetic field lines from a cross-section in a 3D model of the BDFIM geometry.

Clearly, the advantages of the iterative methods are evident as the direct solver requires far much memory. Also, in terms of computation time, iterative methods perform well. As the number of unknowns increase, direct solvers eventually fail due to limitations in memory and also time cost goes up significantly as the number of operations required for factorization increase. In the same example, if we extend the system further to 3.2 million degrees of freedom, direct solver fails to solve the system of equations on account of limited memory. On the other hand, iterative solvers, in particular CG, continue to impress. From this example, one might conclude that the saving in terms of memory is not substantial if one is to choose between the CG and GMRES solver. However, this is not always true. Typically, the saving in memory increases with the number of unknowns. This argument shall become more evident in the next chapter.

Figures 4.7 and 4.8 show typical convergence plots for the GMRES and the CG solver respectively.

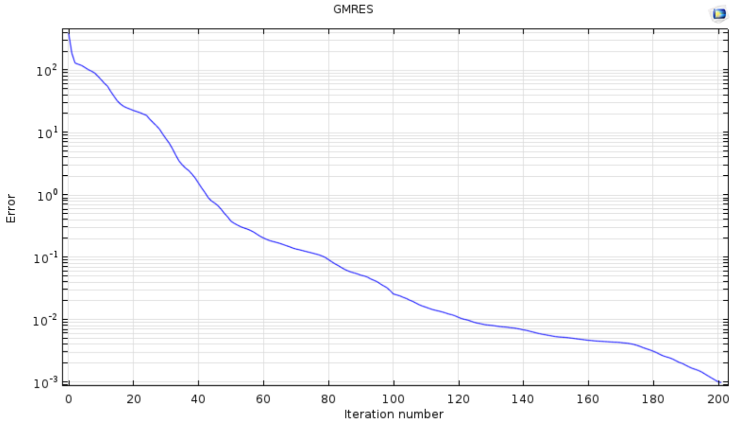

Figure 4.7: Convergence plot for the GMRES solver

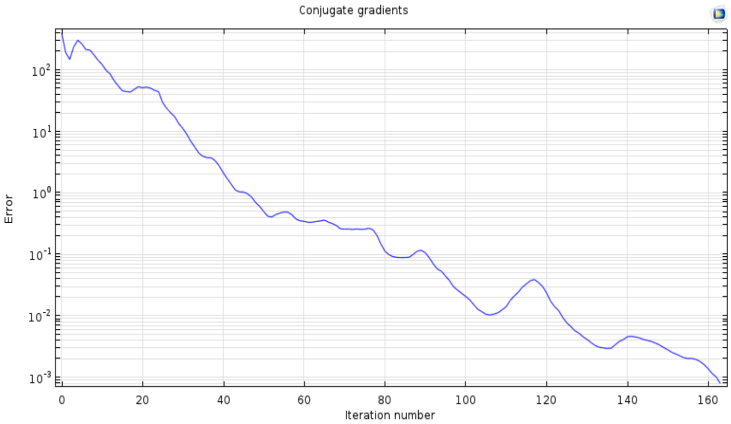

Figure 4.8: Convergence plot for the CG solver

4.7.1 Pre-conditioning

Often before implementing the iterative methods such as CG and GMRES, pre-conditioning of the matrices is done to enhance their convergence for the iterative solution process. This basically involves the pre-multiplication of the matrix K with a suitable pre-conditioner matrix which improves the spectral properties of the new matrix and hence, leads to the better rate of convergence. As one might expect, the extra effort in constructing an effective pre-conditioner and its subsequent multiplication with K, should be justified eventually, in the pursuit of a faster convergence [34]. A pre-conditioner matrix M^{-1} is essentially an approximation to the inverse of matrix K. In the light of this argument, the system of equations in (4.55) is modified into:

$$M^{-1}K\hat{\boldsymbol{x}} = M^{-1}\boldsymbol{f} \tag{4.59}$$

Requiring M^{-1} to be a good approximation to the inverse of K and simultaneously being computationally less intensive to construct clearly implies a trade-off. Some of the most commonly used pre-conditioners are the Jacobi, the symmetric Gauss-Seidel, the incomplete LU factorization and the incomplete Cholesky pre-conditioners [35]. Without an effective pre-conditioner, an iterative solver may even fail to converge at all.

Multigrid methods

The aforementioned pre-conditioners are not so effective when dealing with very large matrices. Electromagnetic boundary value problems in 3D discretized by finite elements often give rise to such large systems. Large size matrices may arise due to the fine geometrical features such as small airgaps in electrical machines or thin conducting plates, among many other similar features which require fine discretization. Multigrid methods were developed precisely to deal with such huge matrices. The objective was to formulate an iterative methods whose convergence was somewhat independent of the grid size [35].

An intrinsic limitation of the iterative methods is that even though the high frequency error modes are eliminated efficiently, the low frequency modes or the smooth error components tend to stay. This often leads to stalling in the convergence process. The low frequency error modes appear as more oscillatory on a coarser mesh, and vice-versa. Multigrid methods eliminate both low and high frequency errors by performing iterative procedures on coarse and finer grids [42–44].

In the present work, multigrid pre-conditioners have been almost invariably employed for the iterative procedures, unless mentioned otherwise. In fact the numbers given in the previous section pertain to the Geometric multigrid pre-conditioning. The same problem when solved with the SOR preconditioner for CG takes approximately 58 mins with a required physical memory of 7.98 GB.

4.7.2 Ill-conditioning

A prerequisite that is often mentioned for a system of equations to be solved by an iterative process is that the K matrix should not be *ill-conditioned*. A problem is said to be ill-conditioned when a small change in the input parameters results in a relatively large change in the output solution. Ill-conditioned problems tend to have a high condition number of the K matrix. Roughly the condition number is equal to the magnitude of the ratio of the largest eigenvalue of a matrix to its smallest[1]. The convergence of the iterative methods depend critically on the condition number of the matrix. A high condition number can result in stalled convergence or no convergence at all [35]. Also, on some occasions, a poor choice of the pre-conditioners can result in a so-called *ill-conditioned pre-conditioner*. Therefore, one has to be mindful of the choice for the pre-conditioner.

Well-conditioned problems might also at times result in the ill-conditioned equations; this might be due to a correct but very fine mesh idealization. Such problems can be done away with a coarser mesh. On the other hand, ill-conditioned problems can also be attributed to—among other factors—sudden mesh variation and high aspect ratio of the elements [34]. Limiting the growth factor in the mesh can be done to avoid abrupt change in element sizes. However, this problem is prominent only if the problem has relatively less number of degrees of freedom. Elements with high aspect ratio are often encountered in 3D problems. Very sharp corners or edges in the discretized domain are also potential points of singularities, and smoothening or filleting away such corners and edges can boost the convergence significantly [45].

4.8 2D multi-slice model

In the 3D magnetostatic analysis of the BDFIM in this thesis, we shall mostly limit our analysis to compare the results between the skewed and the non-skewed rotor. The effects of skew in the BDFIM rotor has been studied earlier using the 2D multi-slice model [8]. In Chapter 5, we shall frequently refer to this model in order to establish the effects of the axial component of the magnetic flux. Therefore, it seems appropriate to give the reader a brief idea about the multi-slice model.

Multi-slice models were developed to estimate the effects of skew on machine performance, in case of a skewed rotor. In this model, several normal 2D models, say m slices, are used to approximate a skewed rotor. Each slice is assumed to be $1/m^{th}$ of the total machine length.

---

[1] This definition actually holds true only for symmetric positive definite matrices.

In Figure 4.9 the conductors have been skewed by an angle α.

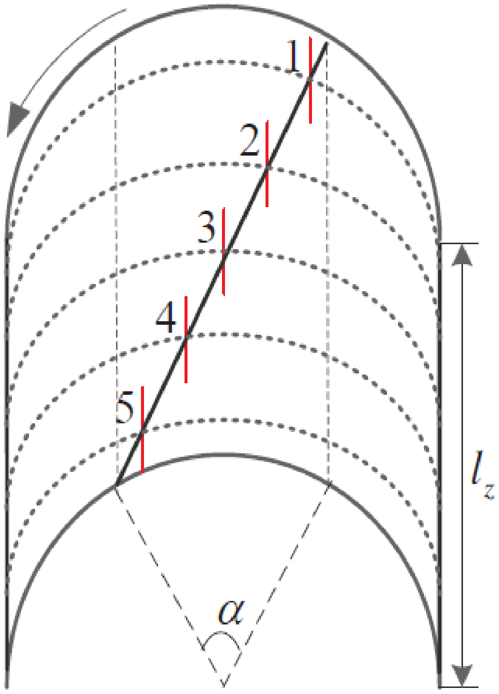

Figure 4.9: A multi-slice model, figure reproduced from [8] .

The field equation applicable for the model is:

$$\frac{\partial}{\partial x}(\frac{1}{\mu}\frac{\partial A_z^n}{\partial x}) + \frac{\partial}{\partial y}(\frac{1}{\mu}\frac{\partial A_z^n}{\partial y}) = J_{e,z}^n \tag{4.60}$$

where n is the slice number,
μ is the permeability of the medium,
A_z is the normal component of the magnetic vector potential, and
$J_{e,z}$ is the external current density.
The rotor current is calculated from the below equation:

$$\frac{l_z/m}{S}\sum_{n=1}^{m}\frac{d(\iint A_z^n dS_+ - \iint A_z^n dS_-)}{dt}) - I_r R_r = 0 \tag{4.61}$$

where l_z is the total axial length of the machine,
S is the cross-sectional area of the rotor conductor,
S_+ and S_- represent the go and the return conductors in a rotor loop, and
R_r is the total resistance of one rotor loop.
From the knowledge of the rotor currents, it is fairly straightforward to calculate the current density in the rotor and substitute it in (4.60).
The various 2D slices are solved separately and simultaneously, however, they are constrained by the fact that the current density in a particular conductor is same in all the slices at any time instant.

Chapter 5

3D Magnetostatic modeling for BDFIM

What we observe is not nature itself but nature exposed to our method of questioning. Our scientific work in physics consists in asking questions about nature in the language that we possess and trying to get an answer from experiment by the means that are at our disposal.—Werner Heisenberg

---

Chapter summary:

The aim of this chapter is to demonstrate building a 3D magnetostatic model of the BDFIM in COMSOL Multiphysics. Various steps involved like defining physics, meshing of the BDFIM geometry and selection of the solver are presented. The simulations and the subsequent analysis are especially concerned with the effects of skew in the rotor on the axial component of the magnetic flux density. Results from the simulation are expected to give an insight into the magnetic field distribution inside the machine. The chapter ends with a brief discussion on non-linear models involving saturation.

5.1 Introduction to COMSOL

COMSOL Multiphysics is a popular finite element based software. The software consists of various modules customized to model different physical phenomenon. It is also capable of handling several physics such as thermal, electromagnetic, acoustic, etc. simultaneously in a multiphysics environment. The equations from the different physics can be coupled together or they may be decoupled.

COMSOL allows the user to define the governing differential equations and impose different relevant boundary conditions or initial states as per the problem. Various material properties are in-built; specific properties can be manually defined. Simulations in this thesis have been done using the *Rotating Machinery, Magnetic* physics module.

COMSOL provides the user with a flexible meshing and solving environment. Different shapes

of elements can be used to mesh any complex geometry. It also has a wide variety of solvers to choose from.
In this thesis, we used the **version 5.1** of COMSOL Multiphysics.

5.2 Assumptions

Essentially, every model is based on some approximations or simplifications. To quote George Box, "*All models are wrong, some are useful*". Therefore, before we go about describing the methodology behind the 3D model of a Brushless Doubly-fed induction machine, it is imperative to explicitly mention the assumptions made in the model. These assumptions are:

1. **No eddy currents are considered in the iron.** The magnetic field generated due to the eddy currents in the iron was also neglected. This is a reasonable approximation in the light of the fact that in electrical machines the iron part is laminated and as such, induced eddy currents are considerably mitigated.
2. **Effects such as skin and proximity are also neglected in the conductors.** In other words, the current density in the conductors are assumed to be uniform throughout the conductor domain.
3. **The properties of all the materials involved are assumed to be linear.** This statement is mainly applicable to the non-linear permeability of the iron at high saturation levels. Although, a way to incorporate this effect in future models has been described in this thesis.
4. **No mechanical deformations, if any, were accounted for in this thesis.**
5. **The models discussed in this work do not take into account any thermal effects.** This includes thermal expansion in the materials or the change in resistance of the conductors due to the change in temperature.

5.3 BDFIM model

The various steps involved in finite element modeling of the BDFIM are shown in Figure 5.1. These steps are briefly explained next.

5.3.1 Geometry

Creating an electrical machine geometry in 3D is by no means a trivial task. Fortunately, with a little insight and the flexibility offered by the COMSOL GUI or other modern CAD based softwares, this task is much simplified. In this section, we neglect the end windings which significantly simplifies the geometry.
We begin by making a 2D cross-section of the machine as shown in Figure 2.4. For models with zero skew, we can simply extrude this 2D geometry along the third dimension.

For models with non-zero skew, the stator and the rotor domains are extruded separately. The 3D geometries for the stator and the skewed rotor are shown in Figures 5.2 and 5.3 respectively. The airgap can be easily generated subsequently.

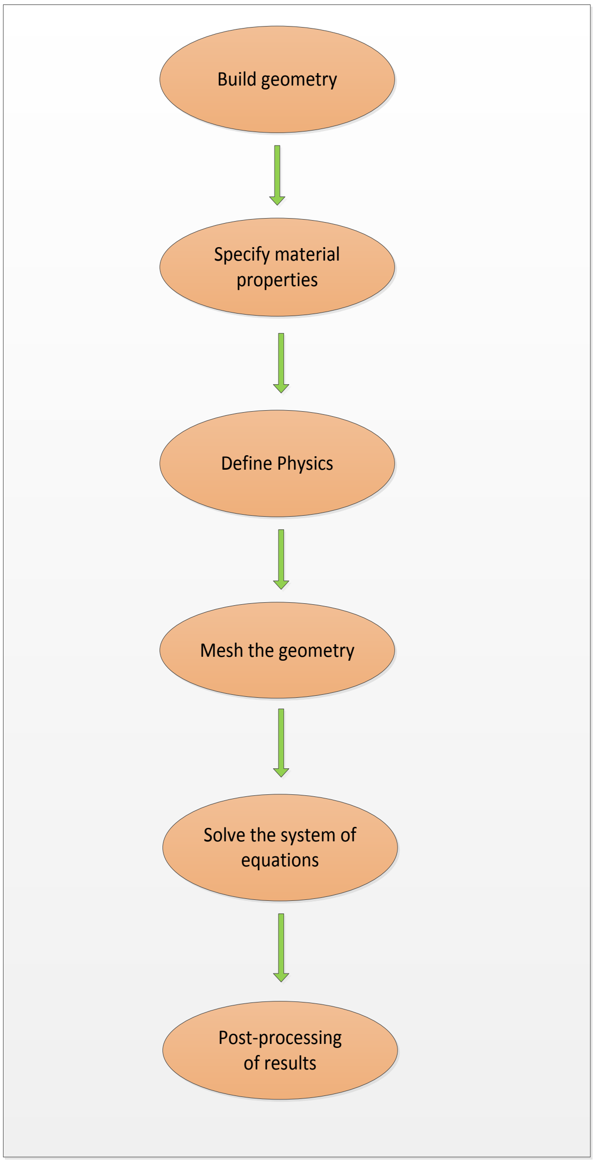

Figure 5.1: Steps involved in Finite element modeling

An important point

Sharp corners in the geometry can often lead to extremely slow or stalled convergence. This problem is usually encountered in 3D problems solved using iterative methods, such as the one we deal with in this thesis. To overcome such issues of convergence, it is recommended to avoid sharp corners or edges, and if present, round them slightly without compromising excessively on the true geometry. See Section 4-7-2.

To identify whether these sharp corners are indeed a problem, the solver must be interrupted

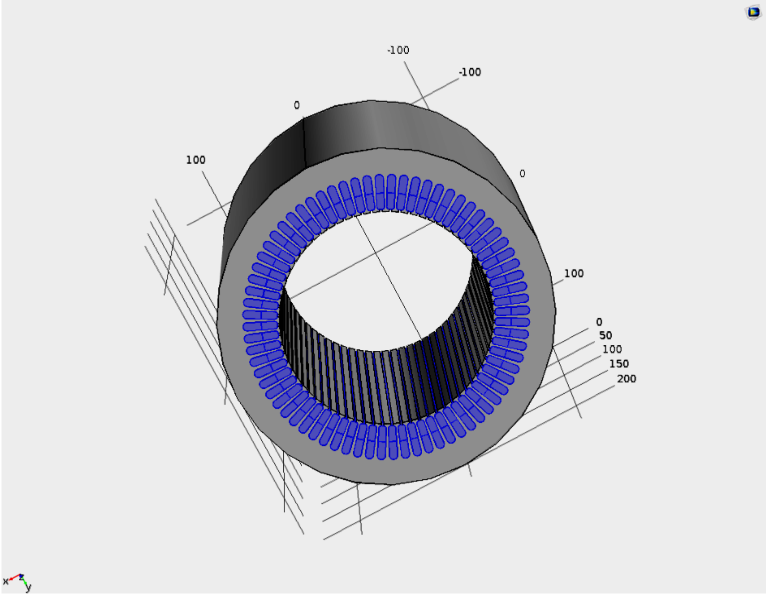

Figure 5.2: 3D BDFIM stator geometry.

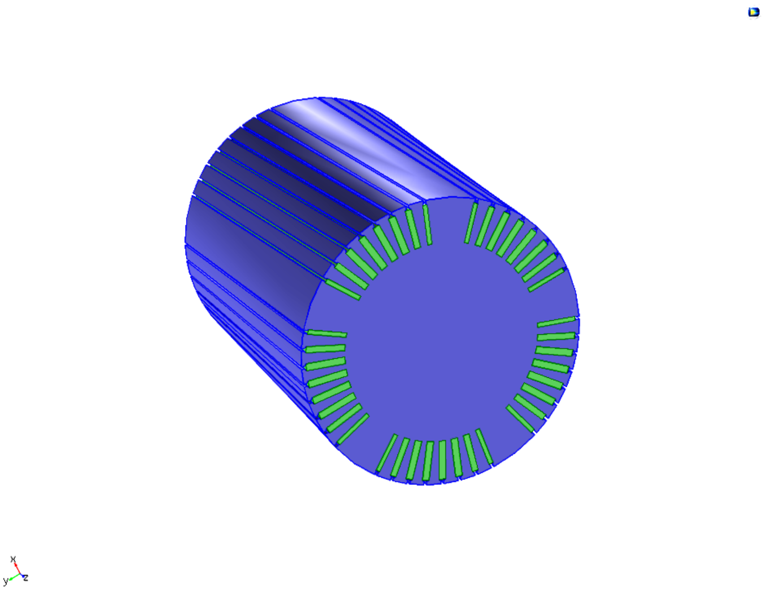

Figure 5.3: 3D BDFIM rotor geometry with skew.

once the convergence begins to stall. The regions where the solution changes abruptly must be carefully analyzed for the pitfalls mentioned here.

5.3.2 Material properties

Generally, material properties have a significant impact on the solution of the differential equation modeling a physical process. Obviously, only those properties are of interest which are included in the governing equation.

For magnetostatic modeling of the BDFIM, the only material property of interest is the permeability of the material. Since, the stator and the rotor current densities are assumed to be known and to be uniform, the conductor material can be treated similar to air. Assuming a negligible value for conductivity in the iron ensures that no eddy current effects arise in the model and thus the computation is more rapid.

For homogeneous and isotropic material domains, such as the conductors and the airgap, it is quite straightforward to define the permeability as a scalar quantity. However, for the stator and the rotor iron certain modifications are needed. This is owing to the laminated structure of the iron. This structure is illustrated in Figure 5.4.

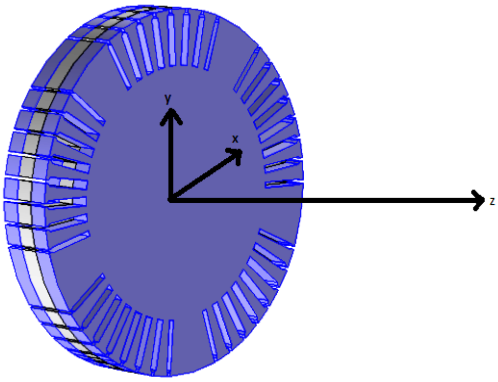

Figure 5.4: Laminated structure of iron.

Clearly, to model each laminated sheet individually, is not ideal from computational complexity viewpoint. However, it cannot be completely ignored as well. An approximate way to account for the laminations in the iron is by using the permeability tensor [46, 47].

For instance, a stacking factor of 0.95 and the relative permeability of 1000 for the iron material yields the relative permeability tensor for the laminated iron as:

$$\overleftrightarrow{\mu} = \begin{bmatrix} 950.05 & 0 & 0 \\ 0 & 950.05 & 0 \\ 0 & 0 & 19.63 \end{bmatrix} \tag{5.1}$$

5.3.3 Specifying physics

The two essential parts of solving any physical problem is to specify the governing differential equations and corresponding boundary conditions. For the magnetostatic modeling of the BDFIM, these are mentioned below.

Governing equations

For the regions formulated using the vector potential, the following differential equation applies:

$$\nabla \times (\frac{1}{\mu} \nabla \times \boldsymbol{A}) = \boldsymbol{J} \tag{5.2}$$

In a mixed formulation problem, the regions formulated using the scalar potential are governed by the equation:

$$-\nabla \cdot (\mu \nabla \phi) = 0 \tag{5.3}$$

Boundary conditions

The external boundaries of the machine can be assumed to be a magnetic insulation boundary preventing the flux from leaving the machine boundaries.
For the vector potential regions adjacent to the boundary, this can be done by imposing:

$$\boldsymbol{n} \times \boldsymbol{A} = 0 \tag{5.4}$$

For the scalar regions adjacent to the boundary, a Neumann condition can be imposed:

$$\boldsymbol{n} \cdot \boldsymbol{B} = 0 \tag{5.5}$$

Additional boundary conditions to be imposed at the interfaces between the scalar and the vector potential regions, if required, have already been mentioned in Chapter 3.

Defining current density

Consider the length of the machine to be along the z-axis. Then in case of the non-skewed rotor, the only component of the rotor current density is along the z-axis. Same cannot be said about the skewed rotor configuration.
To define the current density for the skewed rotor, we employ the cylindrical coordinates (r, θ, z). The two non-zero components of the rotor current density are then J_θ and J_z, both of them a function of the skew angle.

If J is the magnitude for the total current density, then:

$$\begin{aligned} J_\theta &= J\ t_\theta \\ J_z &= J\ t_z \end{aligned} \tag{5.6}$$

where, t_θ and t_z are derived from:

$$\begin{aligned} norm &= \sqrt{(skew * r)^2 + l_{stk}^2} \\ t_\theta &= \frac{skew * r}{norm} \\ t_z &= \frac{l_{stk}}{norm} \end{aligned} \tag{5.7}$$

Here, l_{stk} and $skew$ denote the stack length and the skew angle respectively.
The current densities in the stator are known, whereas for the rotor conductors they are taken from the results obtained in the 2D transient model [8].

5.3.4 Meshing

For models with zero skew, it is relatively easy to mesh the 3D geometry. We begin by meshing one end of the machine and then sweep the mesh throughout its length. Here, we prefer to mesh the surface using the default triangular and quad elements which on sweeping give rise to the mesh with triangular prism and hexahedral elements. This is shown in Figure 5.5. For pedagogic purposes, only half of the mesh is shown. The model though is solved for the entire geometry.
A good mesh results in swift convergence, even if it sometimes implies more number of elements or degrees of freedom. In other words, a high number of degrees of freedom does not necessarily mean more time cost for the model. The coordinates for each mesh plane along the machine length is based on the Gaussian distribution. Since, for zero skew the solution does not change in the axial direction, thus a fewer number of sweep planes can lead to convergence compared to the skewed case.

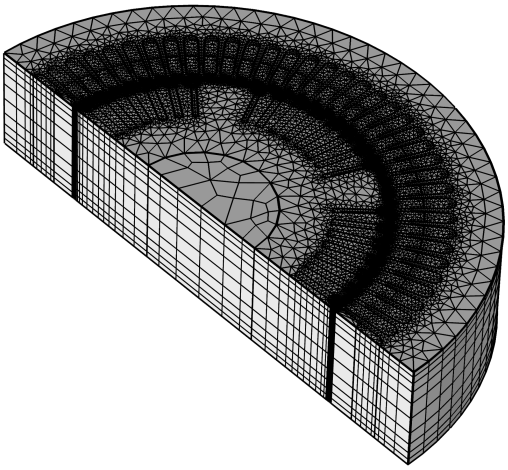

Figure 5.5: Sweep mesh for BDFIM geometry.

For models involving skew, using the default sweep mesh can be tricky; the reason is that the curve along which the mesh is swept in the stator and the rotor are different, see Figure 5.6. This problem can be solved by using a (slightly) distorted hexahedral element in the airgap as an intermediary between the stator and the skewed rotor mesh. See Figure 5.7.

One needs to be careful of the distortion in the element though. A relatively higher degree of distortion can lead to poor convergence or an inaccurate solution. To be sure of the accuracy of the solution, we increased the number of sweep planes in the mesh until the solution no longer changed or did so negligibly. In this case, we preferred using 27 Sweep planes. Opting for less than 21 mesh sweeps lead to a poor convergence, and consequently an inaccurate solution. Decreasing the number of sweeps further leads to a highly ill-conditioned system.

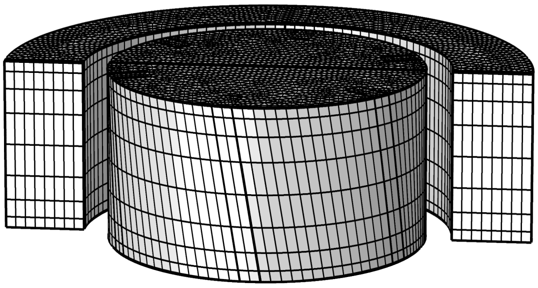

Figure 5.6: A simplified view illustrating non-conformity of the sweep mesh in the skewed rotor configurations.

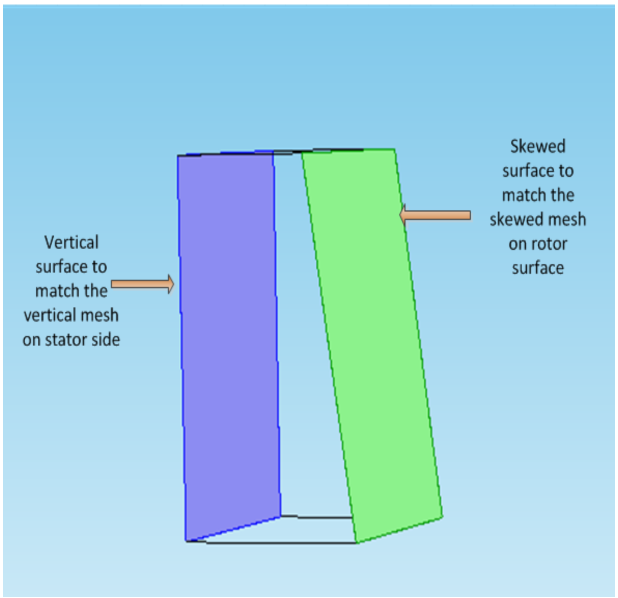

Figure 5.7: Intermediate hexahedral element in the airgap for skewed rotor.

5.3.5 Setting up Solver

The performance of the iterative solvers is highly problem specific. Many iterative solvers might be able to solve a particular system of equations, however, their performance—both in terms of computational memory and time cost—can differ vastly. Therefore, even a superficial understanding of the iterative solvers can help us to opt for the best solver for a particular problem.

If the 3D magnetostatic problem is formulated entirely using the vector potential, the resultant system of matrices is symmetric. Thus, the iterative solver of choice is the Conjugate gradients. The preconditioner used here is the Geometric multigrid (GMG), with SOR Gauge smoothers. To keep the current densities numerically divergence free, it is important to apply the divergence cleaning during all the iterations. This is done using the SOR Gauge solvers. On the other hand, if some of the regions of zero-current density are formulated using the scalar potential, and regions of the vector potential are gauged, the matrix turns out to be non-symmetric. This obviously rules out the use of CG solver and GMRES has to be employed.

The advantage of using the scalar potential in some regions, in terms of fewer degrees of freedom, is overcome by the increased expense on account of the higher memory requirement of the GMRES solver. The two cases—vector formulation and mixed formulation—are compared in Table 5-1 below. The information in the table pertains to the full axial length of the BDFIM. The number (50) mentioned alongside the GMRES solver is the number of iterations before the GMRES algorithm is restarted.

Solver	**CG**	**GMRES (50)**
Preconditioner	GMG	GMG
Smoothers	SOR Gauge	Vanka
Mesh Sweeps	27	18
Degrees of freedom	17,348,680	11,891,867
Memory usage	30 GB	31 GB
Time cost	1h 10min	1h 20min

Table 5-1: Solver comparison: CG and GMRES for 3D Magnetostatic model of BDFIM.

Clearly, the magnetic vector potential formulation using CG solver is superior in performance, and the results presented in this chapter correspond to the same combination. Table 5-2 compares the time cost of the models involving the skewed and the non-skewed models.

Solver	CG		GMRES	
Skew angle	0°	5°	0°	5°
Time cost	1h 10 min	2h 40min	1h 20 min	3h 22min

Table 5-2: Solver performance for non-skewed and skewed models.

5.4 Simulation results

5.4.1 3D plots for norm of B

Here we shall compare the distribution of the magnetic fields in the rotor and the stator iron for the non-skewed and the skewed rotor configuration. The plots correspond to the positions shown in Figure 5.8.

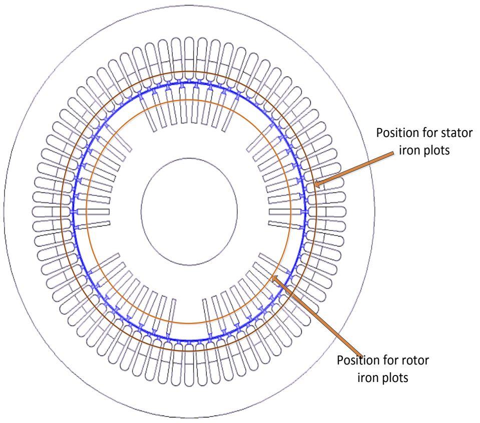

Figure 5.8: Positions of the stator and the rotor iron plots.

Figures 5.9 and 5.10 show the surface plots for the norm of the magnetic flux density in the rotor and the stator parts respectively, for the rotor with zero skew. The banded distribution of the flux density is owing to the presence of the slots.

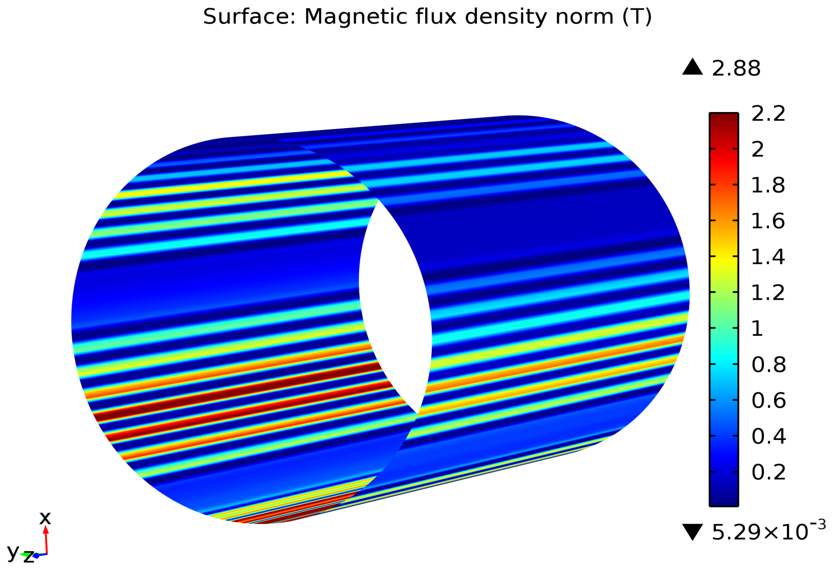

Figure 5.9: Norm of radial flux density in rotor iron

As for the skewed rotor, the magnetic flux density plots in the rotor and the stator parts are shown in Figures 5.11 and 5.12. The skew in the rotor is clearly evident in Figure 5.11.

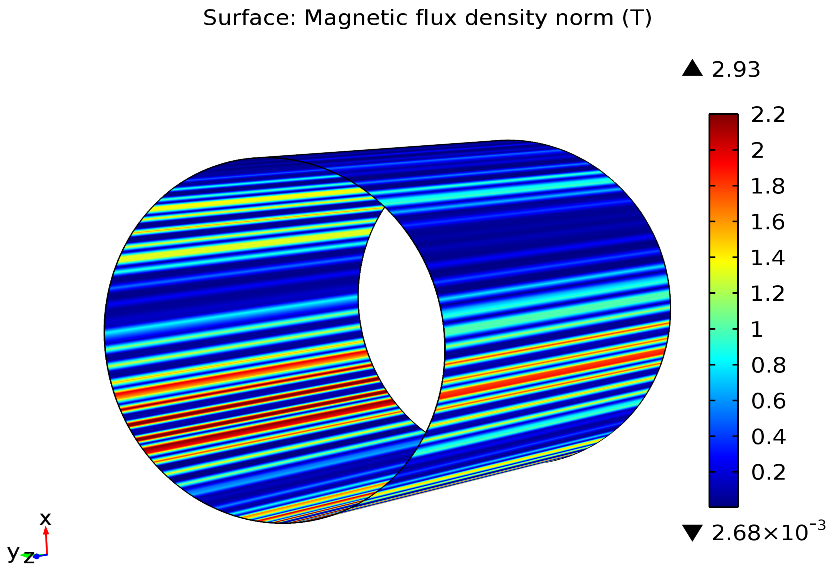

Figure 5.10: Norm of radial flux density in stator iron

The rotor conductors are skewed by 1 stator slot each in this case. Also, as is evident, the magnetic field norm increases from one end of the machine to the other, unlike to what was observed in the non-skewed case.

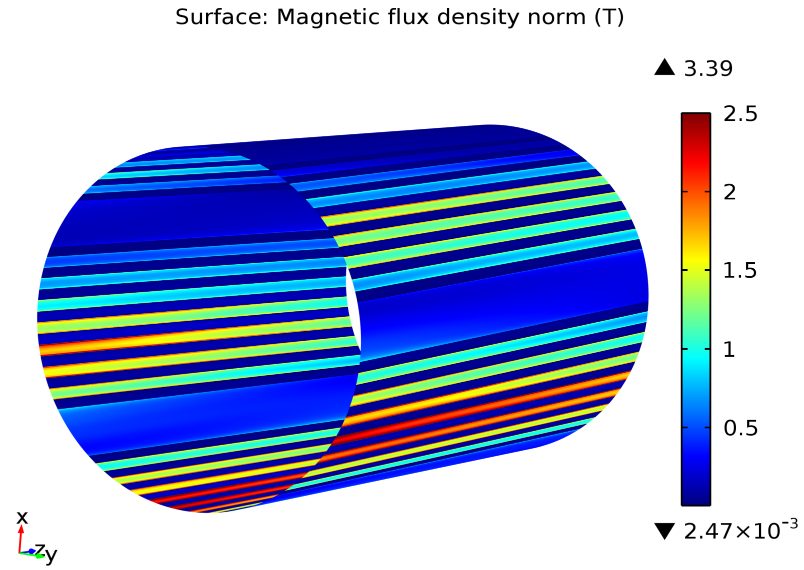

Figure 5.11: Norm of radial flux density in rotor iron for skewed rotor

5.4.2 1D plots for Radial flux density

The radial flux density in the airgap is plotted at three different axial coordinates, one near each end of the machine and one at its centre. For the non-skewed rotor, the plots are shown

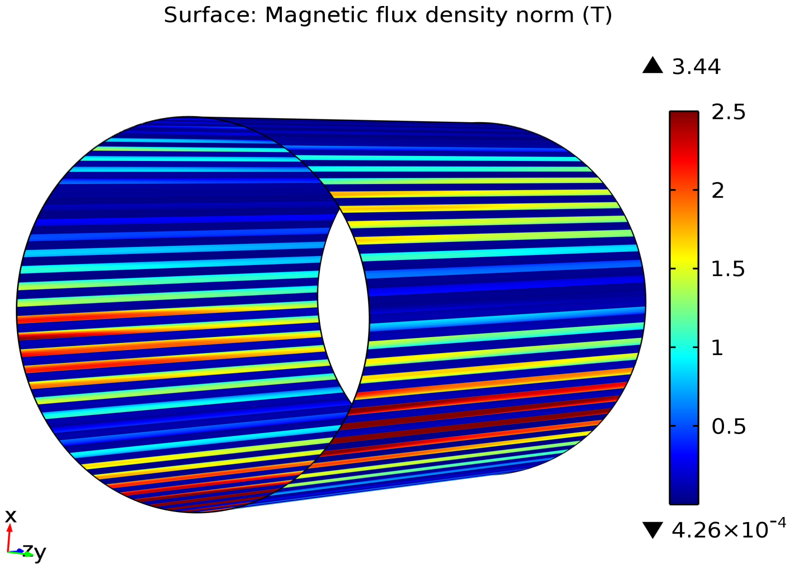

Figure 5.12: Norm of radial flux density in stator iron for skewed rotor

in Figure 5.13. As expected, the three plots overlap on each other due to the homogeneity in the structure along the axial direction.
On the other hand, similar plots for the skewed rotor configuration tend to differ from each other, as can be seen in Figure 5.14. Obviously, this is a result of the non-homogeneity in the structure axially.

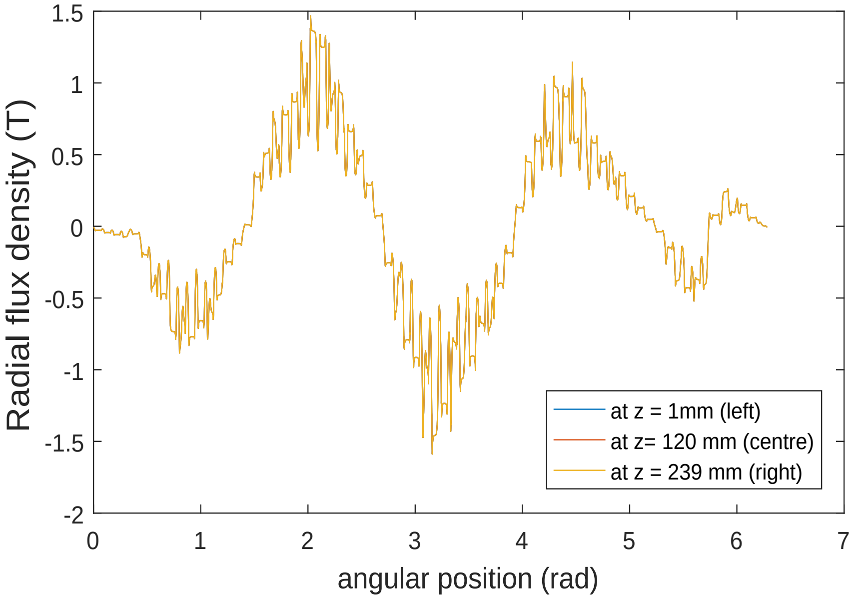

Figure 5.13: Comparison of Radial flux densities at three different axial positions for non-skewed rotor.

This difference in the radial flux density plots can be attributed to two factors. First and

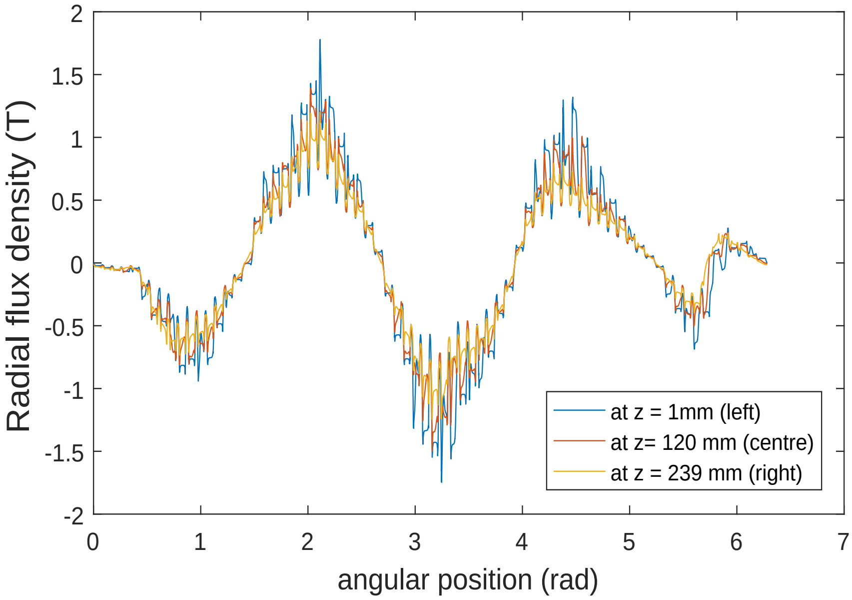

Figure 5.14: Comparison of Radial flux densities at three different axial positions for rotor with 1 stator slot skew.

foremost is the change in the relative phase shift between the stator and the rotor currents, whilst moving from one end to the other of the machine. And the second, is due to the presence of the axial flux. This axial flux, arising from the circumferential component of the rotor currents, aids the radial flux at one of the machine while opposing it at the other.

5.4.3 Magnitude of axial flux

Figure 5.15 shows the magnitude of the axial flux component in the rotor iron with the permeability given by (5.1). On increasing the stacking factor to 0.97, the magnitude of the axial flux component increases as expected, as shown in Figure 5.16. The magnitude of the axial component is still relatively negligible compared to the radial flux density component. If however, we were to assume isotropic properties, the axial flux component would have been significant as seen in Figure 5.17. Clearly, the laminated nature of the iron offers high reluctance along the axial direction.

Also, towards the edges it can be observed that there is a slight decrease in the magnitude of axial component. This is due to the fact that at these boundaries, the axial flux changes its direction and combines with the radial flux.

5.4.4 Impact of axial flux on rotor currents

Earlier, we have mentioned the two reasons due to which the rotor current in the skewed case differs from the non-skewed case. One of those, the change in the relative phase shift between the stator and the rotor currents from one end of the machine to the other, is taken care of in the 2D multi-slice model. However, the effect of the axial flux is neglected therein.

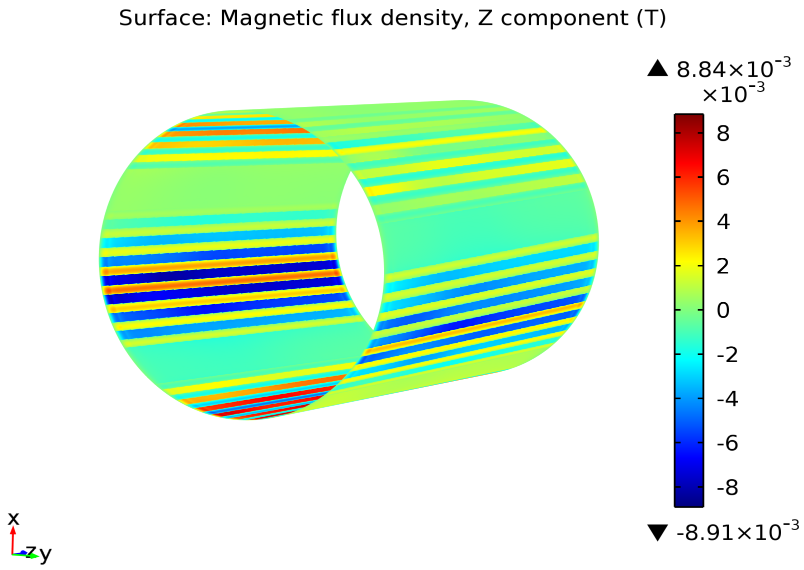

Figure 5.15: Magnitude of axial flux inside the rotor iron for a stacking factor of 0.95 .

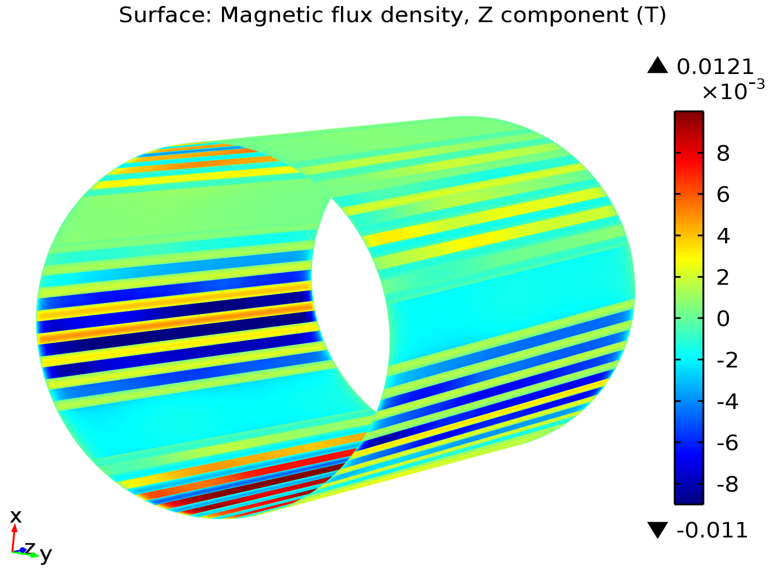

Figure 5.16: Magnitude of axial flux inside the rotor iron for a stacking factor of 0.97 .

To establish the effect of the axial flux on the rotor currents, we compare the plots for the radial flux density in the airgap under two scenarios. In the first case, we use the effective permeability tensor for the iron, as given by (5.1). See Figure 5.14. In the second case, we replace the permeability along the axis of the machine with that of the air so as to minimize the axial flux as much as possible. The permeability tensor is then:

$$\overleftrightarrow{\mu} = \begin{bmatrix} 950.05 & 0 & 0 \\ 0 & 950.05 & 0 \\ 0 & 0 & 1 \end{bmatrix} \tag{5.8}$$

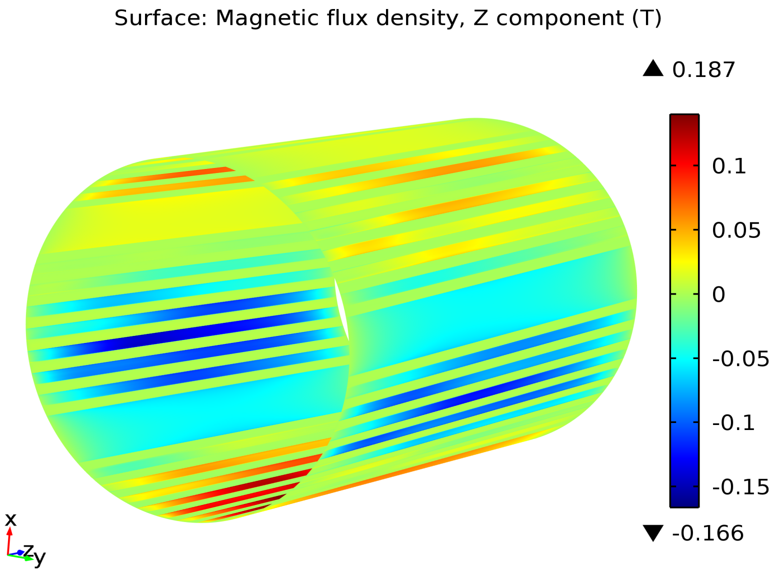

Figure 5.17: Magnitude of axial flux inside the rotor iron assuming isotropic properties.

The result from the simulation corresponding to the latter case is shown in Figure 5.18.
As can be seen from Figures 5.14 and 5.18, the differences in the radial flux density plots, even though present, is minimal. Since, the rotor currents are a function of the radial flux density, we can safely conclude that—under given circumstances—the effect of axial flux arising from the skewed rotor conductors on the rotor currents is negligible.
An alternate way of arriving at the same conclusion would be to calculate the flux linkage in the two cases, at the same rotor position and time instant, and compare the results. To avoid redundancy, we do not present those results here.

5.4.5 Comparison with the 2D multi-slice model

To see how predictions from the 3D model compare with the erstwhile developed 2D models, we must opt for a comparison parameter. In this section, we compare the torque values as obtained from the 3D model and the 2D multi-slice model, which was introduced in the previous chapter. Figures 5.19 and 5.20 plots the torque values for the non-skewed and the skewed rotor configurations respectively.

The difference in the 2D multi-slice and the 3D model torque values for both the cases is somewhat similar, and more or less constant. The values obtained from the 3D models are approximately 2-3% lower compared to the values predicted from the 2D multi-slice models. However, this difference corresponds to the stacking or of 0.95. With increasing stacking factor, this difference obviously approaches more closely to the values predicted by the 2D model.
An important point to be noted here is the manner in which the torque is calculated from the 2D model. In the 2D multi-slice model, the torque obtained per unit length is multiplied by the axial length of the machine to obtain the total torque. No compensation is made for the laminations in the iron.

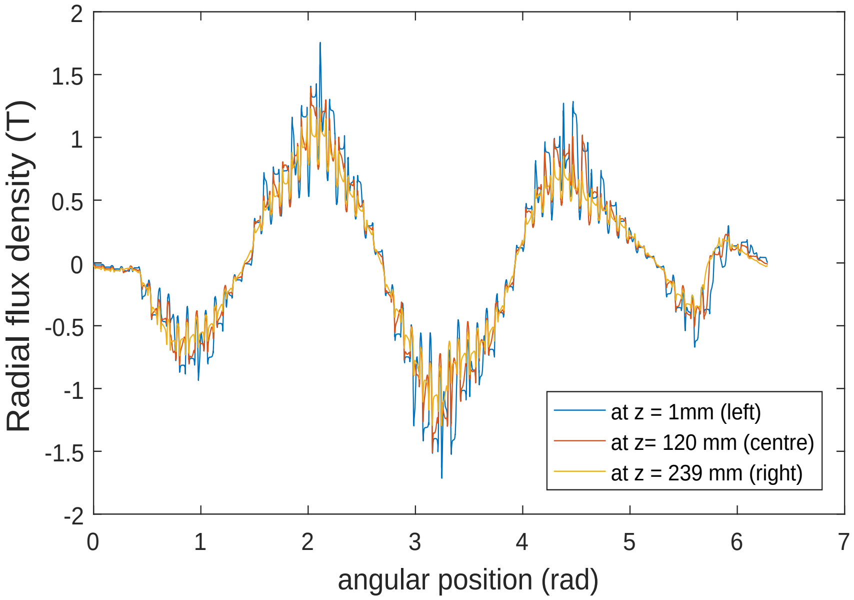

Figure 5.18: Comparison of radial flux densities at three different axial positions for the rotor with 1 stator slot skew, and permeability of iron as given in (5.8)

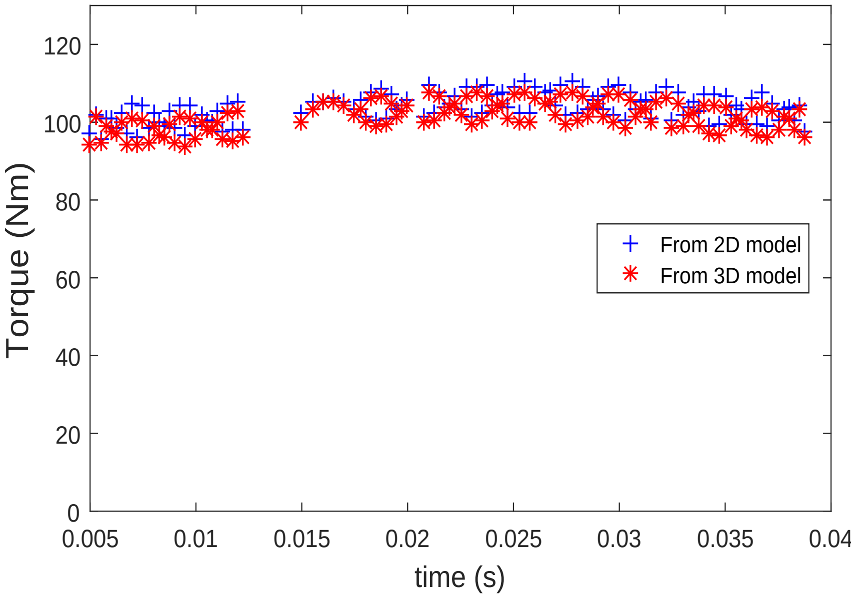

Figure 5.19: Comparison of torque values for non-skewed rotor.

Implementing Maxwell Stress Tensor method for torque computation

The choice of torque for comparison purposes is purely arbitrary. Equivalently, loss comparisons could also have been done. The torque in both the models has been calculated by the Maxwell Stress Tensor (MST) method. MST is easier to implement compared to other methods such as Virtual Work in 3D as it requires relatively fewer computations.

There are few points one should be careful of while using the MST method in FEM discretized

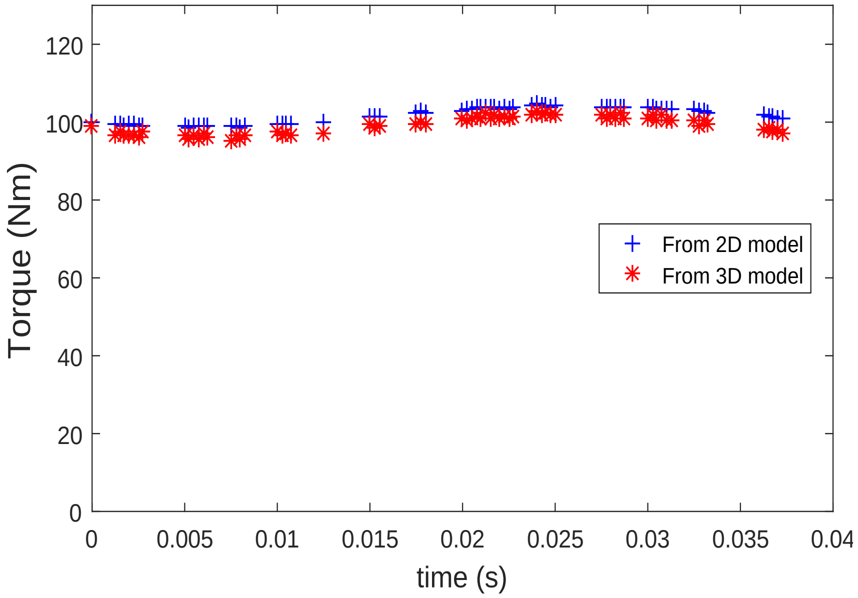

Figure 5.20: Comparison of torque values for rotor with 1 stator slot skew.

models. The values obtained from the MST method are highly mesh sensitive, therefore, a poor quality mesh can lead to spurious values. Ideally, the radius in the airgap at which the MST method is employed should be irrelevant for the torque values; however, often this is not the case due to numerical issues. If indeed by varying the radius of the integration surface leads to negligible variations in the torque values, the mesh quality can be assumed to be good.

Corners near the slot openings can lead to very high and often incorrect values for the derivative of the magnetic potential in the airgap. This can result in inaccurate values of the field in the region. It can be avoided by slightly rounding off these corners. Another point to be considered is that the integration surface must not be in close proximity to either the stator iron or the rotor iron. Also, to avoid errors it is suggested that the integration surface does not coincide with the element faces in the airgap.

Besides the mesh quality in the airgap, the number of integration points chosen on the surface on which the stress tensor is evaluated also has an impact on the calculated torque values. In most cases, the torque values attain a constant value beyond a certain number of points. Therefore, it is recommended to increase the resolution until such a stage is reached.

5.5 Results from the non-linear model

Due to the time limitations we have neglected the non-linear nature of the permeability in the iron, in most of the simulations. However, this effect is encountered more often than not in practice, and hence, we describe an approximate method of incorporating this in the future models.

The problem involving a non-linear iron is solved using the damped Newton-Raphson method. Usually, there is a possibility of non-convergence in non-linear cases if the initial guess is far off from the final solution; in other words, when current densities are high enough to cause deep saturation. Therefore, it is sometimes necessary to ramp up the current densities (or the source vector) gradually, and using the previous solution as an initial guess for the next iterate with a higher current density. Current ramping was employed in the below mentioned model. The non-linear model was first solved with a peak current density of $5 \times 10^5\ A/m^2$, and the solution from this case was taken as an initial guess for the model with a peak current density of $1 \times 10^6\ A/m^2$. No such stepping up of current densities is required for the linear case.

To illustrate our point, we consider a BDFIM model with an axial length of 24mm and 0 degree skew. The number of degrees of freedom in this case is 3,055,794.

A magnetostatic simulation assuming linear properties of iron is solved within 11 minutes. On the other hand, the similar model with non-linear iron takes 1 hour and 4 minutes. The difference in time cost increases with the increase in the number of degrees of freedom.

The plot for norm of $\boldsymbol{B}$ in the machine cross-section for the linear and the non-linear case are shown in Figures 5.21 and 5.22 below.

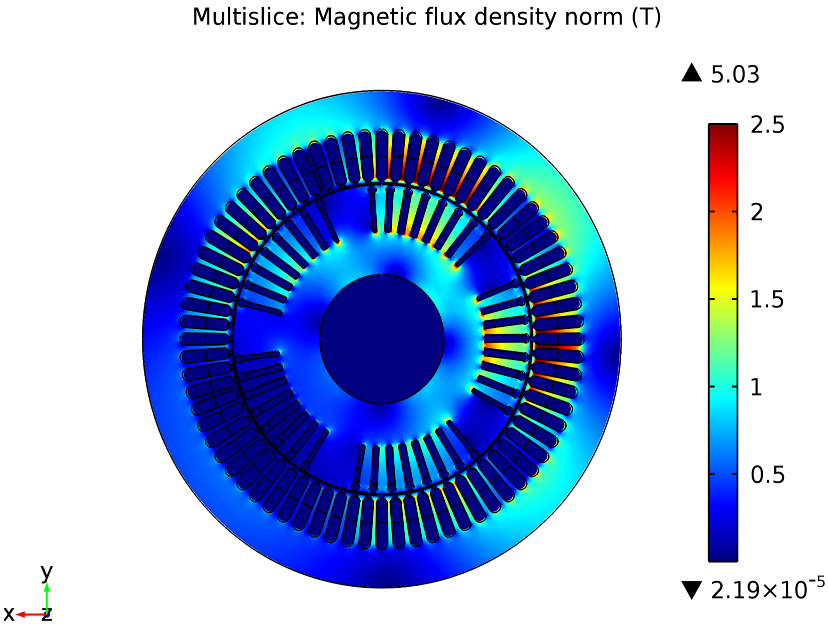

Figure 5.21: Plot of norm B from the linear model.

The difference between the peak value of the magnetic flux density (as shown on the scale on right side of the figures) is clearly evident. The peak value is smaller as expected when saturation is taken into account. Needless to say that higher the degree of saturation, greater is the difference in the results predicted from the linear and the non-linear case.

5.6 Inferences

The 3D model for the BDFIM discussed in this chapter takes both the axial flux arising from the skewed rotor as well as anisotropy of the iron into account. These factors as mentioned

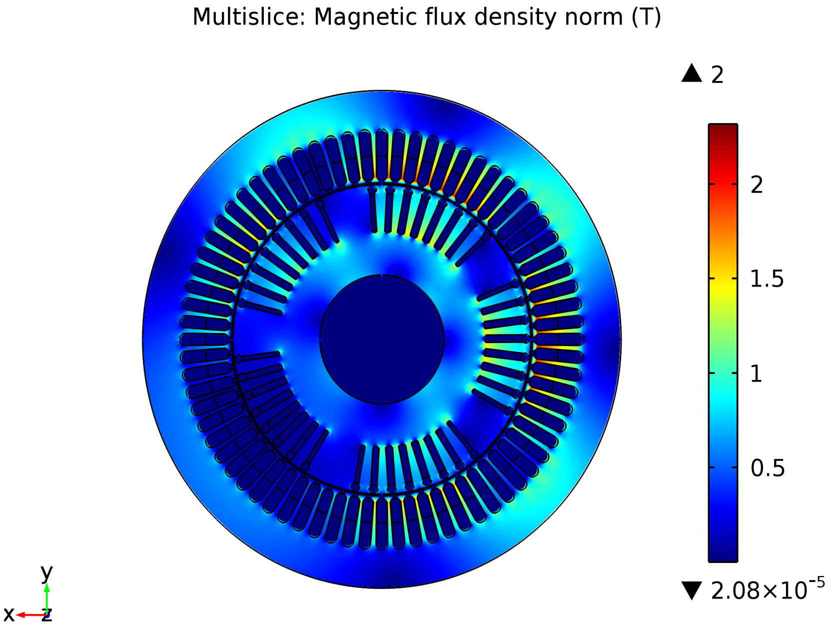

Figure 5.22: Plot of norm B from the non-linear model.

at the outset of this thesis have been neglected in the 2D models heretofore, including the multi-slice model.

From the analysis presented in this chapter it is evident that the presence of the axial component of the magnetic flux density in the machine does alter the estimated torque values significantly. Same can be said about the associated torque ripple and the power developed (for constant speed operation).

Incorporating the anisotropic nature of the iron does lead to a slight decrease in the estimated torque values, compared to an isotropic iron and neglecting the laminated structure. However, this decrease is more or less constant and therefore, should not significantly alter the estimation of the torque ripple .

The axial component of the magnetic flux is normal to the plane of laminations, and therefore, it can give rise to huge eddy current losses. Fortunately, however, the laminated structure of the iron not only limits the eddy losses due to the radial flux but also offers significant reluctance in the axial direction. This reluctance to the axial flux substantially decreases its magnitude resulting in minimal losses.

Chapter 6

Transient Modeling for BDFIM

We are at the very beginning of time for the human race. It is not unreasonable that we grapple with problems. But there are tens of thousands of years in the future. Our responsibility is to do what we can, learn what we can, improve the solutions, and pass them on.—Richard Phillips Feynman

---

Chapter summary:

The chapter introduces various concepts involved in the transient modeling, involving motion and circuit equations, for electrical machines. Special attention is paid to the transient models of induction machines in 3D and BDFIM in 2D. Suitability of solvers such as CG and GMRES is discussed for transient models involving motion. Much of the discussion in this chapter is generic in nature, however, some terms introduced are specific to COMSOL Multiphysics.

6.1 Introduction

Rotating electrical machines comprises of two main components: the stationary part (or the stator) and the moving part (or the rotor). Involving two distinct and complex domains, with one rotating and the other stationary makes modeling of such machines cumbersome. To do so in 3D and perform a transient study makes the task even more difficult. Though smart transformations can sometimes allow the user to transform the problem from a moving domain into a stationary one, it is not always possible; especially, if one intends to capture or observe some effects arising out of the anisotropy resulting from the motion. Therefore, transient modeling of rotating electrical machines in 3D remains an area of active interest.

6.2 Geometry definition allowing rotor motion

Finite element models of rotating electrical machines comprises of an *assembly*[1] of two disjoint geometrical entities or objects—the stator and the rotor objects. These two objects are connected by a sliding boundary layer in the airgap. The problem formulation is completed only after imposing the continuity of the relevant potential across this boundary. To achieve good convergence and accurate results, it is important to set up such an interface somewhere near the middle of the airgap. Therefore, the stator object then comprises of the stator iron, stator windings and the airgap section adjacent to it; and same applies for the rotor object. This is unlike other FEM problems where the problem domain or boundaries remains stationary with time, and the geometry comprises of a one complete geometrical entity or the *union*[2]. For instance, in cases where we are interested only in a static solution such as the one in the previous chapter.

An advantage of using the *assembly* over the *union* is that it allows for the relative motion between the domains. The rotor part of the model is generally solved in a rotating reference frame whereas the stator is solved in the stationary frame. Another advantage is that it allows for the non-conforming meshes on the stator and the rotor sides.

While solving for the domains in the stator and the rotor objects, which are not adjacent to the interface boundary, the choice for the Scalar or the Vector potential formulation is usually straightforward. Quite often the slots with current carrying conductors are modeled using the Vector potential. In regions where the current density is assumed to be zero, for instance, the laminated iron, can be formulated using the Scalar potential. However, there can be exceptions as explained in the next section.

6.2.1 Arbitrary Lagrangian-Eulerian formulation

The governing PDEs of a problem are usually formulated either in a spatial frame of reference or in a material frame of reference. In the former case, also known as the Eulerian formulation, the coordinate axes remain static in space. In the latter case, also known as the Lagrangian formulation, the coordinate axes follow the material as it moves or deforms. Both formulations have their advantages and drawbacks.

Eulerian approach is more favorable when the information regarding the state variables is more important at fixed points in space. However, it cannot handle moving domain boundaries effectively. On the other hand, the Lagrangian approach—since, it is written in the material frame—can easily tackle such problems. In addition to this, the inclusion of history-dependent constitutive relations is also facilitated. The limitation though with the Lagrangian approach is its inability to follow huge distortions in the material without recourse to remeshing [48]. Arbitrary Lagrangian-Eulerian (ALE) formulation was developed to overcome the shortcomings of the aforementioned formulations. The ALE approach involves writing PDEs on a freely moving mesh coordinates. Under special circumstances, this mesh can coincide with the spatial one resulting in a Eulerian formulation. In some other cases, the mesh follows a deforming or a moving material resulting in a Lagrangian formulation [49].

For rotating electrical machines, this usually implies writing of the field equations for the stator domains in the spatial or the Eulerian frame, and for the rotor domains in the material

---

[1] The term used here is in accordance with the COMSOL nomenclature.

[2] See footnote 1.

or the Lagrangian frame. The electromagnetic fields in the two frames are related by the following equations:

$$\begin{aligned} \boldsymbol{B}_{material} &= \boldsymbol{B}_{spatial} \\ \boldsymbol{E}_{material} &= \boldsymbol{E}_{spatial} + \boldsymbol{v} \times \boldsymbol{B}_{spatial} \end{aligned} \tag{6.1}$$

where, $\boldsymbol{v}$ is the relative velocity between the two frames.

6.3 Potential formulations in the airgap

For the machine models to give reasonable results, it is imperative to ensure the continuity of potential across the interface between the stator and the rotor. This is done by introducing the Lagrange multipliers at the interface boundary. In COMSOL Multiphysics, one needs to add the *Continuity* node under the *Rotating Machinery, Magnetic* physics, to enable this feature. In other words, the Continuity feature ensures the transparency of the flux between the stator and the rotor entities. This continuity of the potential generally involves some interpolation as the meshes on two sides of the interface are not conforming at every time instant. The reason that it is recommended to implement the scalar potential formulation in 3D models, on both sides of the interface, is that the interpolation errors involved with scalar potential have little impact on the numerical stability. On the other hand, if the vector potential is used, the resulting interpolation errors lead to the violation of the current conservation law, which is a consequence of the Ampere's law. As such, these interpolation errors render such models almost invariably numerically unstable [50]. These numerical issues may be amplified when one uses the iterative solvers for the problems in 3D. Such problems do not arise in 2D, and the vector potential (z-component) is used throughout the model. Other finite element softwares, such as FLUX 3D, also resort to scalar potential formulation in the airgap. However, if we can ensure that the meshes on both sides of the interface are exactly the same at every time instant, vector potential formulation can be employed in the airgap. This can only be done by remeshing airgap at each time step, and thus may not present an efficient way to tackle such problems.

There is another consideration one must take into account when using the Scalar potential formulation. The domains modeled using the scalar potential must be *simply connected.* A region is simply connected if any closed loop inside the region does not encircle an external domain. In this case, an external domain carrying a current. If that's the case, then closed loop line integral of the Magnetic field inside the region is not zero, which is the prerequisite for using the Scalar potential in the region [51–53]. Figure 6.1, taken from[51] below illustrates some basic configurations which can or cannot be formulated with the Scalar potential. The blue regions in the Figure 6.1 represent domains formulated using the Vector potential and the grey regions represent current-free domains, which are formulated using the Scalar potential. Figure 6.1(a), depicts an invalid topology as the Scalar potential region encircles a current carrying conductor and hence, violates the Ampere's Law. Figure 6.1(b) shows some valid topologies.

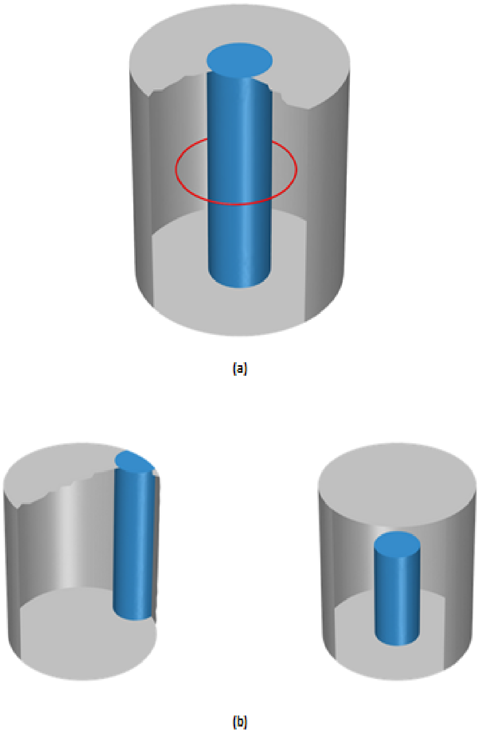

(a)

(b)

Figure 6.1: (a) An invalid configuration (b) Valid configurations

6.4 3D transient model for an Induction machine

In the previous chapter we have discussed the 3D magnetostatic model of the BDFIM. A logical next step would have been to discuss the 3D transient model for the same machine. However, in general, transient models are mathematically more complex and time consuming to handle. In addition to this, the geometric structure needed for the transient model of the BDFIM to incorporate motion, makes it more cumbersome to mesh and solve the resulting system of equations. This point should become clear later in this section. Nonetheless a 3D transient model for the BDFIM, or any similar machine, can always be made, provided we have adequate computation resource and processing power.

Therefore, for illustrative purposes, we shall demonstrate a 3D transient model of a simplified induction machine, involving motion and circuit equations. The 3D transient model for the BDFIM presented in previous chapter can be made along the similar lines, however, with a significant memory usage and time cost.

The three phase induction machine, in this case, has been made with 2 slots/pole/phase and with one loop of the rotor conductor. Based on the previous discussion, the airgap is divided into two sections, the stator and the rotor parts. An interface between the stator and the rotor is setup in the airgap. For numerical stability, the magnetic field on both sides of the interface in the airgap, is derived from the Scalar potential. The rest of the regions in the model are formulated using the Vector potential. Each rotor bar is surrounded by the rotor iron on the three sides and the airgap on the fourth. To avoid situation similar to the one presented in Figure 6.1(a), it becomes unavoidable to model the rotor iron with Vector potential as well, regardless of the fact whether the eddy currents are neglected or not. See Figure 6.2.

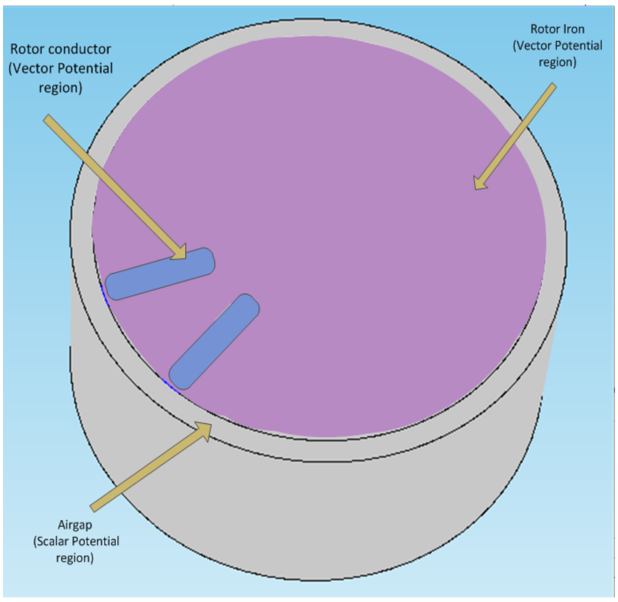

Figure 6.2: Top view of a simplified rotor object with only two rotor conductors

To ensure that the airgap remains simply connected, the shape of the airgap needs to be altered. This can be done by connecting the airgap surrounding the rotor on either the top or the bottom or both. In this case, as shown in Figure 6.3, we do so only on the top side.

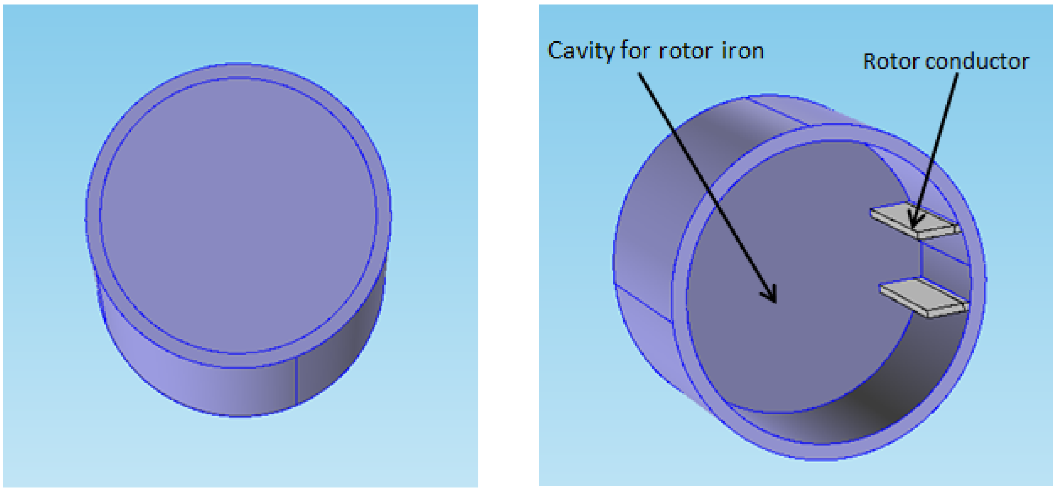

Figure 6.3: (a) Top view of simply connected rotor airgap (b) Bottom view of the simply connected airgap

There is another constraint though that is introduced by modifying the shapes of the airgap. That is, the current conservation law is not satisfied at the top surface of the rotor iron, if the current loop is not defined properly. This can be a cause for an ill-posed problem and hence, needs to be done away with. A current loop must be appropriately defined to avoid any singularities that might arise due to the incomplete loop. Therefore, the modeling of the end winding becomes necessary at least on one end of the rotor as shown in the Figure 6.4 . Again to avoid any loops in the scalar potential region encircling a current carrying conductor, the air surrounding the end winding must be modeled using the Vector potential.

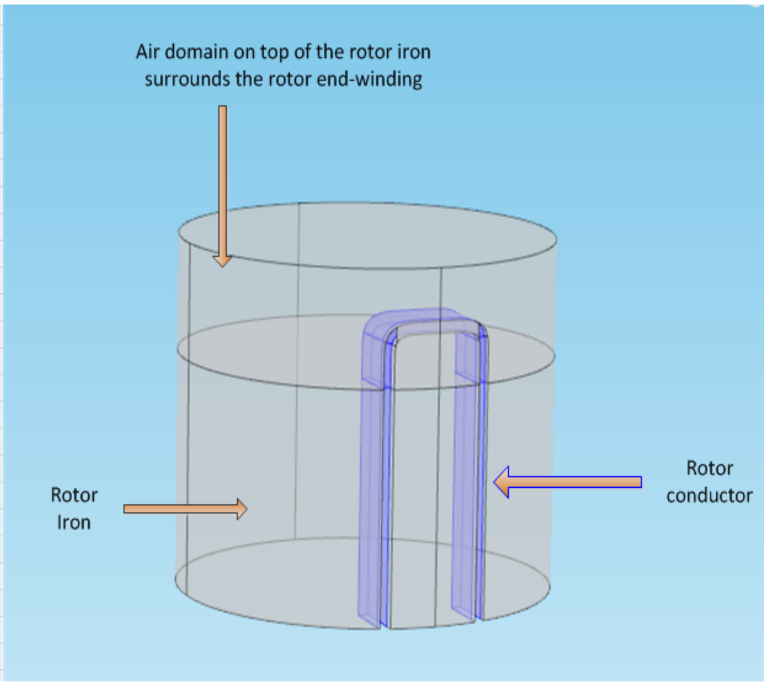

Figure 6.4: All domains shown in this Figure are modeled using Vector potential

Similar to the airgap section adjacent to the rotor object, the constraint of simple connectedness also applies on the airgap section adjacent to the stator. Therefore, the final shape taken by airgap is as shown in Figure 6.5. Domains shaded blue are formulated using Vector potential.

Figures 6.6 and 6.7 show the top view and the bottom view of the full machine geometry respectively.

The next step in the modeling is to define the circuit equations for the evaluation of the rotor currents, and to couple them with the unknown vector potential degrees of freedom.

6.4.1 Evaluation of rotor currents

In case of the skewed rotor, defining the current density components is a little tricky due to its skewed geometry, as shown in the previous chapter on magnetostatic modeling. It can be even more challenging to define the current density components for the conductors which involve end windings or nested loops.
In case of an induction machine model, the rotor currents are unknown at the outset. However, they can be evaluated by incorporating a predefined equation in the model expressed in terms of the field variables. This results in a coupled field-circuit finite element model [54]. The rotor currents are calculated based on the induced electric field obtained implicitly from the model while knowing the resistance of the rotor loop. The complex shape of the rotor conductors in case of the end-windings makes it slightly difficult to define the current

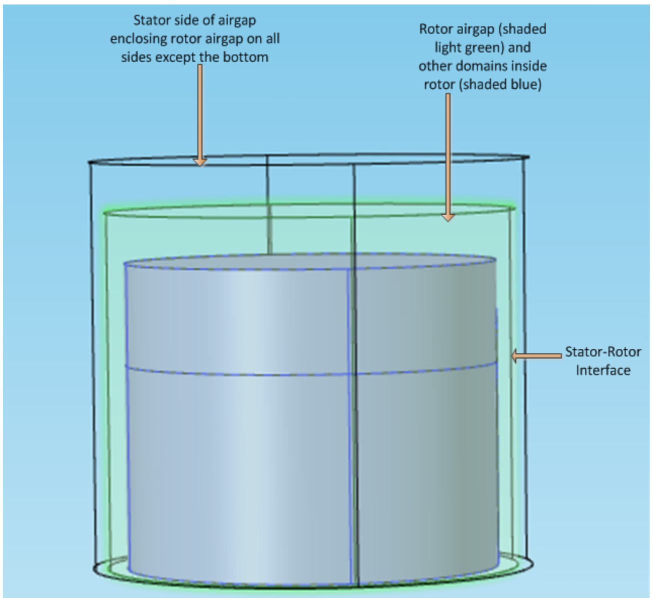

Figure 6.5: Rotor domains, rotor and stator sections of the airgap.

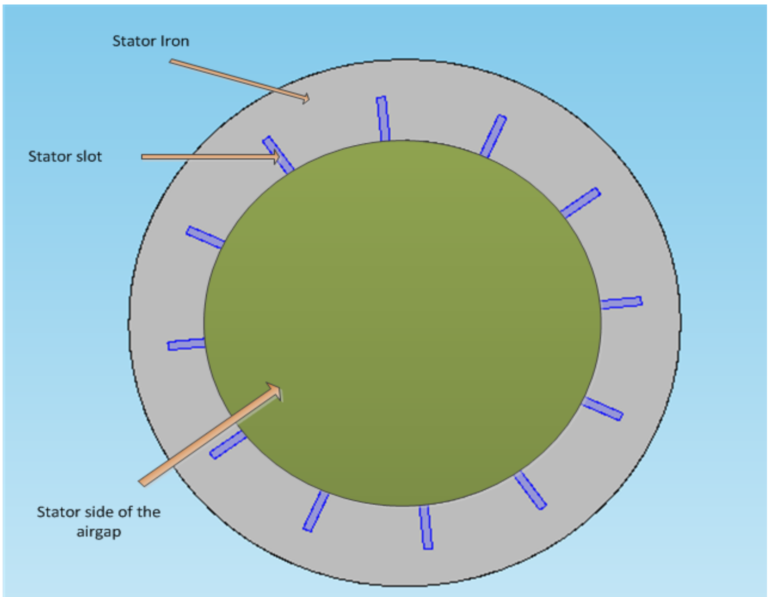

Figure 6.6: Top view of a simplified rotating machine

density along any particular coordinate axes. In calculating the rotor current from such a methodology, it becomes imperative to evaluate the integral of the electric field along the rotor conductor axis, which maybe a complex curve. Though simpler transformations might exist in simple cases where the electric field along the length of the rotor can be easily calculated knowing its components along the cartesian coordinates, we present a more general approach here.

We propose using the Curvilinear coordinates for geometrical entities with non-trivial shapes. In the present case, one such entity is the rotor conductor. In the rotor frame, the current

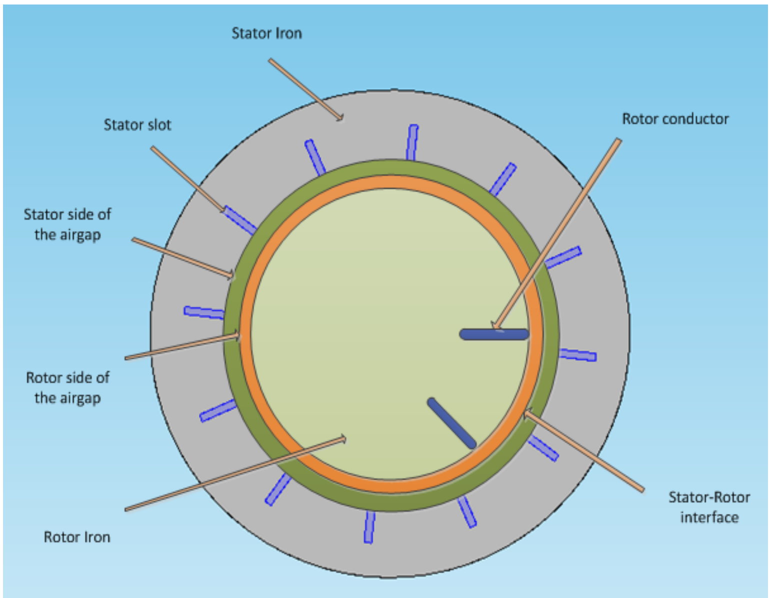

Figure 6.7: Bottom view of a simplified rotating machine

can be calculated using the Ohm's law:

$$\int_0^L \boldsymbol{E} \cdot \boldsymbol{dl} - I_r R_r = 0 \tag{6.2}$$

where, L, I_r and R_r represent the length of the rotor, induced rotor current and the rotor loop resistance respectively. The electric field corresponds to the rotor frame.

For the 2D transient model,the above equation takes the form [54]:

$$\frac{L \iint \boldsymbol{E} \cdot \boldsymbol{ds}}{\iint ds} - I_r R_r = 0 \tag{6.3}$$

where $\iint ds = S_r$ is the cross-sectional area of the rotor conductor.

Similarly, for the 3D case, the induced current is evaluated using the following equation:

$$\frac{\iiint E_{cc} dv}{\iint ds} - I_r R_r = 0 \tag{6.4}$$

where, E_{cc} and dv represent the component of the electric field along the curve traversed by the rotor conductor and the volume element inside the rotor conductor respectively. The direction of the E_{cc} is as shown in Figure 6.8.

The electric field vector along the rotor conductor in a caged rotor is given by:

$$\boldsymbol{E} = -\frac{\partial \boldsymbol{A}}{\partial t} \tag{6.5}$$

We can compute the curvilinear coordinates for any general shaped object by using the *Diffusion method*, which essentially solves the Laplace equation over that object with defined

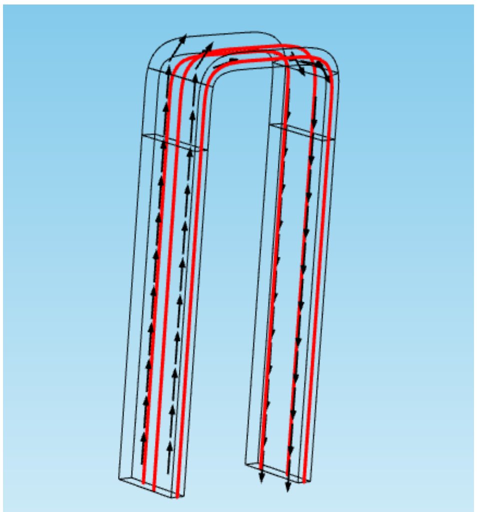

Figure 6.8: Unit vector along the rotor conductor

potentials at the inlet and the outlet boundaries. The method employed is a scalar potential and is usually suitable for smooth geometries, as in this case. Using curvilinear coordinates can be very handy to define anisotropic material properties for a curved object [49, 55]. Obviously, the field equations are solved in the spatial or the material frame. The field components along the curvilinear coordinate axes are then computed from the spatial (or material) frame components using the corresponding transformation matrix.

6.5 Model simulation and results

To begin with we solve the model with the gauged vector potential using direct solvers. The three phase stator winding is supplied with a balanced current source at 50 Hz. The rotor is rotating at 300 rpm. The model has 207,741 degrees of freedom. For a time step of 0.0025 s from 0 to 0.01 s, the run time was 6 hours and 32 minutes. The waveform for the induced rotor current is shown in Figure 6.9. If instead of saving the results only at the predetermined time instants, and rather doing it at all the time steps taken by the solver, we see a smoother waveform for the rotor current. See Figure 6.10.

6.6 Iterative solvers for transient studies

In the previous chapters we have shown that direct solvers are incapable of handling large scale 3D problems, and hence, the recourse to iterative methods. The same argument motivates the application of iterative solvers to 3D transient problems. The transient model for the BDFIM differs from the magnetostatic case in two aspects. Firstly, transient models involve moving domains and secondly, there are additional degrees of freedom arising from the unknown rotor currents. Both of them have an impact on the choice of the iterative solvers to be employed in such cases. We shall illustrate this with the help of a 2D model for the BDFIM in this section.

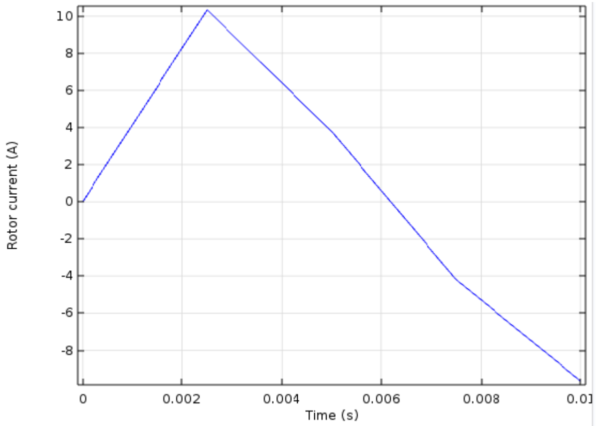

Figure 6.9: Induced rotor current for a time step of 0.0025 s

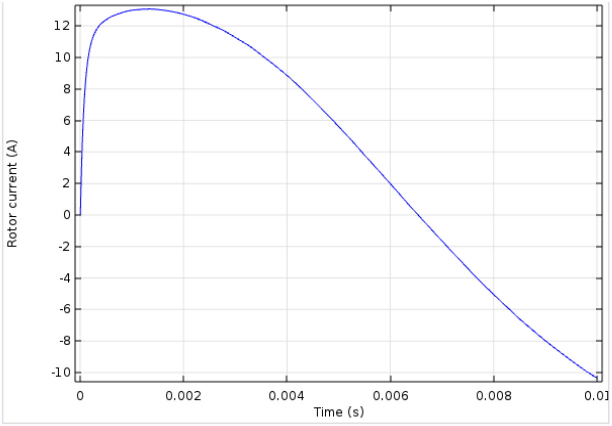

Figure 6.10: Induced rotor current with solution saved at all time steps taken by the time-dependent solver

6.6.1 Application to 2D BDFIM model

Direct solvers work efficiently for 2D transient problems, and pragmatically there is little motivation to apply iterative solvers here. However, the application of iterative solvers to such cases rather than complex 3D problems can help us better understand the benefits and limitations of different iterative solvers, whilst saving considerable amount of time.
To put forth our argument more clearly, we shall explain it in a three-step process. Later, we shall tabulate the performance of direct and iterative solvers at each step.

Step-1 Stationary model

In 2D, the only component of the current density and the vector potential is normal to the plane (or the z-component). In this case, we assume that the stator as well as the rotor current densities are known well in advance. The governing equation in this case is:

$$\nabla \times (\frac{1}{\mu}\nabla \times A_z) = J_z(t) \tag{6.6}$$

where, $J_z(t)$ is the applied current density, as a function of time.
After expressing the above equation in the weak form, as mentioned in Chapter 4, we arrive at the system of equations of the following form:

$$[S]\boldsymbol{U}_A = \boldsymbol{F} \tag{6.7}$$

where, $\boldsymbol{U}_A$ is the vector with its components being the degrees of freedom corresponding to the vector potential.
The stiffness matrix S, is symmetric and positive definite in this case. Hence, it is a straightforward choice to employ the CG solver.

Step-2 Model with sliding boundaries

We now introduce moving (or more precisely rotating) domains to the stationary problem in the previous step. The rotor domains are rotating with respect to the stator. An interface is set up in the airgap, with the sections adjacent to the stator and the rotor being stationary and moving respectively. See Figure 6.11. At the interface, the vector potential on the stator side should match that on the rotor side. That is,

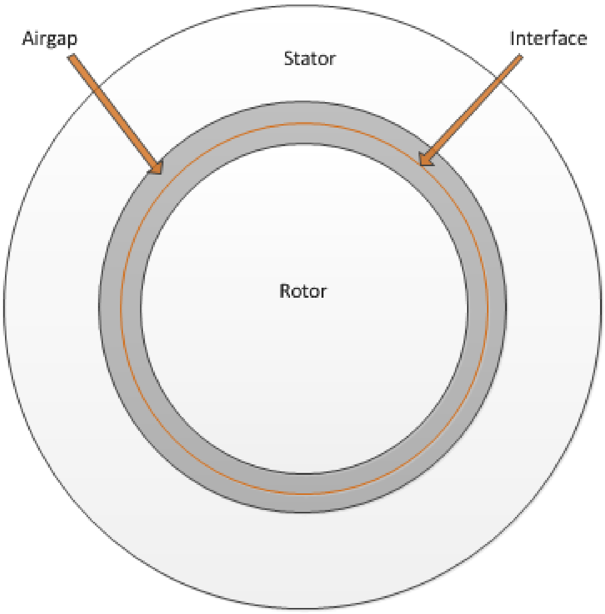

Figure 6.11: Stator-rotor interface.

$$A_{st} - A_{rt} = 0 \qquad\qquad on \quad \Gamma_{interface} \tag{6.8}$$

This condition can be satisfied by imposing a *weak constraint* on this interface. Weak constraints enforce the required condition in an average sense, by using Lagrange multipliers as a weighting function [56]. Mathematically put,

$$\int_{\Gamma_{interface}} \lambda(A_{st} - A_{rt}) \quad d\Gamma = 0 \tag{6.9}$$

Clearly, using the Lagrange multipliers introduces additional degrees of freedom. This is seen from the resulting system of equations which takes the form:

$$\begin{bmatrix} S & B \\ B^T & C \end{bmatrix} \begin{bmatrix} U_A \\ \lambda \end{bmatrix} = \begin{bmatrix} F \\ 0 \end{bmatrix} \tag{6.10}$$

Here, B and B^T are the coupling matrices resulting from the weak forms of equations (6.6) and (6.10). More concisely (6.10) can be written as:

$$[SS]\boldsymbol{U}_{A,\lambda} = \boldsymbol{F}_\lambda \tag{6.11}$$

The matrix SS, arising from this formulation is singular. This implies that though it is symmetric, it is not positive definite [49, 57]. A typical solver to be used under such circumstances would be the MINRES. However, since COMSOL does not offer this an option, we opt for the GMRES solver instead.

Step-3 Model with sliding boundaries and circuit equations

In order to complete a transient model for the BDFIM, we include the equations for the rotor conductors and couple them with the field equations. More details on the coupled field-circuit models can be found in [23, 56–59].

The field equation for the transient BDFIM model can be written as:

$$\nabla \times (\frac{1}{\mu}\nabla \times A_z) + \sigma\frac{\partial A_z}{\partial t} + \frac{N_t I_r}{S_r} = J_z(t) \tag{6.12}$$

Here, N_r is the number of turns in the rotor coil. To generalize the equation, $N_t = 0$ for all other domains except the rotor conductors.

The circuit equation for the rotor current is given by:

$$I_r R_r + \frac{L}{S_r}\iint_{S_r} (\frac{\partial A_z^+}{\partial t} - \frac{\partial A_z^-}{\partial t})ds = 0 \tag{6.13}$$

where, A_z^+ and A_z^- represent vector potentials at go and return conductors of the loop respectively.

Combining the weak forms of equations (6.12), (6.13) and (6.8), we obtain the following system of equations:

$$\begin{bmatrix} G & 0 \\ Q & 0 \end{bmatrix} \begin{bmatrix} \dot{U}_{A,\lambda} \\ \dot{I}_r \end{bmatrix} + \begin{bmatrix} SS & P \\ 0 & R \end{bmatrix} \begin{bmatrix} U_{A,\lambda} \\ I_r \end{bmatrix} = \begin{bmatrix} F_\lambda \\ 0 \end{bmatrix} \tag{6.14}$$

To speed up the calculations and neglect eddy current effects, we can substitute $\sigma = 0$ in (6.12). However, that makes the matrix, $G = 0$ and consequently results in a singular mass matrix. To avoid numerical difficulties, it is suggested to opt for a small but non-zero value of conductivity in the model. The solver of choice in this case has to be GMRES.

Model type	**Iterative solver**	**Time cost for iterative solver**	**Time cost for direct solver**
Step-1	GMG/CG	2min 12s	3min 15s
Step-2	GMG/GMRES (50)	15min 52s	21min 49s
Step-3	GMG/GMRES (50)	1h 19min 47s	53min 7s
Step-3	AMG/GMRES (50)	4h 9min 17s	53min 7s

Table 6-1: Comparison between direct and iterative solvers for 2D transient analysis.

6.6.2 Comparison with Direct Solver

Table 6-1 compares the performance of the iterative solver with the direct solvers for the three cases mentioned above. Since, the problem is 2D in nature and thus has relatively fewer degrees of freedom, the memory comparison is unlikely to give any clear insight. Therefore, the comparison has only been done on the basis of time cost.

The simulations were performed from $t = 0$ to $t = 0.038$ seconds, which corresponds to one complete cycle of rotor current in the BDFIM (for PW frequency of 50 Hz and CW frequency of 10 Hz).
As we can see from Table 6-1, the choice for the type of iterative solver is problem-specific. Clearly, due to the presence of indefinite and/or non-symmetric matrices we are forced to employ GMRES solver instead of CG for 2D transient problems, including motion and circuit equations. This has implications on the time cost and the memory requirement of the model. Same argument holds for the 3D transient problems.
Another fact that becomes evident from Table 6-1 is that the iterative solvers in the transient case do not significantly outperform direct solvers in terms of time cost. Therefore, extending the same set of solvers or preconditioners to 3D problems is unlikely to produce promising results. Also, given the fact that GMG/AMG preconditioners work in 2D transient problems, it should not be assumed that the same will hold in 3D problems.

6.6.3 Application to 3D Induction machine model

In Section 6.4 we discussed the 3D model of an induction machine. At that moment we had solved the problem using the direct solvers. In this section we shall discuss the performance of the GMRES solver with different preconditioners for the same problem.
In certain cases, GMRES with different preconditioners did exhibit properties of convergence, however, in all cases the time cost was too large compared to the direct solvers mentioned earlier. Nevertheless, the memory requirement was clearly far less than those demanded by the direct solvers. This was the case with SOR Vector and Vanka preconditioners.
In other cases, for instance, with ILU or multigrid (both GMG and AMG) preconditioners, it was difficult to obtain convergence even for first couple of time steps.
In both the aforementioned cases, similar initial conditions were provided.

6.7 Conclusions

Performing 3D transient modeling of the BDFIM is a non-trivial task. The task is further complicated if the pole-pair combination is such that the whole geometry needs to be modeled. Absence of a magnetic plane of symmetry increases the number of degrees of freedom, and consequently the computational memory and time cost. In addition to this, the necessity to model airgap with the magnetic scalar potential and to ensure that these domains remain simply connected adds to the complexity. Nonetheless the task at hand is possible albeit may not always be feasible.

As with the magnetostatic case, the memory requirement and time cost of the models can be decreased by recourse to iterative solvers. However, with increased complexity of the model, such as 3D BDFIM, it gets increasingly difficult to arrive at an optimum preconditioner. The non-symmetric and indefinite matrices resulting from the coupling of circuit equations with the field equations, and including sliding boundaries, often make the use of best iterative solvers such as CG and preconditioners like GMG impossible. The performance of other solvers such as GMRES is not always desirable. Unless ways are found to tackle these issues, large scale 3D transient modeling of the BDFIM will be a difficult task to accomplish.

Chapter 7

Conclusions and recommendations

The Stone Age didn't end for lack of stones, and the oil age will end long before the world runs out of oil.—Sheikh Ahmad Zaki Yamani

---

Chapter summary:

This chapter is meant to briefly conclude the contributions from this thesis and present some avenues for further research in future.

7.1 Conclusions

7.1.1 On modeling in 3D

2D models for electrical machines, in general, often ignore electromagnetic and thermal effects arising from several aspects such as anisotropy of the iron, end windings and skewed conductors. A complete 3D model can address these issues albeit at the cost of significant memory and time.
This thesis outlines the basis for developing magnetostatic as well as transient models of the BDFIM in 3D,however, only limited effects were accounted for in the modeling examples. This was primarily done to avoid high time cost of the more complex models. The 3D models developed for BDFIM take the laminated structure of the stator and the rotor iron into account. In addition to this, the impact of the axial flux arising in the skewed rotor was also studied.
The models including saturation effect were only briefly described due to time limitations. The time cost does not only increase due to more number of iterations needed to arrive at the final solution, but incorporating saturation also necessitates the use of a finer mesh in the iron, especially in or near the teeth regions.
The large number of unknowns arising in a 3D finite element problem dictates the use of iterative methods for solving system of equations over the direct methods. 3D models are also more prone to non-convergence or stalled convergence compared to 2D models when solved

using the iterative solvers. Therefore, extra care has to be taken while setting up the model. This includes properly defining the geometry, such as avoiding corners, and opting for the best possible element shape for a particular problem. Unfortunately, there are no hard and fast rules as to what type of elements should be used under different circumstances. A foresight about the solution based on experience or understanding of the problem and corresponding boundary conditions can be helpful in making an informed guess.

Usually we are interested in the derivative of the primary dependent variable rather than the variable itself, for instance, deriving the magnetic flux density from the magnetic vector potential. A relatively smoother geometry and optimally selected elements also result in a more accurate value of the desired derivative. A poorly defined geometry can result in unrealistic values for the derivative of the primary dependent variable.

2D models are formulated using the normal component of the magnetic vector potential. The choice for the magnetic potential is not so straightforward in 3D. Formulations using the magnetic scalar potential are simpler to understand and implement, in addition to being economic computationally, generally speaking. However, scalar potential formulation cannot be applied in all cases, and thus the need for the magnetic vector potential. A mixed formulation may therefore seem to be the best alternative. Unfortunately, minimizing the degrees of freedom is not the only measure of how efficient a particular potential formulation is in a certain case. When solving the system of equations using iterative methods, the properties of the resulting stiffness matrix have a big impact on how efficiently these equations can be solved. For instance, a full vector potential (ungauged) formulation which results in a symmetric positive definite matrix, can be advantageous computationally over a mixed formulation with fewer degrees of freedom.

Time dependent problems, involving moving rotor and circuit equations for the rotor currents, are more complex to deal with. In addition to appropriate boundary conditions such problems also require consistent initial conditions. Moreover, ensuring continuity of the potential across the sliding boundaries, between the stator and the rotor regions in the airgap, by means of imposing the weak constraints results in an indefinite stiffness matrix. This again has implications for the choice of the iterative solver to be used.

Coupling of field equations with the rotor circuit equations, and the scaling factor used for the magnetic vector potential variable and the electrical variables also influence the type and performance of the solver that can be employed.

Quite often the matrices resulting from the FEM discretized models have high condition numbers which makes the convergence to the solution a painstakingly long process. Under such circumstances, preconditioning of the matrix equations should be done to facilitate the solution process. Multigrid methods are a popular class of preconditioners. However, like most methods they are not always the best choice. The choice of a preconditioner, much like the that of the iterative solver, is indeed highly problem-specific.

7.1.2 Concerning the BDFIM model

A proper estimation of the axial flux is only possible if the laminated structure of the stator and the rotor iron in the BDFIM is somehow accounted for in the 3D models. Modeling each sheet of lamination individually—perhaps unnecessarily—complicates the 3D model, instead using an effective permeability tensor seems to be a good approximation. The magnitude of the elements within this permeability tensor is a function of the stacking factor of the iron. Consequently, the magnitude of the axial flux and other electromagnetic quantities such as torque developed also depend on the stacking factor, however, to different extents.

Clearly, a high stacking factor implies lower axial reluctance and thus, a higher magnitude of the axial flux. However, the nominal stacking factors in the range of 0.95-0.98 result in a relatively insignificant magnitude of the axial flux, at least two orders of magnitude smaller than the radial flux . This axial flux, therefore, should not lead to substantial eddy losses even though the axial flux is orthogonal to the plane of lamination. Obviously, eddy losses due to the axial flux increase with the stacking factor.

As far as estimation of the developed torque in the BDFIM is concerned, assuming isotropic iron leads to an overestimation of torque. Nonetheless, this exaggeration is not substantial as the stacking factors are usually very high. Higher stacking factor obviously results in torque values closer to that predicted by the model with isotropic iron properties.

The circumferential torque is determined by the radial flux density in the airgap. The axial flux does not directly influence the torque, however, it does have an impact on the distribution of the radial flux density. It adds to the radial flux at one end of the machine and subtracts from it at the other, and thus can influence the torque produced indirectly. The question whether at any specific rotor position, does the axial flux add or reduce the torque cannot be, at this moment, answered unequivocally. However, what can be said is that the impact of the axial flux on torque for the BDFIM is small enough to be neglected. Therefore, for purposes of analyzing effects of skew one can with high degree of certainty rely on the results obtained from the multi-slice model without recourse to 3D modeling.

7.2 Contributions

The scientific contributions from this thesis can be summarized as follows:

1. A 3D magnetostatic finite element model of the BDFIM was built. The methodology explained in the thesis can be in general adopted for any other electrical machine. Iterative solvers with multigrid preconditioners were introduced to solve such large scale problems involving several million unknowns, with efficiency both in terms of memory and time cost.

2. The magnetostatic model was able to quantify the magnitude of the axial component of the magnetic flux density arising from the skewed rotor in the BDFIM.

3. The effects of the axial component and anisotropy of the iron on performance parameters such as torque was studied. This also helped us to establish the validity of the 2D multi-slice model.

4. This thesis also briefly describes methods to arrive at a solution for problems involving non-linear effects such as saturation in the 3D models.

5. The groundwork was established for solving 3D transient models for electrical machines, involving motion and circuit equations. However, it was only demonstrated for a system with few hundred thousand degrees of freedom and solved using direct solvers. The limitations of iterative solvers to tackle such large scale transient problems in 3D were also documented.

7.3 Recommendations

Owing to the complexity of the 3D models, we have analyzed only few effects which were neglected in earlier 2D models, whereas many other effects remain to be studied. We suggest some of them here to be considered in the future:

1. 3D magnetostatic models can be used to estimate the end winding inductances. These inductances can then be included in the rotor circuit equations for the 2D multi-slice model. This hybrid modeling will result in a more accurate estimation of performance parameters.
2. Eddy current losses resulting from the axial component of the flux can be estimated. This axial flux not only arises from the skew but also due to the end windings.
3. Solving 3D transient models—involving motion and circuit equations—using iterative solvers was found to be a major challenge. Future studies can either focus on finding better solvers, using finite element formulations which result in matrices with favorable properties or both.
4. Also, 3D finite element modeling for apparatus such as electrical machines or optimization algorithms often require a considerable amount of memory. It would be worthwhile to explore options for parallel or distributed computing for such cases.

Bibliography

[1] M. O. Hansen, *Aerodynamics of wind turbines.* Routledge, 2015.

[2] F. Blázquez, C. Veganzones, D. Ramírez, and C. Platero, “Characterization of the rotor Magnetic field in a brushless doubly-fed induction machine,” *IEEE Transactions on Energy Conversion*, vol. 24, no. 3, pp. 599–607, 2009.

[3] R. A. McMahon, X. Wang, E. Abdi-Jalebi, P. J. Tavner, P. C. Roberts, and M. Jagiela, “The BDFM as a Generator in Wind Turbines,” *2006 12th International Power Electronics and Motion Control Conference*, 2006.

[4] T. Long, S. Shao, E. Abdi, P. Malliband, M. E. Mathekga, R. a. Mcmahon, and P. J. Tavner, “Symmetrical Low Voltage Ride-Through of a 250 kW Brushless DFIG under a Symmetrical Full Voltage Dip,” *Power Electronics, Machines and Drives (PEMD 2012), 6th IET International Conference on*, 2012.

[5] R. A. McMahon, P. C. Roberts, X. Wang, and P. J. Tavner, “Performance of BDFM as generator and motor,” *IEE Proceedings-Electric Power Applications*, vol. 153, no. 2, 2006.

[6] N. H. V. D. Blij, T. D. Strous, X. Wang, and H. Polinder, “A Novel Analytical Approach and Finite Element Modelling of a BDFIM,” *IEEE*, pp. 346–352, 2014.

[7] P. C. Roberts, R. A. McMahon, P. J. Tavner, J. M. Maciejowski, and T. J. Flack, “Equivalent circuit for the brushless doubly fed machine (BDFM) including parameter estimation and experimental verification,” *IEE Proceedings-Electric Power Applications*, vol. 152, no. 4, 2005.

[8] X. Wang, T. D. Strous, D. Lahaye, H. Polinder, and J. A. Ferreira, “[effects of rotor skew on the performance of brushless doubly-fed induction machine],” pp. 260–265, 2015.

[9] T. D. Strous, X. Wang, H. Polinder, and J. Ferreira, “Brushless doubly-fed induction machines: Torque ripple,” in *Electric Machines & Drives Conference (IEMDC)*, 2015.

[10] T. Strous, N. van der Blij, H. Polinder, and J. A. Ferreira, "Brushless doubly-fed induction machines: Magnetic field modelling," in *Electrical Machines (ICEM), 2014 International Conference on*, pp. 2702–2708, IEEE, 2014.

[11] T. D. Strous, X. Wang, H. Polinder, and J. Ferreira, "Finite element based multi-objective optimization of a brushless doubly-fed induction machine," Electric Machines & Drives Conference (IEMDC), 2015.

[12] X. Wang, T. Strous, D. Lahaye, H. Polinder, and J. Ferreira, "Finite element modeling of brushless doubly-fed induction machine (bdfim) based on magneto-static simulation," in *Int. Conf. Elect. Machines & Drives (IEMDC)*, 2015.

[13] B. E. Thompson, "Three-dimensional finite element design procedure for the brushless doubly fed machine," *Master's thesis, Oregon State University*, 1995.

[14] C. Steinmetz, "Operating alternating motors," Aug. 3 1897. US Patent 587,340.

[15] L. J. Hunt, "A new type of induction motor," *Electrical Engineers, Journal of the Institution of*, vol. 39, no. 186, pp. 648–667, 1907.

[16] F. Creedy, "Some developments in multi-speed cascade induction motors," *Electrical Engineers, Journal of the Institution of*, vol. 59, no. 301, pp. 511–532, 1921.

[17] A. R. W. Broadway and L. Burbridge, "Self-cascaded machine: a low-speed motor or high-frequency brushless alternator," *Electrical Engineers, Proceedings of the Institution of*, vol. 117, no. 7, pp. 1277–1290, 1970.

[18] R. Li, R. Spée, A. K. Wallace, and G. Alexander, "Synchronous drive performance of brushless doubly-fed motors," *Industry Applications, IEEE Transactions on*, vol. 30, no. 4, pp. 963–970, 1994.

[19] D. Hanselman, "Effect of skew, pole count and slot count on brushless motor radial force, cogging torque and back EMF," *IEE Proceedings - Electric Power Applications*, vol. 144, no. 5, p. 325, 1997.

[20] D. C. Hanselman, *Brushless motors: magnetic design, performance, and control of brushless dc and permanent magnet synchronous motors.* E-Man Press LLC, 2012.

[21] K. Binns, R. Hindmarsh, and B. Short, "Effect of skewing slots on flux distribution in induction machines," *Electrical Engineers, Proceedings of the Institution of*, vol. 118, no. 3.4, pp. 543–549, 1971.

[22] S. Ho and W. Fu, "A comprehensive approach to the solution of direct-coupled multislice model of skewed rotor induction motors using time-stepping eddy-current finite element method," *Magnetics, IEEE Transactions on*, vol. 33, no. 3, pp. 2265–2273, 1997.

[23] J. P. A. Bastos and N. Sadowski, *Electromagnetic modeling by finite element methods.* CRC press, 2003.

[24] T. Yamaguchi, Y. Kawase, and S. Sano, "3-d finite-element analysis of skewed squirrel-cage induction motor," *IEEE transactions on magnetics*, vol. 40, no. 2, pp. 969–972, 2004.

[25] Y. Kawase, T. Yamaguchi, Z. Tu, N. Toida, N. Minoshima, and K. Hashimoto, "Effects of skew angle of rotor in squirrel-cage induction motor on torque and loss characteristics," *Magnetics, IEEE Transactions on*, vol. 45, no. 3, pp. 1700–1703, 2009.

[26] H. Kometani, S. Sakabe, and A. Kameari, "3-d analysis of induction motor with skewed slots using regular coupling mesh," *Magnetics, IEEE Transactions on*, vol. 36, no. 4, pp. 1769–1773, 2000.

[27] R. P. Feynman, R. B. Leighton, and M. Sands, *The Feynman lectures on physics, vol. 2: Mainly electromagnetism and matter.* Addison-Wesley, 1979.

[28] D. J. Griffiths, "Electrodynamics," *Introduction to Electrodynamics, 3rd ed., Prentice Hall, Upper Saddle River, New Jersey*, 1999.

[29] P. P. Silvester and R. L. Ferrari, *Finite elements for electrical engineers.* Cambridge university press, 1996.

[30] M. Kuczmann, "Potential formulations in magnetics applying the finite element method," *Lecture notes, Laboratory of Electromagnetic Fields,Széchenyi István University, Gyor, Hungary*, 2009.

[31] M. Popescu, "Prediction of the electromagnetic torque in synchronous machines through maxwell stress harmonic filter (hft) method," *Electrical Engineering*, vol. 89, no. 2, pp. 117–125, 2006.

[32] C. Steinmetz, "On the law of hysteresis," *American Institute of Electrical Engineers, Transactions of the*, vol. 9, no. 1, pp. 1–64, 1892.

[33] H. Gorginpour, H. Oraee, and E. Abdi, "Calculation of core and stray load losses in brushless doubly fed induction generators," *Industrial Electronics, IEEE Transactions on*, vol. 61, no. 7, pp. 3167–3177, 2014.

[34] V. N. Kaliakin, *Introduction to approximate solution techniques, numerical modeling, and finite element methods.* CRC Press, 2001.

[35] Y. Zhu and A. C. Cangellaris, *Multigrid finite element methods for electromagnetic field modeling*, vol. 28. John Wiley & Sons, 2006.

[36] W. Frei, "Meshing your geometry: When to use the various element types," *http://www.comsol.com/blogs/meshing-your-geometry-various-element-types/*, 2013.

[37] G. Iaccarino, "Geometric modeling and grid generation," *http://web.stanford.edu/class/me469b/handouts/geoandgrid.pdf*, 2004.

[38] J. P. A. Bastos and N. Sadowski, *Magnetic materials and 3D finite element modeling.* CRC Press, 2013.

[39] W. Frei, "How much memory is needed to solve large comsol models?," *http://www.comsol.com/blogs/much-memory-needed-solve-large-comsol-models/*, 2014.

[40] R. Barrett, M. W. Berry, T. F. Chan, J. Demmel, J. Donato, J. Dongarra, V. Eijkhout, R. Pozo, C. Romine, and H. Van der Vorst, *Templates for the solution of linear systems: building blocks for iterative methods*, vol. 43. SIAM, 1994.

[41] G. H. Golub and C. F. Van Loan, *Matrix computations*, vol. 3. JHU Press, 2012.

[42] V. Marra, “On solvers: Multigrid methods,” *https://www.comsol.no/blogs/on-solvers-multigrid-methods/*, 2013.

[43] J. Yström and L. Gordon, “Fast solvers for complex problems,” *http://machinedesign.com/archive/fast-solvers-complex-problems*, 2007.

[44] V. Marra, “On solvers: The v-cycle multigrid,” *https://www.comsol.no/blogs/on-solvers-v-cycle-multigrid/*, 2013.

[45] L. Andersson, “Fillet away your electromagnetic field singularities,” *https://www.comsol.com/blogs/fillet-away-your-electromagnetic-field-singularities/*, 2014.

[46] V. C. Silva, G. Meunier, and A. Foggia, “A 3-d finite-element computation of eddy currents and losses in laminated iron cores allowing for electric and magnetic anisotropy,” *Magnetics, IEEE Transactions on*, vol. 31, no. 3, pp. 2139–2141, 1995.

[47] C. Carpenter, “Theory of flux penetration into laminated iron and associated losses,” *Electrical Engineers, Proceedings of the Institution of*, vol. 124, no. 7, pp. 659–664, 1977.

[48] J. Donea, A. Huerta, J.-P. Ponthot, and A. Rodriguez-Ferran, “Encyclopedia of computational mechanics vol. 1: Fundamentals., chapter 14: Arbitrary lagrangian-eulerian methods,” 2004.

[49] COMSOL, “Comsol multiphysics reference manual 5.1,” 2015.

[50] “Comsol reference manual, rotating machinery 3d tutorial,” *https://www.comsol.nl/model/download/264151/models.acdc.rotating_machinery_3d_tutorial.pdf*, 2013.

[51] A. Ferrario, “How to model rotating machinery in 3d,” *https://www.comsol.nl/blogs/how-to-model-rotating-machinery-in-3d/*, 2015.

[52] N. Paudel, “Guidelines for modeling rotating machines in 3d,” *https://www.comsol.nl/blogs/guidelines-for-modeling-rotating-machines-in-3d/*, 2016.

[53] “Simply connected regions,” *http://ocw.mit.edu/courses/mathematics/18-02sc-multivariable-calculus-fall-2010/3.-double-integrals-and-line-integrals-in-the-plane/part-c-greens-theorem/session-72-simply-connected-regions-and-conservative-fields/MIT18_02SC_MNotes_v5.pdf*, 2010.

[54] X. Wang, T. D. Strous, D. Lahaye, H. Polinder, and J. A. Ferreira, “Finite element modeling of brushless doubly-fed induction machine based on magneto-static simulation,”

[55] B. Sjodin, “Using curvilinear coordinates,” *https://www.comsol.nl/blogs/using-curvilinear-coordinates/*, 2013.

[56] H. Lai, P. Leonard, D. Rodger, N. Allen, and P. Sangha, “3d finite element dynamic simulation of electrical machines coupled to external circuits,” *IEEE Transactions on Magnetics*, vol. 33, no. 2, pp. 2010–2013, 1997.

[57] C. Biddlecombe, J. Simkin, A. Jay, J. Sykulski, and S. Lepaul, "Transient electromagnetic analysis coupled to electric circuits and motion," *IEEE Transactions on magnetics*, vol. 34, no. 5, pp. 3182–3185, 1998.

[58] J. Vaananen, "Circuit theoretical approach to couple two-dimensional finite element models with external circuit equations," *IEEE Transactions on Magnetics*, vol. 32, no. 2, pp. 400–410, 1996.

[59] G. Bedrosian, "A new method for coupling finite element field solutions with external circuits and kinematics," *IEEE Transactions on Magnetics*, vol. 29, no. 2, pp. 1664–1668, 1993.